

**Synthesis and Characterization of Immobilized Gold  
Nanoparticles and Binary Gold Nanoalloys on Cationic  
Spherical Polyelectrolyte Brushes and their  
Application as a Catalyst**

**DISSERTATION**

zur Erlangung des akademischen Grades eines  
Doktors der Naturwissenschaften (Dr. rer. nat.)  
im Fach Chemie  
der Fakultät für Biologie, Chemie und Geowissenschaften  
der Universität Bayreuth

Vorgelegt von  
**Marc Claudius Schrinner**  
Geboren in Nürnberg, Mittelfranken

Bayreuth, 2008





---

Die vorliegende Arbeit wurde in der Zeit von April 2006 bis Oktober 2008 am Lehrstuhl für Physikalische Chemie I (PC I) an der Universität Bayreuth unter der Betreuung von Herrn Prof. Dr. Matthias Ballauff angefertigt.

Vollständiger Abdruck der von der Fakultät für Biologie, Chemie und Geowissenschaften der Universität Bayreuth genehmigten Dissertation zur Erlangung des akademischen Grades eines Doktors der Naturwissenschaften (Dr. rer. nat.).

Tag der Einreichung des Promotionsgesuches:

08. Oktober 2008

Tag des wissenschaftlichen Kolloquiums:

10. Dezember 2008

Prüfungsausschuss:

Prof. Dr. M. Ballauff (Erstgutachter)

Prof. Y. Talmon (Zweitgutachter)

Prof. Dr. A. Böker (Vorsitzender)

Prof. Dr. J. Breu

Amtierender Dekan: Prof. Dr. Axel H. E. Müller

---

---

---

---

*Zum Golde drängt,  
am Golde hängt doch alles.*

J. W. Goethe, Faust I

---

---

*Meiner Familie*

---

## Table of Contents

<b>1</b>	<b>Introduction</b>	<b>1</b>
1.1	Gold Nanoparticles	1
1.2	Binary Metal Nanoalloys	1
1.3	Facetted Metal Nanoparticles	3
1.4	Methods for Stabilization of Metal Nanoparticles	4
1.5	Spherical Polyelectrolyte Brushes (SPB)	7
1.6	Application of Gold Nanoparticles and Binary Metal Nanoalloys in Catalysis	10
1.7	Transmission Electron Microscopy	11
1.8	Objectives of this Thesis	12
1.9	References	14
<b>2</b>	<b>Overview of this Thesis – Results</b>	<b>17</b>
2.1	Synthesis and Characterization of SPB	18
2.2	Structure Studies of SPB	20
2.3	Synthesis and Characterization of Gold Nanoparticles	23
2.4	Synthesis and Characterization of Binary Gold Nanoalloys	25
2.5	Synthesis and Characterization of Platinum Nanocrystals	28
2.6	Application of Metal Nanoparticles in Catalysis	31
2.7	Individual Contribution to Each Publication	34
2.8	References	36
<b>3</b>	<b>Publications of this Thesis</b>	<b>37</b>
3.1	A Novel Photoreactor for the Production of Electrosterically Stabilised Colloidal Particles at Larger Scales	37
3.2	Binding of Oppositely Charged Surfactants to Spherical Polyelectrolyte Brushes: A Study by Cryogenic	47

---

	Transmission Electron Microscopy	
3.3	Mechanism of the Formation of Amorphous Gold Nanoparticles within Spherical Polyelectrolyte Brushes	53
3.4	Stable Bimetallic Gold-Platinum Nanoparticles Immobilized on Spherical Polyelectrolyte Brushes	61
3.5	Single-Nanocrystals of Platinum Prepared by Partial Dissolution of Au-Pt-Nanoalloys	75
3.6	Nanoalloys as Efficient “Green” Catalysts for the Epoxidation of Alkenes by Molecular Oxygen	99
4	<b>Summary/Zusammenfassung</b>	<b>121</b>
5	<b>Publications</b>	<b>125</b>
5.1	Publications of this Thesis	125
5.2	Publications as co-author	125
6	<b>Appendix</b>	<b>127</b>
6.1	Presentations at International Meetings	127
6.2	Abbreviations and Symbols	128
6.3	Danksagung	130
6.4	Schlusserklärung	132

---

# 1 Introduction

Metal nanoparticles (MeNP) play an important and more considerable role in different areas of science and daily life.<sup>[1]</sup> Silver nanoparticles (AgNP) for example are used in modern wound management, as disinfectants.<sup>[1]</sup> The catalytic properties of gold- and platinum metal nanoparticles (AuNP, PtNP) lead to widespread applications in catalysis.<sup>[2-4]</sup> Many new techniques (Lotus effect) and materials are introduced by nanoparticles and -techniques.<sup>[1]</sup>

## 1.1 Gold Nanoparticles

Although gold is the subject of one of the most ancient themes of investigation in science, its renaissance now leads to an exponentially increasing number of publications.<sup>[5,6]</sup> AuNP have been in the focus of literature during the last seven years.<sup>[5,6]</sup> AuNP are the most stable metal nanoparticles. The totally different properties of bulk material and nanoparticles are in the focus of interest: Physicists predicted that nanoparticles in the diameter range 1 – 10 nm (intermediate between the size of small molecules and that of bulk metal) would display electronic structures, reflecting the electronic band structure of the nanoparticles, owing to quantum-mechanical laws.<sup>[7]</sup> The resulting physical properties are neither those of bulk metal nor those of molecular compounds, but they strongly depend on the particle size, interparticle distance, nature of the protecting organic shell and shape of the nanoparticles.<sup>[5]</sup> In the nanosize the particle-particle distance, the organic stabilizer and the shape of the nanoparticles are important.<sup>[8,9]</sup> Reviews of the state of research and fundamentals are found in articles from Daniel *et al.* and Gosh *et al.*<sup>[5,6]</sup>

## 1.2 Binary Metal Nanoalloys

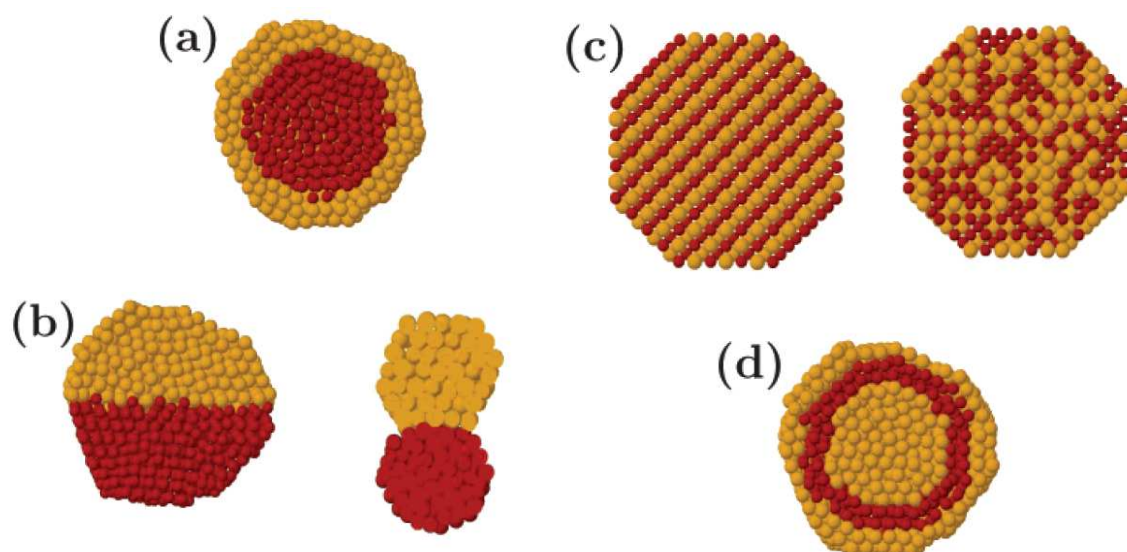
In materials science, the range of properties of metallic systems can be greatly extended by taking mixtures of elements to generate intermetallic compounds and alloys.<sup>[10]</sup> The application of nanoparticles can be extended to new areas such as electronics, engineering and catalysis.<sup>[10]</sup> In many cases, there is an enhancement in specific properties upon alloying due to synergistic effects, and

the rich diversity of compositions, structures, and properties of metallic alloys has led to widespread applications in electronics, engineering, and catalysis. The physical, chemical and material properties differ in comparison to monometallic particles.<sup>[10]</sup> The binary nanoalloy of gold and palladium is for instance more stable and more active as a catalyst of both monometallic nanoparticles gold and palladium.<sup>[11]</sup> An interesting point is the synthesis of binary nanoalloys, where there are no similarities in the macroscopic world. These nanoalloys show fascinating new opportunities.<sup>[12-15]</sup> It is possible to synthesize different Au-Pt nanoalloys without miscibility gap. Lou *et al.* showed that Au-Pt nanoalloys have a lattice parameter depending on the composition of the mixture. The dependency is linear and follows Vegard's law.<sup>[16]</sup>

As for bulk alloys, a very wide range of combinations and compositions are possible for binary nanoalloys.<sup>[10]</sup> Bimetallic nanoalloys ( $A_mB_n$ ) can be generated with, more or less, controlled size ( $m + n$ ) and composition ( $m / n$ ). The cluster structures and degree of A-B segregation or mixing may depend on the method and conditions of cluster generation (type of cluster source, temperature, pressure, etc.). Nanoalloys can be generated in a variety of media, such as cluster beams, colloidal solutions, or can be immobilized on surfaces or inside pores.<sup>[10]</sup>

Nanoalloys can be distinguished according to their mixing and geometric structure. Figure 1 shows the four main types of mixing patterns and structures in a schematic fashion mainly found for binary nanoalloys.<sup>[10]</sup> Core-shell segregated nanoalloys (Fig. 1.1 (a)) consist of a shell of one type of atom B surrounding a core of another atom A. Figure 1.1 (b) shows subcluster segregated nanoalloys consisting of A and B subclusters, which may share a mixed interface (left) or may only have a small number of A-B bonds (right). There is no miscibility possible between the two kinds of atoms A and B. The bimetallic nanoparticle consists of two connected monometallic nanoparticles. Mixed A-B nanoalloys (Fig. 1.1 (c)) may be either ordered (left) or random. This diagramme shows a nanoalloy with statistical distributed atoms A and B. This is typically for binary nanoalloys with a faceted surface. Multishell nanoalloys (Fig. 1.1 (d)) may present layered or onion-like alternating -A-B-A- shells: The core consists of atoms A, surrounded by atoms of B, and then again atoms of A.<sup>[10]</sup>





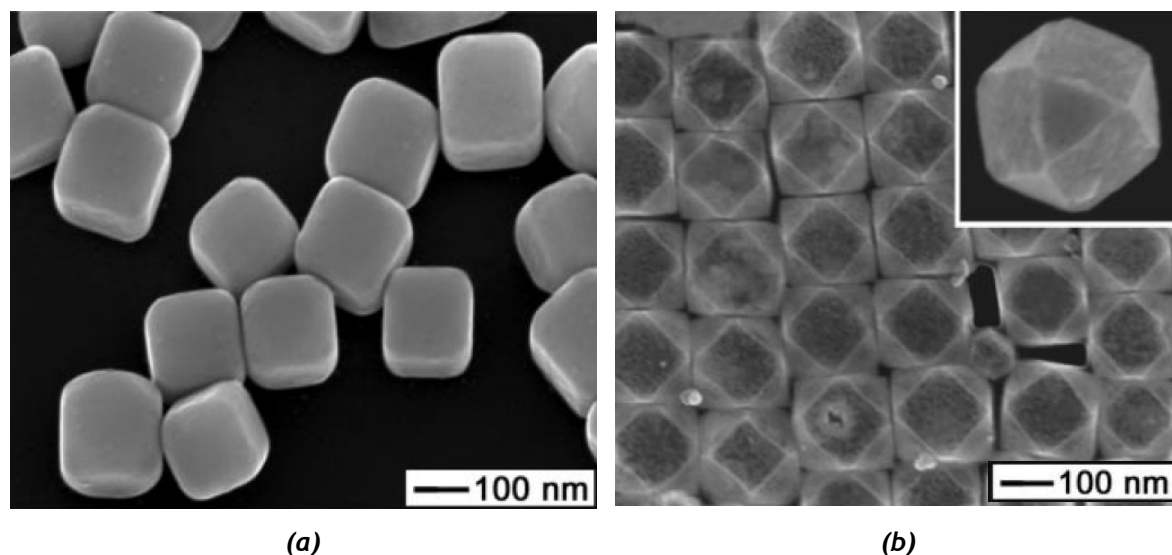
**Figure 1.1 a – d:** Schematic representation of some mixing patterns for two metals A (yellow) and B (red) in nanoscale: (a) core-shell particle, (b) segregated subcluster, (c) statistical mixed particle, (d) three shell particle. The images show cross-sections of the clusters.<sup>[10]</sup>

### 1.3 Facetted Metal Nanoparticles

Metal nanoparticles with tuned size and geometry are of interest in electronic and as optical materials and are also important in catalysis.<sup>[6,17-21]</sup> In this way they have become one of the major basic building blocks of nanotechnology. By now the intense research devoted to metallic nanoparticles in the last years has clearly demonstrated that particle morphology plays a central role in catalysis. For instance, facetted platinum crystals have been found to exhibit higher catalytic activity than spherical particles; the activity of the exposed facets may vary considerably.<sup>[19,22]</sup> The reactivity and selectivity of nanoparticles can therefore be tuned by controlling their morphology. In the opposite, amorphous platinum nanoparticles have been found to exhibit a much reduced catalytic activity.<sup>[23,24]</sup> The prospect for a number of possible applications has led to a strong activity in this field in the last years. However, facetted nanocrystals with a well-developed shape and a narrow size distribution exhibit, in general, sizes typically on the order of 100 nm and more. In previous works mainly gold<sup>[18,25]</sup>, silver<sup>[17,18,26]</sup> and platinum<sup>[21]</sup> nanocrystals were synthesized under harsh conditions. For stabilization of nanoparticles organic ligands were used. The nanocrystal size depending on the route of synthesis ranges from 10 nm to more than 100 nm. Thus, Sun *et al.* could obtain well-defined gold and silver crystals

with sizes around 100 nm. Nanoprisms of silver with dimensions around 100 nm were prepared by Jin *et al.* by a photochemical conversion of silver spheres. Anisotropic silver nanoparticles of similar size were synthesized by Liz-Marzan and co-workers through careful choice of a suitable surfactant. Platinum nanocrystals with high-index facets were obtained recently by Tian and co-workers. Here again the typical sizes range between 50 and 200 nm. Up to now, the only rather tedious route to faceted single crystals in the size range of a few nanometers is the synthesis of well defined clusters, e.g., Au<sub>55</sub>-cluster and subsequent heat treatment.

Figure 1.2 (a) and (b) shows scanning electron microscopy (SEM) micrographs of possible faceted silver and gold nanocrystal geometries.<sup>[18]</sup>

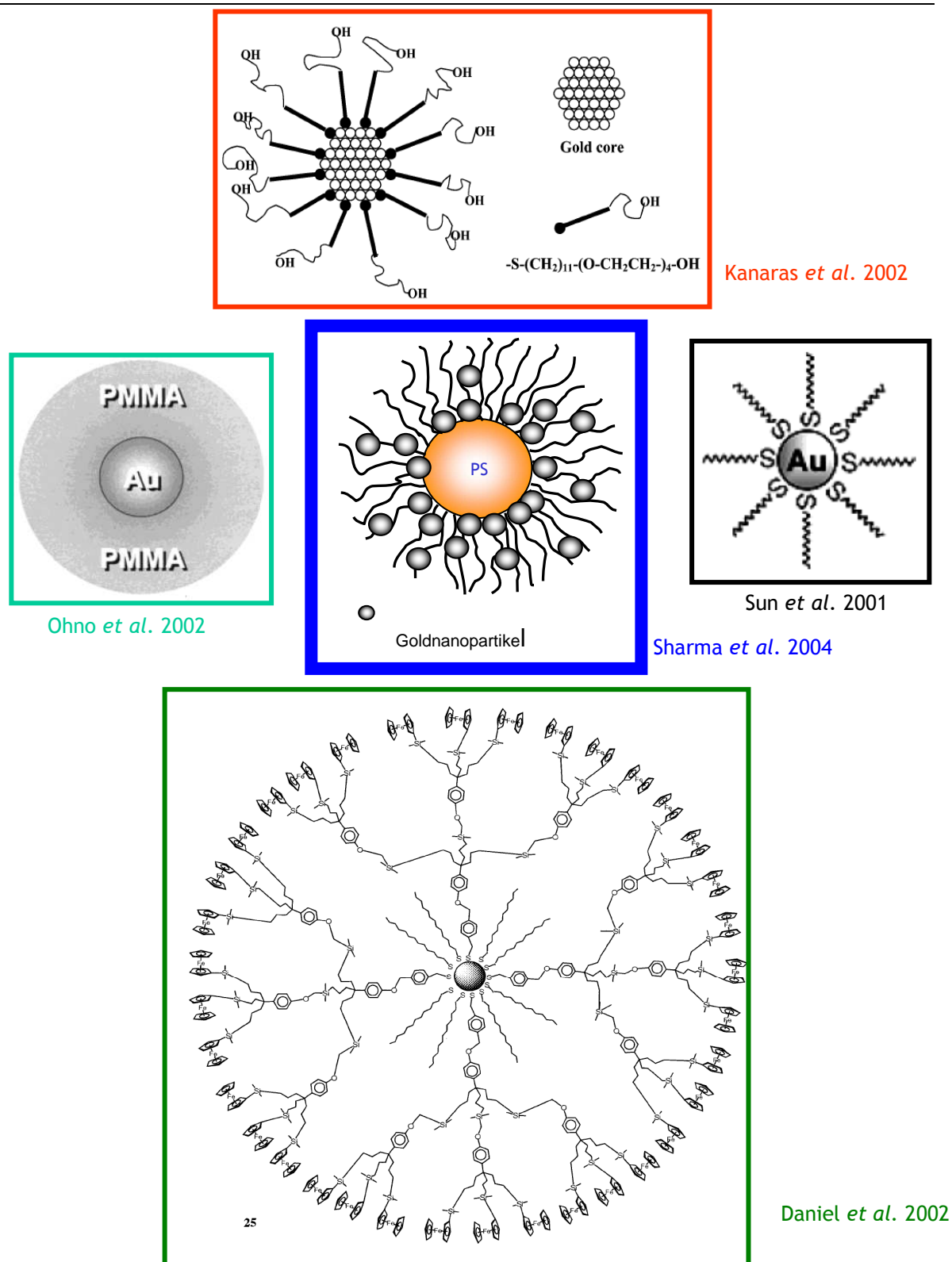


**Figure 1.2 a and b:** Scanning electron microscopy micrographs of silver nanocubes, stabilized by organic ligands (a). SEM micrograph of geometric well-defined gold nanocrystals (b).<sup>[18]</sup>

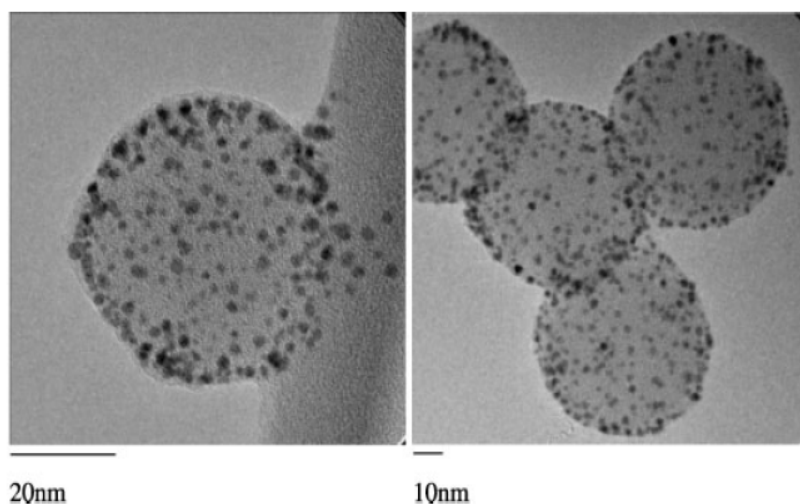
## 1.4 Methods for Stabilization of Metal Nanoparticles

The different concepts of stabilization for all monometallic and binary nanoalloys are described for AuNP. There are different concepts for generation and stabilization of gold nanoparticles.<sup>[5,27]</sup> Many groups use stabilizing agents like ligands during the generation of AuNP. Via this route the generated AuNP core is protected by a shell of ligands. In a typical experiment organic molecules, like dendritic structures or alkyl chains with a sulphur group are used.<sup>[5]</sup> In principle the resulting particle consist of one Au core with a shell of

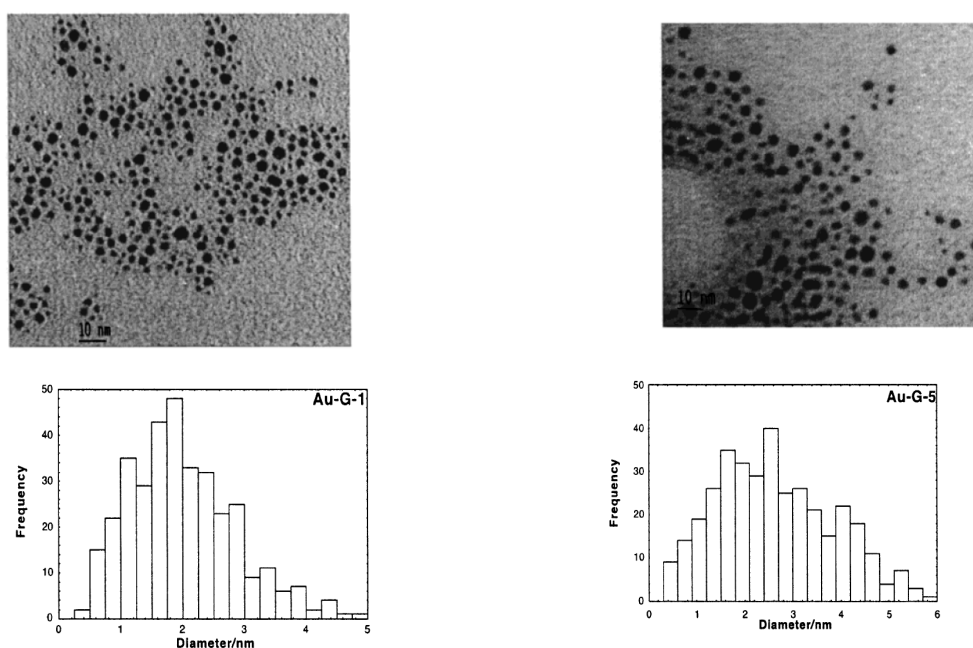
organic molecules. Figure 1.3 shows an overview of different concepts for stabilizing AuNP. In previous works the surface of the AuNP is completely covered by stabilizing agents, whereas this problem doesn't exist in Sharma's concept<sup>[28]</sup> (Chapter 1.5), used in this thesis (Fig. 1.3, middle).<sup>[28]</sup> This point is an advantage in determination of catalytic activity, for example.<sup>[5,6]</sup> There is a higher surface for catalytic processes. The interaction of the organic ligand and the AuNP has not to be taken into consideration during discussion of the results. The method of Sharma *et al.*<sup>[28]</sup> (Fig. 1.3, middle and Fig. 1.4) is compared with the method of Gopidas *et al.*<sup>[29]</sup>. This group is working with dendritic structures. The resulting gold cores are shown in Figure 1.5. A comparison of the transmission electron microscopy (TEM) images of the AuNP, show the better efficiency of Sharma's route.<sup>[28,29]</sup> The AuNP from Sharma *et al.* (Fig. 1.4) not monodispers, but more uniform, than the synthesized by Gopidas *et al.* (Fig. 1.5).



**Figure 1.3:** Overview of different concepts used for stabilizing AuNP. *Sharma et al.* are using spherical polyelectrolyte brushes (SPB); AuNP are generated inside the polyelectrolyte layer. The core consists of polystyrene (PS). *Kanaras et al.* stabilized Au cores by Hydroxy-(1-mercaptoundec-11-yl)-tetraethylenglycol. The hydrophobic  $\text{C}_{11}$ -chain stabilizes AuNP, whereas the hydrophilic Tetraethylenglycol is responsible for solubility in water. *Ohno et al.* stabilize an AuNP through a closed poly(methyl methacrylate) PMMA shell. *Sun et al.* protect the AuNP core by alkylthiolate. *Daniel et al.* protect their Au core by dendronizing with Nanoferrocenylthiol dendrons.



**Figure 1.4:** TEM micrograph<sup>[28]</sup> of gold nanoparticles (approximately 2.5 nm) onto the core-shell system used by Sharma *et al.* introduced and discussed in Figure 6 in detail.

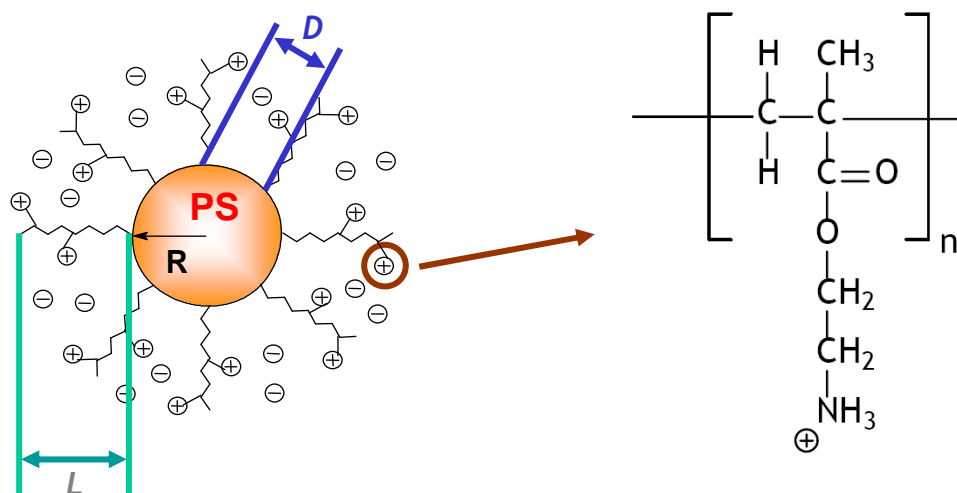


**Figure 1.5:** TEM images (top) of synthesized AuNP by Gopidas *et al.* (stabilized by dendritic structures). The particle distribution of the sample (bottom).<sup>[29]</sup>

## 1.5 Spherical Polyelectrolyte Brushes (SPB)

Spherical polyelectrolyte brushes (SPB), used as carriers in this work – were introduced by Guo *et al.*<sup>[30,31]</sup> Starting from these core shell systems with anionic polyelectrolyte chains Mei *et al.* changed the synthesis to bound cationic polyelectrolyte chains to the polystyrene core in a photo emulsion polymerization.<sup>[32]</sup> At the beginning PS cores of defined particle size are

synthesized by emulsion polymerization. In the next step a photo initiator is bound to the pre-polymerized polystyrene (PS) core. In the last step the chosen polyelectrolyte are grafted to the surface of the PS core via photo emulsion polymerization. Figure 1.6 shows in a schematic manner the characteristics of a cationic spherical polyelectrolyte brush. It is consisting of a PS core and cationic polyelectrolyte chains of 2-amino ethyl methacrylate attached to the surface of the core. The positive charge of the polyelectrolyte chains are compensated by the chloride counter ions.



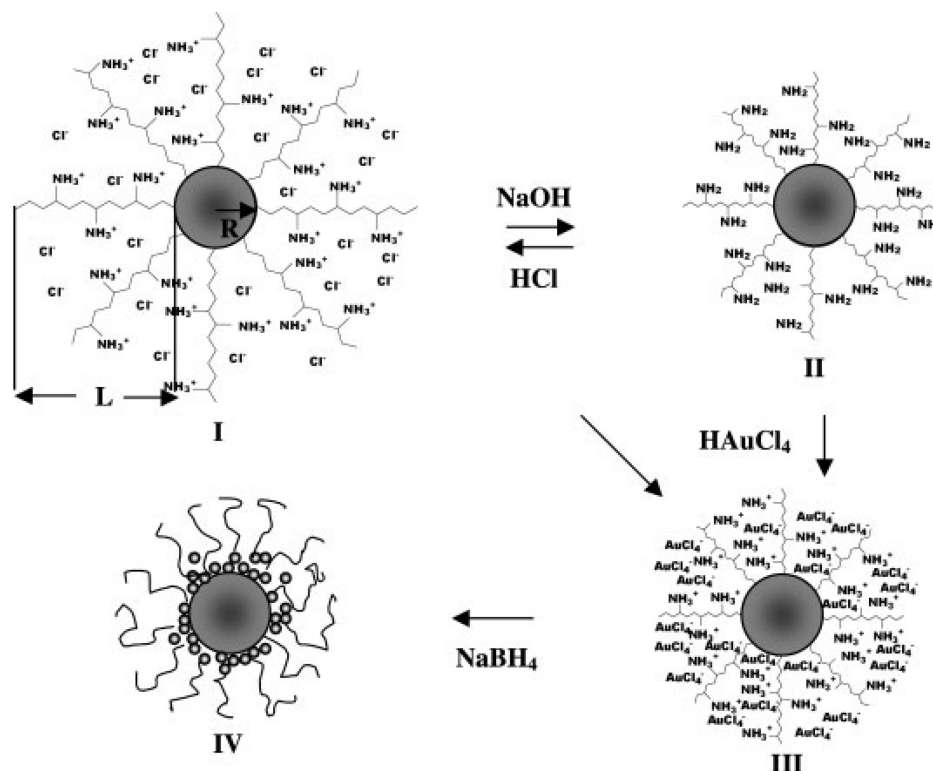
**Figure 1.6:** Schematic representation of a synthesized core-shell latex introduced by Guo et al.: The SPB consist of solid PS particles of approximately 100 nm diameter ( $R_H \approx 50$  nm) bearing a dense layer of tethered cationic polyelectrolytes. The brush thickness  $L$  of the polyelectrolyte shell depends, on the conditions of polymerization, pH value and ionic strength in between 10 und 200 nm.  $L$  consists in the scheme of poly(2-amino ethyl methacrylate)-hydrochloride. The structure of one monomer unit is depicted on the right hand side. The distance  $D$  of two polyelectrolyte chains at the surface of the PS core is determined by the thickness of occupation.<sup>[30]</sup>

The given core-shell latex consists of a PS core bearing polyelectrolyte chains. The terminology brush means a shell of polymer chains bound to the surface (PS core). The neighbouring chains clearly overlap.<sup>[34]</sup> Because of the highly covered surface of non-charged polymer chains the geometric dimensions becomes interacted in a good solvent. Because of the steric interaction of single chain segments stretching of the bounded polymer chains result.<sup>[35,36]</sup> About this points the shell thickness  $L$  of the polymer brush is a function of the polymer chains,

the solvent, also the occupation thickness of chains. The distance  $D$  of two polyelectrolyte chains at the surface of the PS core is determined by the thickness of occupation. Physically the distances  $D$  of each point of contact have to be smaller than the radius of gyration  $R_G$  (Fig. 1.6).

In the following part some physical facts for charged brushes are discussed in detail. The highly charged brush system affects a strong localisation of the counter ions inside the brush.<sup>[37]</sup> The osmotic pressure causes a clear stretching of the polyelectrolyte chains. Jusufi *et al.* showed by molecular dynamics (MD)-simulations, that in star-branched polyelectrolytes the counter ions are free inside the star or along the stretched polyelectrolyte chain are located.<sup>[38]</sup> Theoretical description of the charged brush particles and the respective conformations is possible by the studies of Jusufi.<sup>[39-42]</sup> Guo *et al.* demonstrate that the brush thickness is depending not only on the  $pH$  value, but also on the ionic strength and the occupation of the surface of the PS core.<sup>[33]</sup>

The principle of the localized counter ions is used for the synthesis introduced by Sharma *et al.* (Fig. 1.7). Starting from the poly(2-amino ethyl methacrylate)-hydrochloride-system [I], the  $Cl^-$ -ions are exchanged against  $AuCl_4^-$ -ions by ion exchange [III]. The following reduction by  $NaBH_4$  is generating the system [IV]. The AuNP are localized inside the polyelectrolyte layer. Figure 1.4 shows some TEM micrographs of the synthesized systems.<sup>[28]</sup>



**Figure 1.7:** Schematic representation of the formation of gold nanoparticles on the surface of the core-shell system. The core-shell system having a shell of poly(2-amino ethyl methacrylate)-hydrochloride-system [I] is de-protonated reversibly at high pH to give amine shell system [II]. [I] and [II] can be used for a counter ion exchange with  $\text{HAuCl}_4$  [III]. Reduction of [III] with  $\text{NaBH}_4$  forms [IV] with nanosized gold particles.<sup>[28]</sup>

## 1.6 Application of Gold Nanoparticles and Binary Metal Nanoalloys in Catalysis

First theoretical considerations of the catalytic application of nanoparticles were introduced by Henglein.<sup>[43]</sup> These preliminary studies on catalytic activity of different MeNP has led to widespread research in the last 20 years.<sup>[2]</sup> For many NP interesting catalytic effects could be observed.

AuNP are the most studied NP in this research area: One reason for the interest in nanogold is the catalytic activity of nanoparticles and zero activity of bulk metal gold.<sup>[5,6]</sup> Because of the quantum-size effect at this length scale.<sup>[5,44-47]</sup>

One issue of the Journal of Applied Catalysis A: General<sup>[48]</sup>, for example, is dedicated to heterogeneous catalysis with AuNP. Graham *et al.* showed that AuNP immobilized on carbon material activated molecular oxygen. After that it is possible to oxidize alkenes to epoxides under mild conditions at atmospheric pressure and temperatures between 60° C and 80° C.<sup>[49]</sup> Yoon *et al.* reported



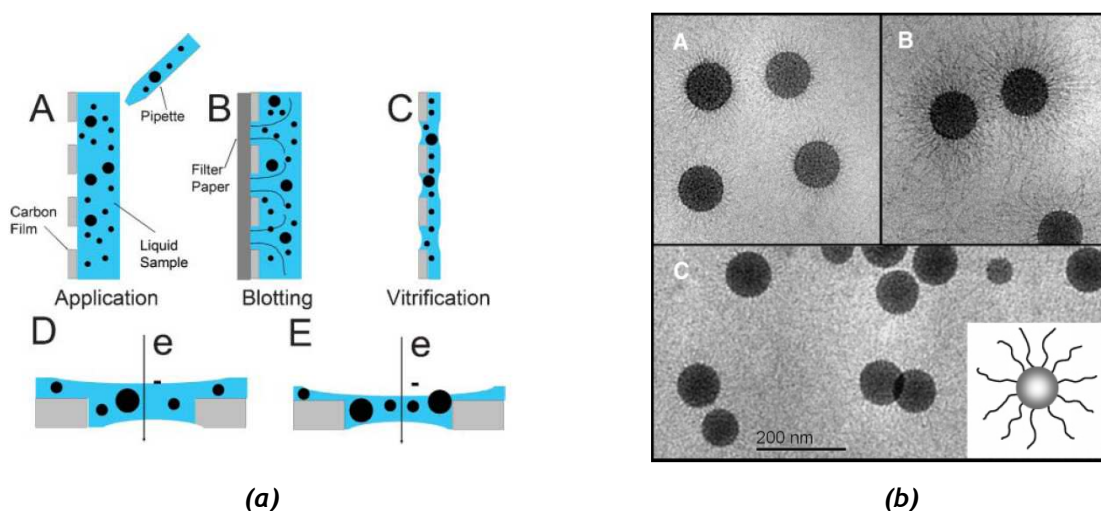
about the gold octamer species  $\text{Au}_8$ . It is possible to realize the conversion of CO to  $\text{CO}_2$  on magnesium oxide at room temperature.<sup>[50]</sup> Tsunoyama *et al.* showed that a size specific catalytic activity of polymer stabilized gold nanoclusters for aerob conditions alcohol oxidation in water exists. The oxidation of benzyl alcohol derivatives to the respective benz aldehyde derivatives and benzoic acid derivatives was also reported.<sup>[46]</sup>

For kinetic studies with nanoparticles the model reduction 4-nitrophenol to 4-aminophenol was introduced by Pal *et al.* in 2004.<sup>[51]</sup> The application for Pt- and Pd- composite systems was carried out by Mei *et al.*<sup>[52,53]</sup> It was examined that binary gold-platinum nanoalloys show a better catalytic activity in comparison to both monometallic nanoparticles.<sup>[2,54-57]</sup> Enache *et al.* reported about the excellent catalytic properties of binary Au-Pd nanocrystals for oxidation reactions from primary alcohols.<sup>[11]</sup> There are also reports of the application of Au-Pt nanoparticles in electro catalysis.<sup>[12,13]</sup>

## 1.7 Transmission Electron Microscopy

For a better understanding of SPB composite systems imaging methods are essential. In this context transmission electron microscopy (TEM) is a predicative examination method for polyelectrolyte/MeNP composite systems and also for the generated metal nanoparticles.<sup>[28,58]</sup> It is possible to image both carrier particles and MeNP by this method, because both particles (systems) are in the resolution limits of this apparatus (of the microscope). In particular the method of cryogenic transmission electron microscopy (cryo-TEM) in combination with special methods of preparation<sup>[59]</sup> offers new possibilities. The fundamentals of this method and their application to problems in the area of colloid chemistry was established by Talmon.<sup>[60]</sup> Figure 1.8 shows the preparation of a polymer dispersion sample by this method in a schematic fashion.<sup>[59]</sup> A drop of the liquid sample is applied onto a perforated carbon film supported on a TEM copper grid (A). The solvent is blotted by an absorbing filter paper (B). In the next step the sample is rapidly plunged into a cyrogen reservoir. During this process a vitrified film (C) is developed, which can be of different thickness (D and E).<sup>[59]</sup> It is possible to make the structures in solution visible by cryo-TEM. The

application of this method to spherical polyelectrolyte systems was established by Wittemann *et al.*<sup>[58]</sup> (Fig. 1.8 (b)). The micrographs show anionic SPB (C). The contrast of the polyelectrolyte chains is enhanced compared to the original particles (C) by replacing the  $\text{Na}^+$  counter ions of the polyelectrolyte chains by  $\text{Cs}^+$ -ions (A) and additionally by bio molecules (B). For the explanation of nanoparticular structures different methods of high resolution transmission electron microscopy (HR-TEM) are well suited.<sup>[61-63]</sup>



**Figure 1.8 a and b:** Preparation of a cryo-TEM sample by Talmon (a).<sup>[59]</sup> Cryo-TEM images of vitrified 1 wt-% SPB suspensions (b). The contrast is enhanced compared to the original particles (C) by replacing the  $\text{Na}^+$  counter ions of the polyelectrolyte chains by  $\text{Cs}^+$ -ions (A) and, additionally, by BSA molecules (537 mg per g SPB) which are adsorbed in close correlation to the polyelectrolyte chains (B).<sup>[58]</sup>

## 1.8 Objectives of this Thesis

Starting from Sharma's work first of all the process of generation of AuNP@SPB should be understood in detail, as well as the structure of the nanoparticles. (Chapter 2.3 and 3.3). For this purpose different methods, like dynamic light scattering (DLS), transmission electron microscopy methods (TEM) and wide angle X-Ray scattering (WAXS) should be used. In the following part the synthesis of the carrier particles should be modified, so that synthesis of high volumina with high solid content in a reproducible way is possible (Chapter 2.1 and 3.1). First of all a PS core with low polydispersity with a polymerized shell of the photo initiator Methacrylic-acid-2-[4-(2-hydroxy-2-methyl-propionyl)-phenoxy]-ethylester (HMEM) should be synthesized in an emulsion polymerization.<sup>[32]</sup> On

the surface of this system polyelectrolyte chains of 2-amino ethyl methacrylate-hydrochloride (AEMH) should be grafted after initiation by UV light. The synthesized dispersions should be characterized by different methods, like dynamic light scattering (DLS), disc centrifuge (DCP) and transmission electron microscopy (TEM) and cryogenic TEM (cryo-TEM) (Chapter 2.2 and 3.2).

These carrier particles are used for the stabilization of binary gold nanoalloys, which are directly generated inside the brushes attached to the surface of the PS core (Chapter 2.4, 3.4 and 3.6). The obtained nanoalloys should be also characterized in detail by different methods, like high resolution TEM (HR-TEM) and WAXS. The structure should be studied in detail. After the examinations relations between structure and properties should be established. Followed by this analysis in the next step a comparison between nanoalloys and bulk alloys has to be performed. Finally faceted nanoparticle geometries should be generated and characterized (Chapter 2.5 and 3.5).

Moreover, in a second part of this thesis the generated gold nanoparticles and binary gold nanoalloys are tested on their catalytic activity for the oxidation of alcohols (Chapter 3.4) and for epoxidation reactions (Chapter 3.6). All products are of interest for industry. In this connection relations between particle composition and morphology, and also size should be examined (Chapter 2.6).

## 1.9 References

- [1] Willner, I.; Katz E. *Angew. Chem* **2004**, *116*, 6166.
- [2] Astruc, D.; Lu, F.; Aranzaes, J. R. *Angew. Chem* **2005**, *117*, 8062.
- [3] Hashmi, A. S. K. *Chem. Rev.* **2007**, *107*, 3180.
- [4] Yamada, Y. M. A.; Arakawa, T.; Hocke, H.; Uozumi, Y. *Angew. Chem.* **2007**, *119*, 718.
- [5] Daniel, M.-C.; Astruc, D. *Chem. Rev.* **2004**, *104*, 293.
- [6] Gosh, S. K.; Pal, T. *Chem. Rev.* **2007**, *107*, 4797.
- [7] Alivisatos, A. P. *Science* **1996**, *271*, 933.
- [8] Brust, M.; Kiely, C. J. *Colloids Surf. A: Physicochem. Eng. Asp.* **2002**, *202*, 175.
- [9] Pyykkö, P. *Angew. Chem.* **2004**, *116*, 4512.
- [10] Ferrando, R.; Jellinek, J.; Johnston, R. L. *Chem. Rev.* **2008**, *108*, 845.
- [11] Enache, D. I.; Edwards, J.; Landon, P.; Solsona-Espriu, B.; Carley, A. F.; Herzing, A. A.; Watanabe, M.; Kiely, C. J.; Knight, D. W.; Hutchings, G. J. *Science* **2006**, *311*, 362.
- [12] Lou, Y.; Maye, M. M.; Han, L.; Luo, J.; Zhong, C.-J. *Chem. Commun.* **2001**, 473.
- [13] Stamenkovic, V. R.; Mun, B. S.; Arenz, M.; Mayrhofer, K. J. J.; Lucas, C. A.; Wang, G.; Ross, P. N.; Markovic, N. M. *Nater. Mater.* **2007**, *6*, 241.
- [14] Lou, J.; Maye, M. M.; Petkov, V.; Kariuki, N. N.; Wang, L.; Njoki, P.; Mott, D.; Lin, Y.; Zhong, C.-J. *Chem. Mater.* **2005**, *17*, 3086.
- [15] Bond, G. C. *Platinum Met. Rev.* **2007**, *51*(2), 63.
- [16] Mott, D.; Luo, J.; Smith, A.; Njoki, P. N.; Wang, L.; Zhong, C.-J. *Nanoscale Res. Lett.* **2007**, *2*, 12.
- [17] Jin, R.; Cao, Y. W.; Mirkin, C. A.; Kelly, K. L.; Schatz, G. C.; Zheng, J. G. *Science* **2001**, *294*, 1901.
- [18] Sun, Y.; Xia, Y. *Science* **2002**, *298*, 2176.
- [19] Narayanan, R.; El-Sayed, M. A. *J. Am. Chem. Soc.* **2004**, *126*, 7194.
- [20] Burda, C.; Chen, X.; Narayanan, El-Sayed, M. A. *Chem. Rev.* **2005**, *105*, 1025.
- [21] Tian, N.; Zhou, Z.-Y.; Sun, S.-G.; Ding, Y.; Wang, Z. L. *Science* **2007**, *316*, 732.

- [22] Ahmadi, T. S.; Wang, Z. L.; Green, T.C.; Henglein, A.; El-Sayed, M. A. *Science* **1996**, 272, 1924.
- [23] Narayanan, R.; El-Sayed, M. A. *J. Phys. Chem. B* **2003**, 107, 12416.
- [24] Narayanan, R.; El-Sayed, M. A. *Nano Lett.* **2004**, 4, 1343.
- [25] Johnson, C. L.; Snoeck, C. L. E.; Ezcurdia, M.; Rodriguez-Gonzalez, B.; Pastoriza-Santos, I.; Liz-Marzan, L. M.; Hytch, M. *Nater. Mater.* **2008**, 7, 120.
- [26] Pastoriza-Santos, I.; Liz-Marzan, L. *Nano Lett.* **2002**, 2, 903.
- [27] Schmid, G.; Corain, B. *Eur. J. Inorg. Chem.* **2003**, 3081.
- [28] Sharma, G.; Ballauff, M. *Macromol. Rapid Commun.* **2004**, 25, 547.
- [29] Gopidas, K. R.; Whitesell, J. K.; Fox, M. A. *J. Am. Chem. Soc.* **2003**, 125, 6491.
- [30] Guo, X.; Weiss, A.; Ballauff, M. *Macromolecules* **1999**, 32, 6043.
- [31] Ballauff, M. *Progr. Polym. Sci.* **2007**, 32, 1135.
- [32] Mei, Y.; Wittemann, A.; Sharma, G.; Ballauff, M. *Macromolecules* **2003**, 36, 3452.
- [33] Guo, X.; Ballauff, M. *Langmuir* **2000**, 16, 8719.
- [34] Advincula, R. C.; Brittain, W. J.; Caster, K. C.; R  he, J. *Polymer Brushes (Synthesis, Characterization, Applications)*, Wiley-VCH, Weinheim **2004**.
- [35] Alexander, S.; Chaikin, P. M.; Grant, P.; Morales, G. J.; Pincus, P. A. *J. Chem. Phys.* **1984**, 80, 5776.
- [36] de Gennes, P. G. *J. Physique* **1976**, 37, 1976.
- [37] Pincus, P. *Macromolecules* **1991**, 24, 1912.
- [38] Jusufi, A.; Likos, C. N.; L  wen, H. *J. Chem. Phys.* **2002**, 116 (24), 11011.
- [39] Witten, T. A.; Pincus, P. A. *Macromolecules* **1986**, 19, 2509.
- [40] Ligoure, C.; Leibler, L. *Macromolecules* **1990**, 23, 5044.
- [41] Halperin, A.; Tirell, M.; Lodge, T. P. *Adv. Polym. Sci.* **1992**, 100, 31.
- [42] Jusufi, A.; Likos, C. N.; Ballauff, M. *Colloid Polym Sci* **2004**, 282, 910.
- [43] Henglein, A. *J. Phys. Chem.* **1993**, 97, 5457.
- [44] Negishi, Y.; Tsukuda, T. *J. Am. Chem. Soc.* **2003**, 125, 4046.
- [45] Tsunoyama, H.; Sakurai, H.; Ichikuni, N.; Negishi, Y.; Tsukuda, T. *Langmuir* **2004**, 20, 11293.

- [46] Tsunoyama, H.; Sakurai, H.; Negishi, Y.; Tsukuda, T. *J. Am. Chem. Soc.* **2005**, *127*, 9374.
- [47] Landon, P.; Ferguson, J.; Solsona, B. E.; Garcia, T.; Carley, A. F.; Herzing, A. A.; Kiely, C. J.; Golunski, S. E.; Hutchings, G. J. *Chem. Commun.* **2005**, *27*, 3385.
- [48] *Applied Catalysis A: General* **2005**, 291.
- [49] Hughes, M. D.; Xu, Y.-J.; Jenkins, P.; McMorn, P.; Landon, P.; Enache, D. I.; Carley, A. F.; Attard, G. A.; Hutchings, G. J.; King, F.; Stitt, E. H.; Johnston, P.; Griffin, K.; Kiely, C. J. *Nature* **2005**, *437*, 1132.
- [50] Yoon, B.; Häkkinen, H.; Landman, U.; Wörz, A. S.; Antonietti, J.-M.; Abbet, S.; Judai, K.; Heiz, U. *Science* **2005**, *307*, 403.
- [51] Praharaj, S.; Nath, S.; Gosh, S. K.; Kundu, S.; Pal, T. *Langmuir* **2004**, *20*, 9889.
- [52] Mei, Y.; Sharma, G.; Lu, Y.; Drechsler, M.; Irrgang, T.; Kempe, R.; Ballauff, M. *Langmuir* **2005**, *21*, 12229.
- [53] Mei, Y.; Lu, Y.; Polzer, F.; Ballauff, M.; Drechsler, M. *Chem. Mater.* **2007**, *19*, 1062.
- [54] Hill, C. L. *Advances in Oxygenated Processes*, Vol. 1, Jal Press, London **1988**.
- [55] Hundlucky, M. *Oxidations in Organic Chemistry*, ACS, Washington DC **1990**.
- [56] Mallat, T.; Baiker, A. *Chem. Rev.* **2004**, *104*, 3037.
- [57] Anderson, R. A.; Griffin, K.; Johnson, P.; Alsteres, P. L. *Adv. Synth. Catal.* **2003**, *345*, 517.
- [58] Wittemann, A.; Drechsler, M.; Talman, Y.; Ballauff, M. *J. Am. Chem. Soc.* **2005**, *127*, 9688.
- [59] Cui, H.; Hodgdon, T.K.; Kaler, E. W.; Abezgauz, L.; Danino, D.; Lubovsky, M.; Talmon, Y.; Pochan, D. J. *Soft Matter* **2007**, *3*, 945.
- [60] Talmon, Y.; Evans, D. F.; Ninham, B. W. *Science* **1983**, *221*, 1047.
- [61] *Microscopy and Microanalysis* **2008**, 1.
- [62] Kuo, K. H.; Ye, H. Q.; Li, D. X. *Journal of Electron Microscopy Technique* **1986**, *3*, 57.
- [63] Martin, D. C.; Chen, J.; Yang, J.; Drummy, L. F.; Kübel, C. J. *Polym. Sci. Part B: Polym. Phys.* **2005**, *43*, 1749.

## 2 Overview of this Thesis – Results

This thesis contains six publications, introduced in Chapter 3.1 up to 3.6.

First of all, the up scaled synthesis of anionic and cationic spherical polyelectrolyte brushes (SPB) were introduced and the method characterized in detail to synthesize reproducible SPB. The resulting systems were characterized concerning their physico chemical properties. After that the anionic and cationic SPB were compared with each other (Chapter 3.1). Now the synthesized anionic SPB are used for the examination of the interaction between polyelectrolyte chains and a cationic surfactant. The resulting systems and effects were studied in detail by cryo-TEM (Chapter 3.2).

In a following work the cationic SPB was used for the generation of gold nanoparticles. The resulting systems were characterized in detail by different TEM methods. The catalytic activities of the composite systems were checked as well (Chapter 3.3).

Given the results from Chapter 3.3 more sophisticated Au-Pt nanoalloys@SPB were generated. These composite systems were characterized by different HR-TEM methods. Finally the catalytic activity for alcohol oxidation reactions were determined (Chapter 3.4).

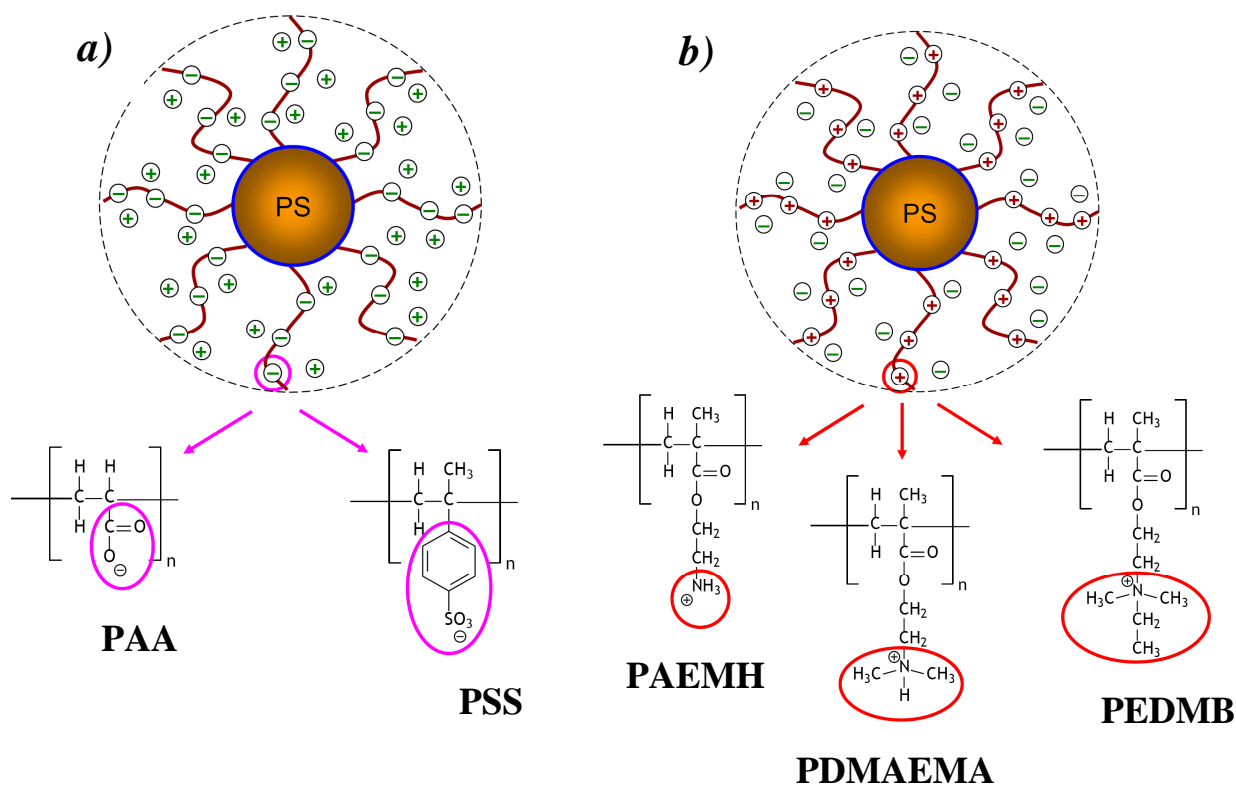
The binary gold nanoalloys serve as a template for the generation of faceted platinum nanocrystals. The special geometric morphology was characterized in detail and also checked by the model reaction known from Chapter 3.3 (Chapter 3.5).

Finally this knowledge was used to synthesize more nanoalloys, which were characterized in detail. The catalytic activities of these nanoalloys were examined for epoxidation reactions (Chapter 3.6).

In the following Chapters 2.1 up to 2.5 the main results of the publications (Chapter 3.1 up to 3.6) are summarized. The experimental details can be found in each publication.

## 2.1 Synthesis and Characterization of SPB

SPB are colloidal particles in the range of 300 nm. Figure 2.1 shows the structure of two different types of these polymer particles.



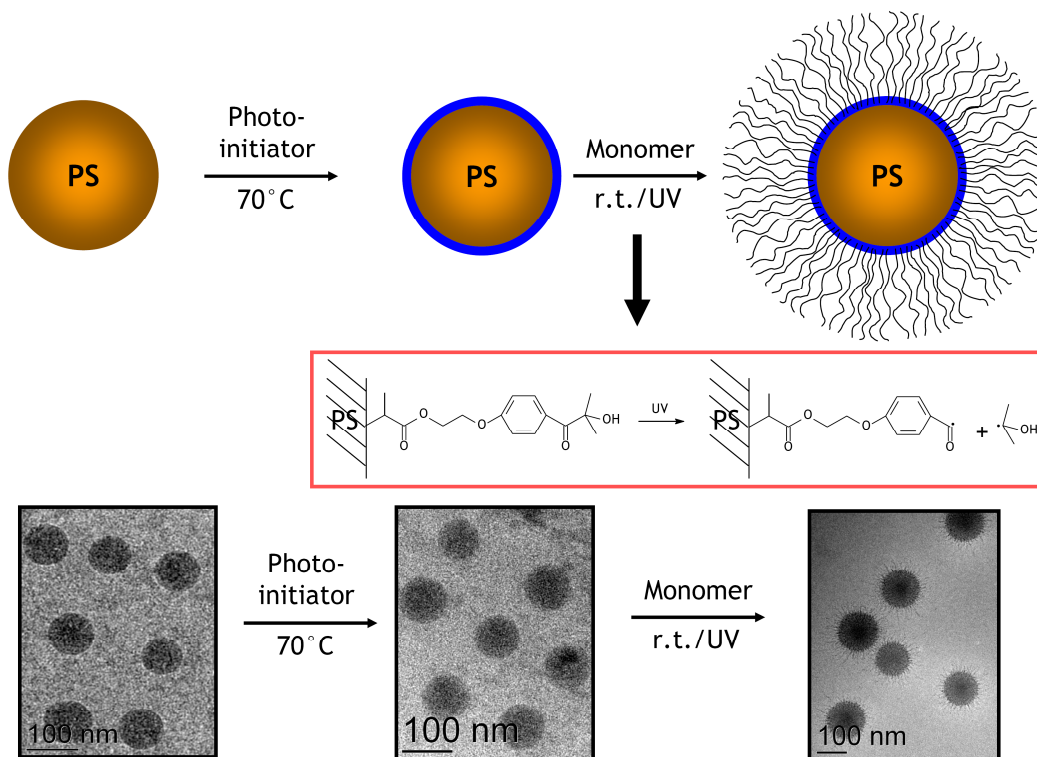
**Figure 2.1 a and b:** The SPB consist of solid PS particles of approximately 100 nm diameter bearing a dense layer of tethered anionic (a) or cationic polyelectrolytes (b). If chains of weak polyelectrolytes such as PAA and PAEMH are attached, the degree of charges of the SPB depends strongly on the pH, and as a consequence the electrostatic stabilization of the particles is influenced by the external pH. However, if chains of the strong polyelectrolytes PSS and PEDMB are bound, the amount of charges onto the SPB does not depend on the pH.

Starting from a solid polystyrene core (PS core) (diameter around 100 nm) polyelectrolyte chains with a shell thickness  $L$  around 70 nm are tethered. The polyelectrolyte chains are anionic (Fig. 2.1 (a)) or cationic (Fig. 2.1 (b)). Typically anionic monomers are acrylic acid (AA) and styrene sulfonate (SS). In case of cationic polyelectrolytes often 2-amino ethyl methacrylate (AEMH) is used. Depending on the ionic strength the shell thickness  $L$  changes.

The synthesis of the polymer particles is shown in a schematic fashion in Figure 2.2. Starting from a PS core ( $R_H = 50$  nm), with low polydispersity, synthesized in emulsion polymerization. In the second step the photo initiator 2-[p-(2-hydroxy-



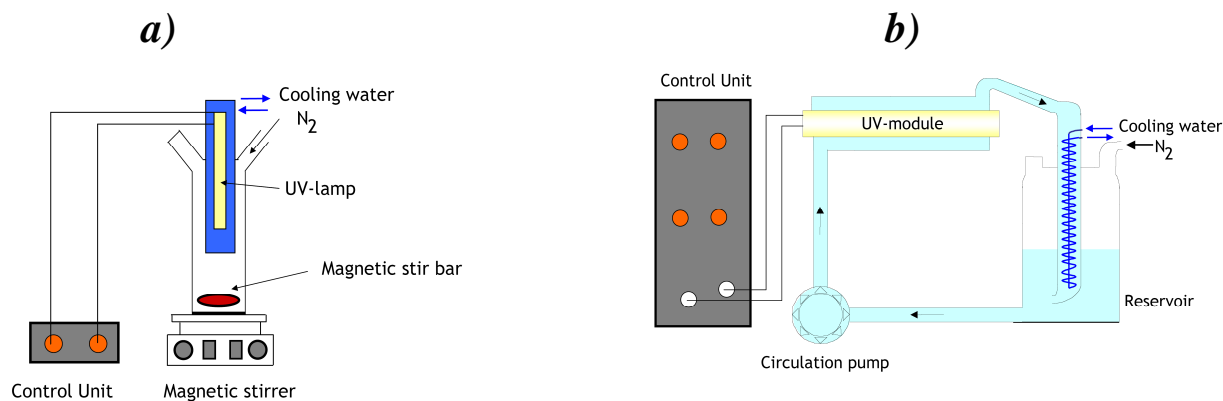
2-methyl-propio(phenone)]-ethylene glycol-methacrylate (HMEM) is added to the reaction to form a thin shell which is used in the third step as initiator. In the last step radicals are generated under UV for the polymerization process of the polyelectrolyte chains. All particle stages are visible by cryo-TEM.



**Figure 2.2:** Preparation of latex particles stabilized with long polyelectrolyte chains: at first polystyrene spheres were prepared by emulsion polymerization. The PS particles were coated with a thin layer of a polymerizable photo initiator at a given conversion of styrene. The seed particles were extensively purified by ultrafiltration against water. Water-soluble monomers such as acrylic acid or styrene sulphuric acid were added. UV irradiation of the suspension led to surface-bound radicals and free radicals in solution. Both types of radicals initiated the polymerization of the water-soluble monomer. Hence, both polyelectrolyte chains anchored onto the PS seed particles and free chains in solution were obtained. The free chains in solution were removed by ultrafiltration. Cryo-TEM micrographs demonstrate that well-defined core-shell particles can be made by this technique.

Figure 2.3 shows the comparison of both photo reactors used for the synthesis of SPB. Thus we were looking for a technique which facilitates the process of photo emulsion polymerization. We assigned the reaction described in Ref.<sup>[1]</sup> to a commercial UV reactor system (aqua concept Laboclean LC Forschungsreaktor, Karlsruhe, Germany), which has been designed for water and liquid waste treatment, i.e., applications that involve large throughputs or poor transmission (Fig. 2 (b)). After adaption to the present purpose, this novel reactor largely

improves the efficiency of the photo emulsion polymerization by reduced reaction times (Fig. 2 (a): 6h; Fig. 2 (b): 25 min), larger scales and reproducible reaction conditions. A detailed study on the formation of polyelectrolyte brushes onto model latexes using the novel UV reactor is presented.



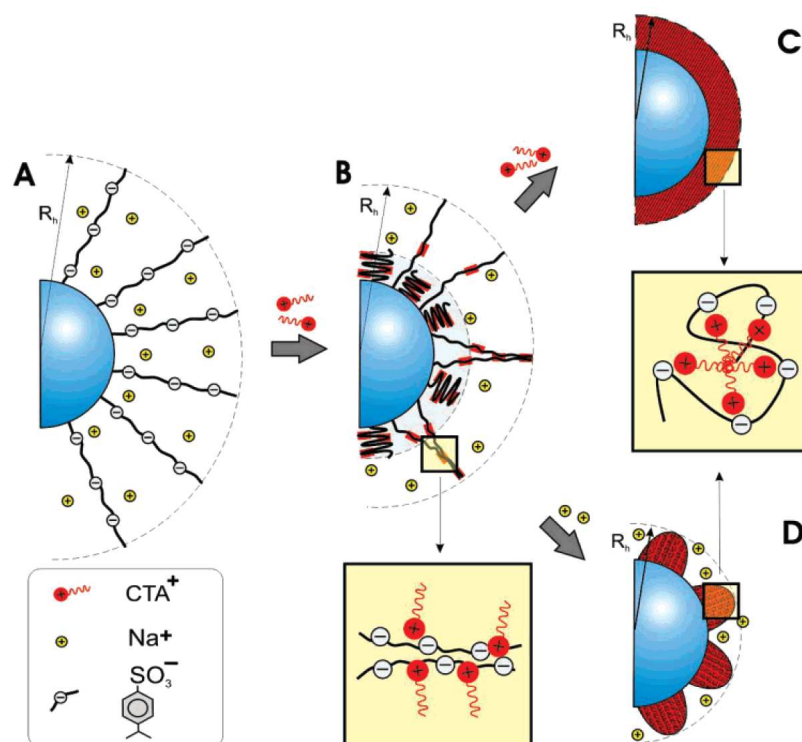
**Figure 2.3 a and b:** Photoreactor systems used to conduct photo emulsion polymerization: the schematic representation on the left (a) shows the reactor used by Guo et al.<sup>[1]</sup> A medium pressure mercury lamp (TQ 150 Z3, Heraeus Noblelight, Hanau, Germany; range of wave lengths 200-600 nm, power consumption 150W) surrounded by a cooling quartz tube was directly placed in a 650 ml reactor glass vessel. The right-hand illustration (b) gives a schematic rendition of the UV reactor (aqua concept Laboclean LC Forschungsreaktor, Karlsruhe, Germany) used in the present study. The suspension circulates continuously from a reservoir (here: 3000 ml) into a UV radiation chamber (power consumption reduced to 500 W) and via a condenser back into the reservoir. This setup allows for variable batch sizes that only depend on the size of the reservoir. Continuous circulation of the suspension allows for a highly turbulent flow and prevents the formation of deposits. Moreover, the electronic performance of the UV module enables reliable accuracy of the UV irradiation.

A detailed description of all experiments and results can be found in Chapter 3.1.

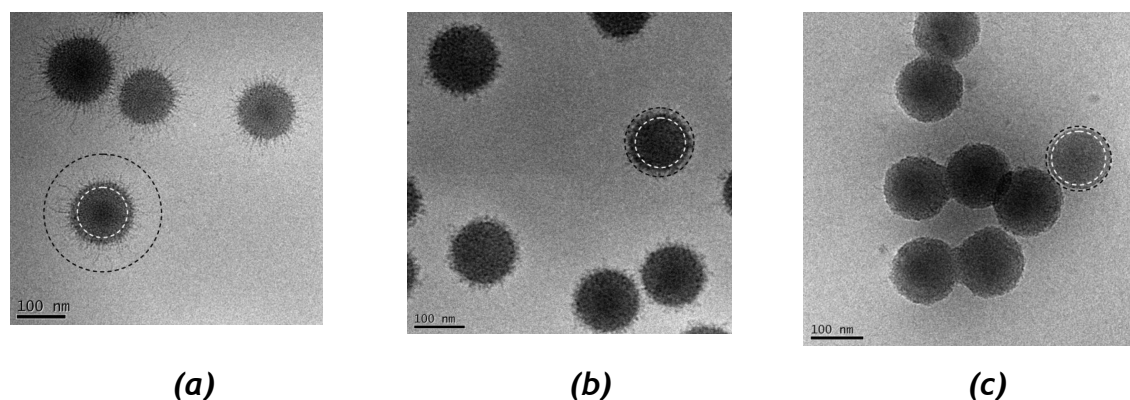
## 2.2 Structure Studies of SPB

For a better understanding of the interaction between anionic SPB and cationic surfactants<sup>[2]</sup> the formation of a complex between an anionic spherical polyelectrolyte brush and the cationic surfactant cetyl trimethyl ammonium bromide (CTAB) is investigated. The SPB consists of long chains of the strong polyelectrolyte poly(styrene sulfonate) (PSS), which are bound chemically to a

solid poly(styrene) core 56 nm radius. The SPB are dispersed in water, and the ionic strength is adjusted by addition of NaBr. The resulting complexes are investigated in dilute solution by dynamic light scattering (DLS) and by cryo-TEM. The different models of the complexation are depicted in Figure 2.4. It is clearly visible, that, depending on the amount of CTAB and NaBr different complexes are built. **(A)** shows the SPB before the addition of salt and surfactant. **(B)** and **(C)** show the changed structures after addition of salt and surfactant. The interaction of the polyelectrolytes with surfactant and high ionic strength is followed by a contraction **(D)**. All stages are examined by cryo-TEM (Fig. 2.5). The formation of the complex between the SPB and the surfactant can be monitored by a strong shrinking of the surface layer when adding CTAB to dilute suspensions (0.01 wt-%) and by a decrease of the effective charge of the complexes. Complex formation starts at CTAB concentrations lower than the critical micelle concentration of this surfactant. If the ratio  $r$  of the charges on the SPB to the charge of the added surfactant exceeds one the particles start to flocculate. Cryo-TEM images of the complexes at  $r = 0.6$  measured in salt-free solution show that the surface layer composed of the PSS chains and the adsorbed CTAB molecules has partially collapsed: A part of the chains form a dense surface layer while another part of the chains or aggregates thereof still stick out. This can be deduced from the cryo-TEM micrographs as well as from the hydrodynamic radius, which is still of appreciable magnitude. The 1:1 complex ( $r = 1.0$ ) exhibits a fully collapsed layer formed by the PSS chains and CTAB. If the complex is formed in the presence of 0.05 M NaBr,  $r = 0.6$  leads to globular structures directly attached to the surface of the core particles. All structures seen in the cryo-TEM images can be explained by a collapse transition of the surface layer brought about by the hydrophobic attraction between the polyelectrolyte chains that became partially hydrophobic through adsorption of CTAB.



**Figure 2.4:** Schematic model of the spatial structure of the complexes from spherical polyelectrolyte brushes and the cationic surfactant CTAB. Model A corresponds to the spherical polyelectrolyte brush in salt-free solution, that is, with sodium counterions. Models B and C refer to the complex of the brush particles with CTAB at  $r = 0.6$  (B) and  $r = 1.0$  (C) at a low ionic strength. Model D refers to the structure formed by the brush particles and the surfactant at a higher ionic strength (50 mM NaBr).



**Figure 2.5 (a) – (c):** Cryo-TEM images of different systems, described in Figure 2.5. (a) shows the SPB dispersion in salt- and surfactant free solution. (b) shows the system after addition of surfactant and NaBr. (c) shows the system after addition of a huge amount of surfactant.

A detailed description of all experiments and results can be found in Chapter 3.2.

### 2.3 Synthesis and Characterization of Gold Nanoparticles

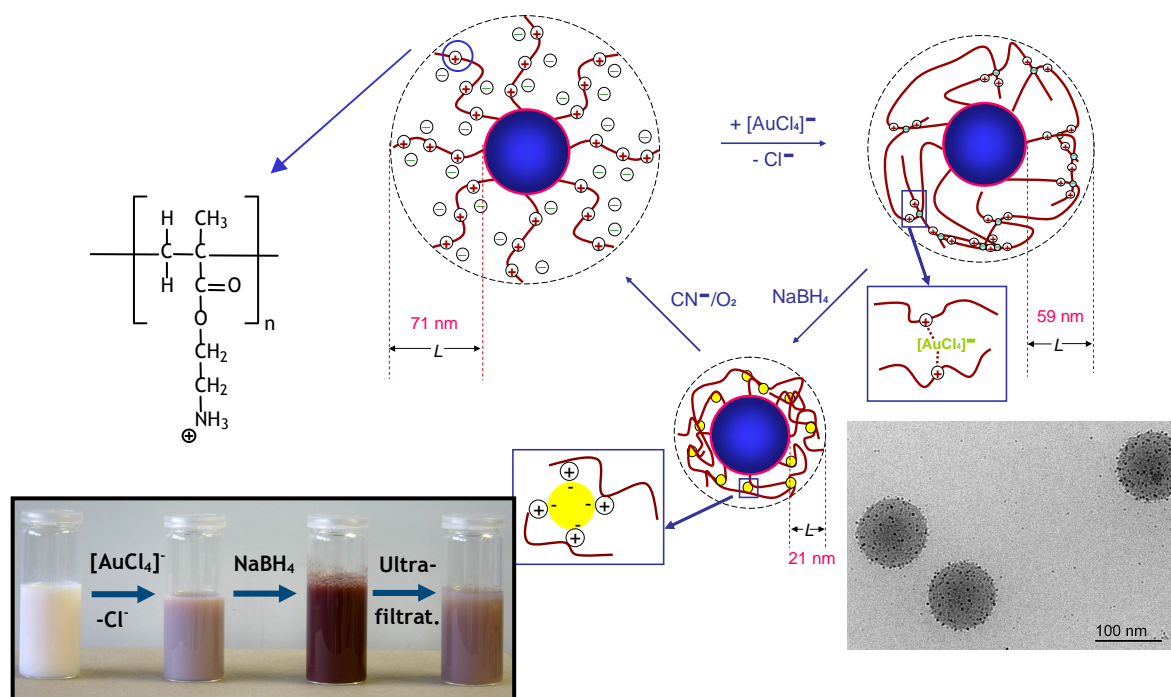
The SPB with the polyelectrolyte chains of poly(2-amino ethyl methacrylate) presented in Chapter 2.1 are used for the generation of AuNP, now.

Figure 2.6 displays all results for the generation of AuNP in a schematic fashion. Starting with the SPB with  $\text{Cl}^-$  counter-ions, these are exchanged against  $\text{AuCl}_4^-$  ions. The introduced anions are complexed by the polyelectrolyte chains. The following ultrafiltration removed not complexed  $\text{AuCl}_4^-$  ions from the dispersion medium. The  $\text{AuCl}_4^-$  ions are partially complexed by the polyelectrolyte chains. In this way the  $\text{AuCl}_4^-$  ions create a densely cross linked mesh of polyelectrolyte chains. The local concentration of  $\text{AuCl}_4^-$  ions is, therefore, enlarged considerably. In the next step the reducing agent  $\text{NaBH}_4$  is added. Introducing  $\text{CN}^-$  ions and  $\text{O}_2^{[3]}$  leads to dissolution of the AuNP.

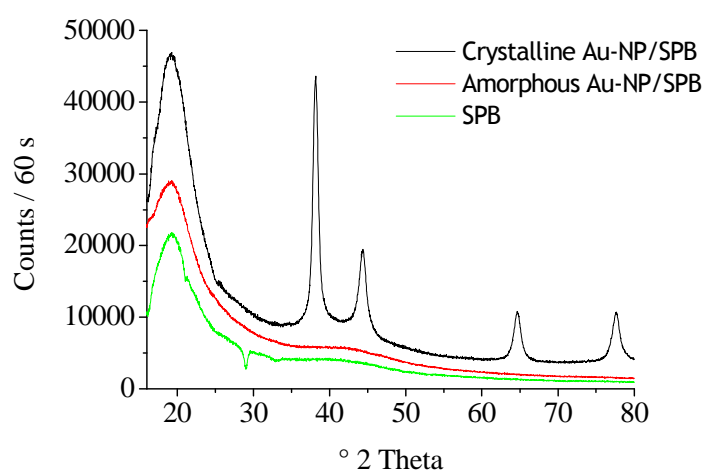
All stages of the formation of the nanoparticles within the brush layer can be followed easily by DLS, which determines the hydrodynamic radius  $R_H$  of the particles. The present data, therefore, point to the preferred formation of small and amorphous particles if the reduction is slow. The Au-NP content of the composite particles could be varied from 7.5 – 9.5 wt.-% by using an excess of  $\text{NaBH}_4$  during the reduction. Systematic cryo-TEM studies showed that the size of the AuNP could be varied between 1.0 and 3.0 nm by varying the amount of bound  $\text{AuCl}_4^-$  ions.

Studies of the generated Nanoparticles on SPB by HR-TEM and WAXS (Fig. 2.7) showed an amorphous structure.

A detailed description of all experiments and results is presented in Chapter 3.3.



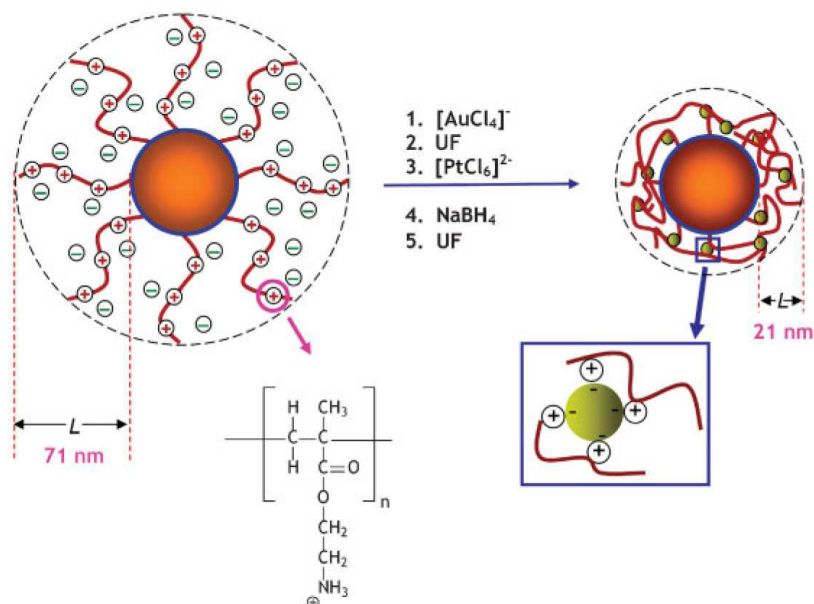
**Figure 2.6:** Scheme for the generation of AuNP and their dissolution with  $\text{CN}^-$ -ions/ $\text{O}_2$ . In the first step  $\text{Cl}^-$  ions are exchanged against  $[\text{AuCl}_4]^-$  ions. The excess  $[\text{AuCl}_4]^-$  ions are removed subsequently by ultrafiltration. Replacing  $\text{Cl}^-$  ions by  $[\text{AuCl}_4]^-$  ions leads to a decrease of the layer thickness  $L$  from 71 to 59 nm. In the next step AuNP are generated by reduction of the confined  $[\text{AuCl}_4]^-$  counter-ions by  $\text{NaBH}_4$ . Here,  $L$  decreased to only 21 nm. In the last step AuNP are dissolved by complexation with  $\text{CN}^-$ -ions/ $\text{O}_2$ . The original thickness of the surface layer is recovered in this step.



**Figure 2.7:** Results of WAXS measurements of the AuNP on the spherical polyelectrolyte brushes. The uppermost scattering curve shows the WAXS diagram for crystalline AuNP of around 3 nm. In the middle, the scattering curve for amorphous AuNP on SPB is shown. The lowermost curve is the scattering curve of the carrier particle without AuNP.

## 2.4 Synthesis and Characterization of Binary Gold Nanoalloys

The principles from Chapter 2.3 for gold nanoparticles are now adapted for the generation of binary nanoalloys. Figure 2.8 shows schematically the generation of binary gold nanoalloys. Here we use the example of Au-Pt nanoalloys.



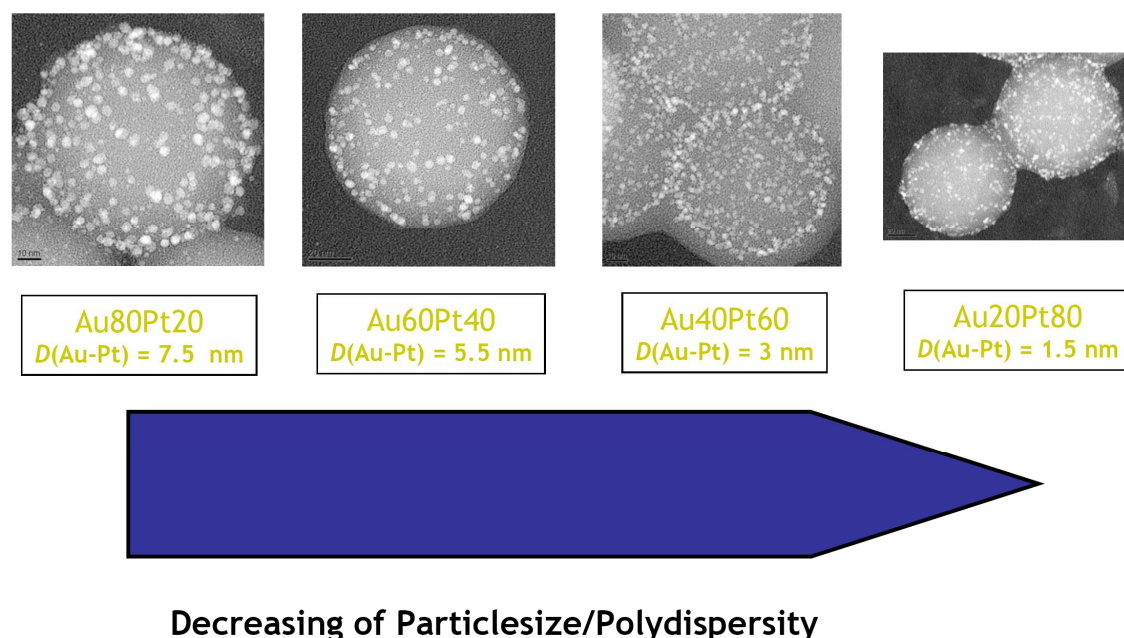
**Figure 2.8:** SPB used as carriers for bimetallic Au-Pt nanoparticles. Linear cationic polyelectrolytes of poly(2-amino ethyl methacrylate) are densely grafted onto a PS core ( $R_H = 45$  nm). The thickness of the polyelectrolyte layer  $L$  is about 71 nm.  $\text{AuCl}_4^-$  and  $\text{PtCl}_6^{2-}$  ions are introduced as counter-ions and reduced within the brush layer to generate bimetallic Au-Pt nanoparticles. In a first step, a given number of the  $\text{Cl}^-$  counter-ions are replaced by  $\text{AuCl}_4^-$  ions. Ultrafiltration removes  $\text{AuCl}_4^-$  ions that have not been complexed. Finally,  $\text{PtCl}_6^{2-}$  ions are introduced and the system is purified again by ultrafiltration. Reduction is achieved by adding  $\text{NaBH}_4$ . All steps can be followed by dynamic light scattering, which allows the thickness  $L$  of the surface layer to be measured.

Starting from cationic polyelectrolyte brushes, first of all a part of  $\text{Cl}^-$  ions are exchanged by  $\text{AuCl}_4^-$  ions.  $\text{AuCl}_4^-$  ions, that are not complexed are replaced by an ultrafiltration. In the next step  $\text{Cl}^-$  ions are exchanged by  $\text{PtCl}_6^{2-}$  ions, before reducing the mixture of metal ions and generating during this step the binary nanoalloys on the surface of the PS core. All single steps of every exchange step can be easily followed by DLS. The shell thickness  $L$  shrinks during the whole exchange process about 50 nm.



With the method described above it is possible to synthesize binary nanoalloys of Au-Pt, Au-Ir, Au-Rh, Au-Ru (Chapter 3.4 and 3.6). In the following part only Au-Pt nanoalloys are discussed in detail.

Figure 2.9 shows different particle geometries and -sizes of Au-Pt nanoalloys. It is obvious that the particle size and distribution on the PS core depends on the composition in the alloy. The higher the gold amount, the bigger the particle becomes and the particle distribution broadens. The detailed characterization by HR-TEM and electron diffraction (Fig. 2.10) shows a crystalline structure of the nanoparticles. Electron dispersive X-ray spectroscopy (EDX) proves the composition in one alloy particle.

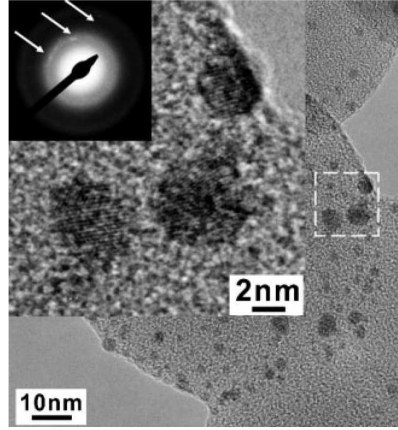


**Figure 2.9:** Au-Pt nanoalloys with different compositions of gold and platinum. The lower the gold amount (left to the right) in the solid solution of the alloy, the smaller the particle size and smaller the size distribution.

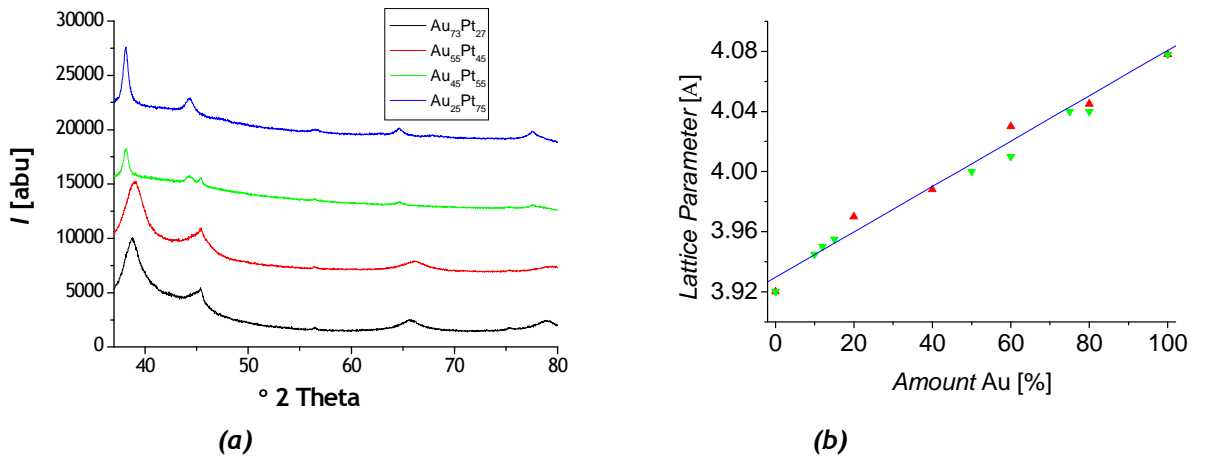
A more detailed analysis of the crystal spacing as a function of the Au/Pt ratio can be done by WAXS. The WAXS diffractograms (Fig. 2.11 (a)) exhibit a marked broadening of the peaks owing to their small size. A similar finding was already reported for Au-Pt nanoparticles synthesized by Lou *et al.*<sup>[4]</sup> The lattice spacing depend linearly on the composition (Vegard's law). The lattice spacing obtained



here are shown in Figure 2.11 (b) together with the data of Lou *et al.* [4,5] This finding is contrary to bulk Au-Pt alloys because of the broad miscibility gap.[6]



**Figure 2.10:** TEM image of  $\text{Au}_{73}\text{Pt}_{27}$  composite particles, with a HR-TEM image of three particles (lattice imaging) and the diffractogram in the insets.

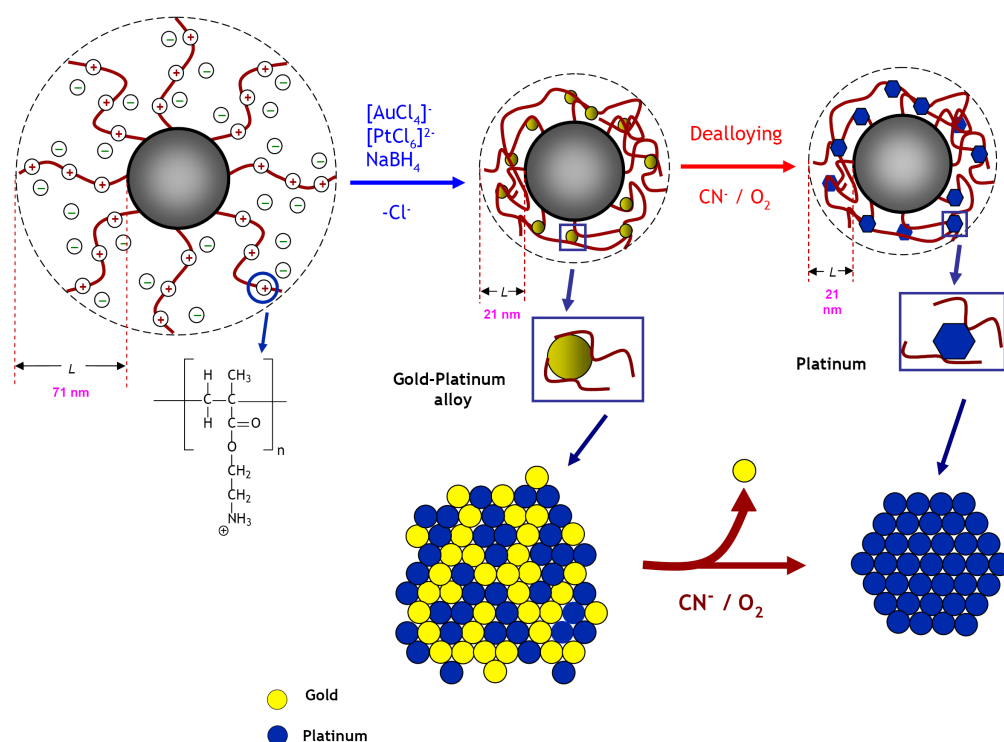


**Figure 2.11 a and b:** Wide angle X-ray scattering intensities of the composite systems  $\text{Au}_{73}\text{Pt}_{27}$ ,  $\text{Au}_{55}\text{Pt}_{45}$ ,  $\text{Au}_{45}\text{Pt}_{55}$ ,  $\text{Au}_{25}\text{Pt}_{75}$  (from bottom to top) (a). Plot of the lattice parameter dependence on the composition of the alloy particle (b). (Red triangles: own measured values; green triangles: data from Zhong *et al.* [4])

A detailed description of all experiments and results for the binary Au-Pt nanoalloys can be found in Chapter 3.4, for binary Au-Ru, Au-Rh and Au-Ir nanoalloys it can be found in Chapter 3.6.

## 2.5 Synthesis and Characterization of Platinum Nanocrystals

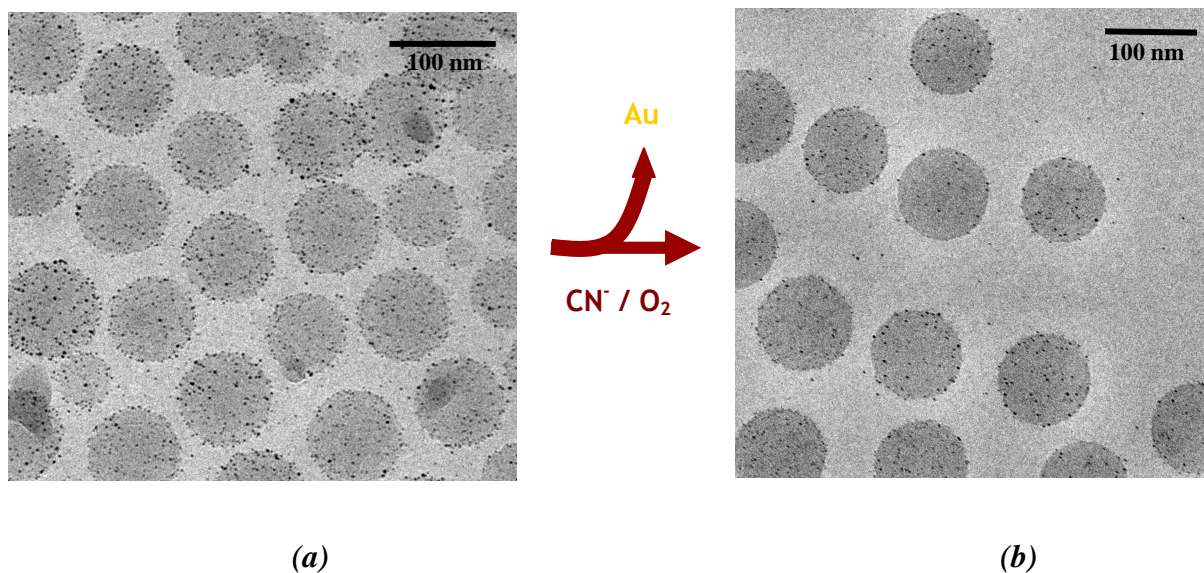
Metallic nanoparticles of controlled size and shape have recently attracted great interest for a number of possible applications in electronic or optical materials as well as in catalysis.<sup>[7-9]</sup> Starting with the binary Au-Pt nanoalloys from Chapter 2.4 it is possible to generate Pt nanocrystals (Fig. 2.12). The gold atoms of the binary nanoalloy can be selectively complexed by  $\text{CN}^-$ -ions and  $\text{O}_2$ <sup>[3]</sup>, resulting in faceted platinum nanocrystals. The method of complexation was already presented and used in Chapter 2.3.



**Figure 2.12:** Scheme of synthesis of platinum nanocrystals by de-alloying of a Au-Pt-nanoalloy. The carrier particles are SPB that consist of PS core ( $R_H = 50$  nm) onto which cationic polyelectrolyte chains of 2-AEMH are chemically attached. In a first step the  $\text{Cl}^-$  counter-ions are exchanged against  $\text{AuCl}_4^-$ -ions; in a second step the remaining of  $\text{Cl}^-$ -ions are exchanged against  $\text{PtCl}_6^{2-}$ -ions. Bimetallic  $\text{Au}_{45}\text{Pt}_{55}$  nanoalloy particles are generated by reduction of the mixture of these ions by  $\text{NaBH}_4$ . The composition of the resulting nanoalloy can be adjusted very well by the ratio of the metal ions in the brush layer. In the final step  $\text{CN}^-$ -ions and  $\text{O}_2$  are used to leach out the gold atoms from the nanoalloy under very mild conditions. This procedure leads to faceted platinum nanocrystals with a size of few nanometers only. The platinum nanocrystals are firmly embedded in the surface layer of polyelectrolyte chains and the entire composite particles exhibit an excellent colloidal stability.

We find that the de-alloying of the Au-Pt-nanoalloy proceeds surprisingly smoothly. Fig. 2.13 shows micrographs of the composite particles before and

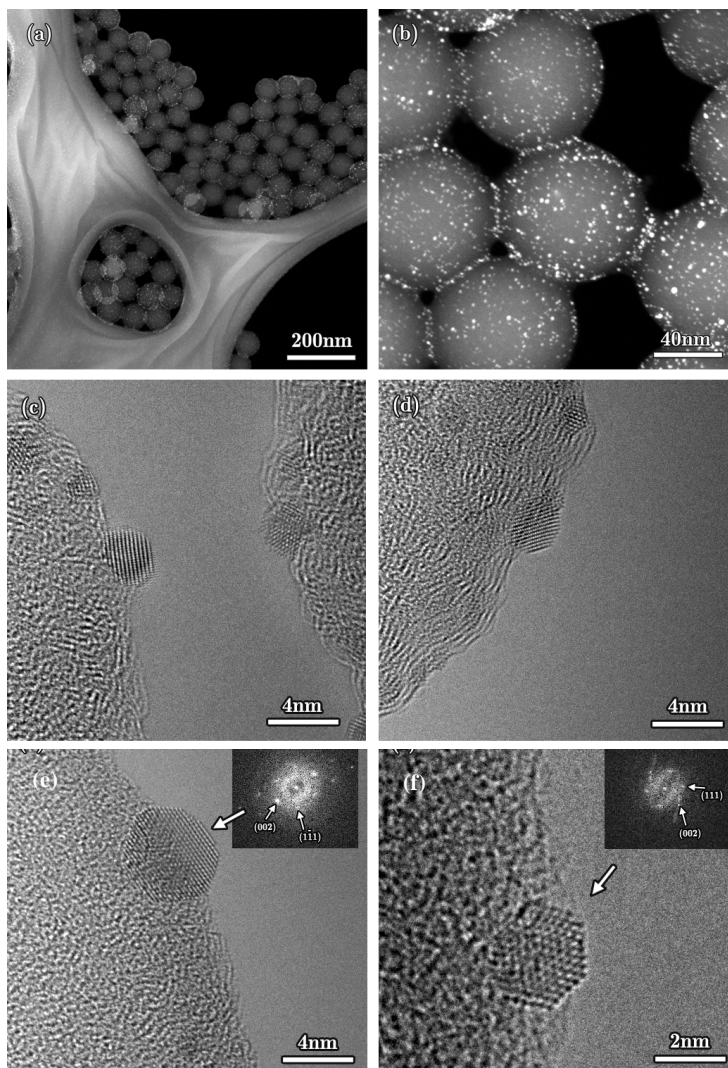
after the leaching process. These micrographs were obtained by cryo-TEM that allows us to analyze the particles in their native state.



**Figure 2.13 (a) und (b):** Cryo-TEM micrographs of the Au-Pt nanoalloy particles (composition:  $\text{Au}_{45}\text{Pt}_{55}$ ) generated on the surface of the spherical polyelectrolyte brushes (a). Composite particles after complete removal of the gold atoms from the Au-Pt nanoalloy by a mixture of  $\text{CN}^-$ -ions and  $\text{O}_2$  (b).

The formation of the cyanide complex of gold atoms is very selective. Hence, only gold atoms of bimetallic Au-Pt nanoalloy are leached out. Energy dispersive X-ray spectroscopy (EDX) demonstrates, indeed, that the metal nanoparticles resulting from de-alloying of nanoparticles consist only of platinum. There can't be detected any traces of gold. The structure of the resulting platinum nanoparticles was analyzed by combining high angle annular dark field scanning transmission electron microscopy (HAADF-STEM) and HR-TEM. Fig. 2.14 (a) shows a low-magnification HAADF-STEM micrograph of the polystyrene spheres on the supporting holey carbon film. Fig. 2.14 (b) is a higher magnification of the same area which shows the uniform distribution of the PtNP on the PS spheres. In order to avoid any disturbance of this analysis by the core particles only nanoparticles sitting on the periphery of the carrier spheres were analyzed by HR-TEM (see Fig. 2.14 (c) – 2.14 (f)). HR-TEM demonstrates that the platinum nanoparticles really are single crystals. All platinum particles observed were

crystalline and no grain boundaries were observed inside the particles. In several cases the facets can be indexed because the nanocrystals are aligned by chance. For instance, in Figures 2.14 (e) and 2.14 (f), the electron diffraction shows directly the hexagonal symmetry of the cubic crystal.



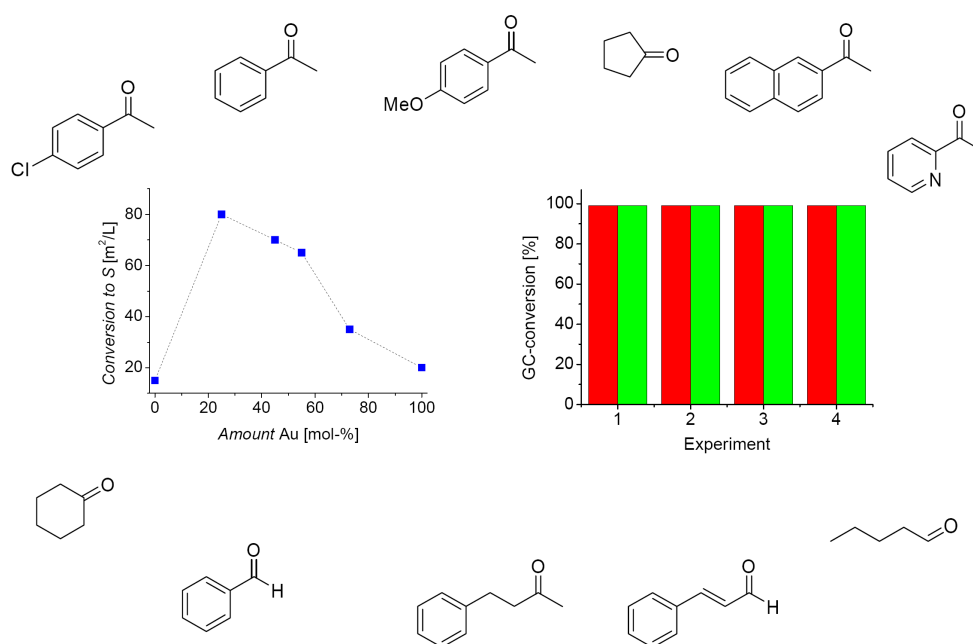
**Figure 2.14 (a) – (f):** HAADF-STEM micrographs of the platinum nanoparticles (bright spots) embedded and uniformly dispersed on a surface layer of the spherical polyelectrolyte (a) and (b); HR-TEM micrograph of nanoparticles on the surface of two adjacent spherical polyelectrolyte (c); HR-TEM micrograph of several crystalline nanoparticles (d); HR-TEM micrographs of two different single crystalline platinum nanoparticles of sizes 4.6 nm and 2.8 nm, respectively, showing well defined facets (e) – (f). All micrographs were acquired at 300 keV.

A detailed description of all experiments and results for faceted Pt nanocrystals can be found in Chapter 3.5.

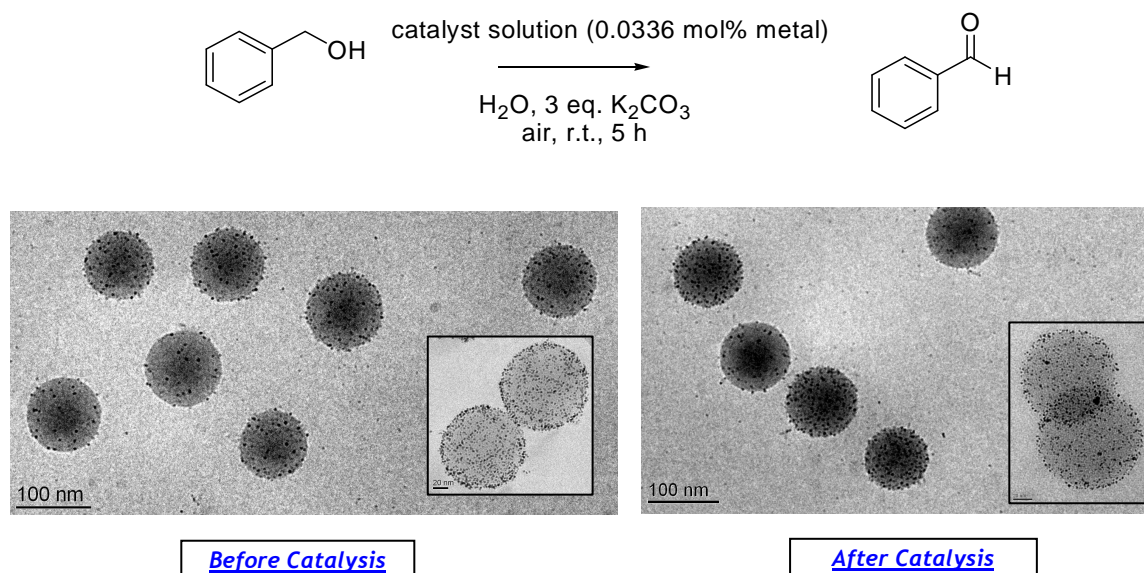
## 2.6 Application of Metal Nanoparticles in Catalysis

Some works show the special catalytic properties of binary gold nanoalloys.<sup>[10]</sup> Au-Pd<sup>[11]</sup> and Au-Pt<sup>[12]</sup> have higher catalytic activities in comparison to respective monometals.

Industrial interesting molecules especially aromatic aldehydes and ketones.<sup>[13]</sup> It is possible to synthesize those primary and secondary alcohols by using a catalyst. Important parameters are the conditions of the reaction and the stability of the catalyst. We were successful in the synthesis of the aldehydes and ketones at room temperature and air by using the described Au-Pt nanoalloys above (Fig. 2.15). The catalytic activity for the oxidation of alcohols to the respective aldehydes goes through a maximum as the function of the Au/Pt composition. The highest conversion was succeeded with the nanoalloy of composition Au<sub>20</sub>Pt<sub>80</sub>. The catalysts could be used for different reaction cycles. It should be noted that no surface stabilization was needed to keep these particles from coagulation. The stabilization is solely achieved by the SPB on which the alloy nanoparticles are immobilized and the catalysis shows a very high selectivity towards aldehydes owing to the mild reaction conditions. The examination of the particle morphologies before and after catalysis is needed to do in situ. As seen in Figure 2.16 the cryo-TEM images show that there is no change in the morphology before and after the catalysis of the oxidation of benzyl alcohol. Another interesting reaction is the epoxidation of unsaturated molecules (Fig. 2.17). It was shown that there is a high conversion and activity for binary nanoalloys such as Au-Pt, Au-Ru, Au-Rh and Au-Ir.

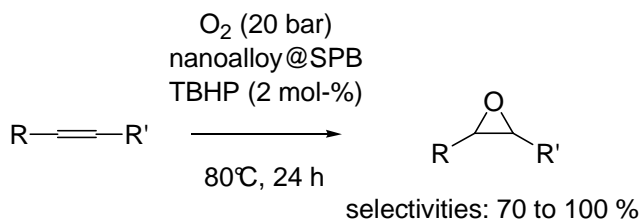


**Figure 2.15:** Different industrial interesting aldehydes and ketones, synthesized by the conversion of the respective alcohol using Au-Pt nanoalloys from Chapter 2.4 as a catalyst. On the left hand side the dependency of conversion (normalized to the surface area) on the amount of gold in bimetallic nanoparticles is shown. The highest conversion is reached for a composition of 20 % gold and 80 % platinum. On the right hand side the results from the reusing experiments of the catalyst solution is shown. The catalyst didn't lose his activity.



**Figure 2.16:** Cryo-TEM image of Au-Pt@SPB catalyst solution before and after catalyzed conversion of benzyl alcohol to benzaldehyde. The morphology of the particles didn't change.





**Figure 2.17:** Heterogeneous epoxidation of alkenes using nanoalloys@SPB as efficient catalysts and  $\text{O}_2$  as oxidant, activated by TBHP.

A detailed description of all experiments and results of the oxidation reactions of binary Au-Pt nanoalloys can be found in chapter 3.4. A detailed description of all experiments and results of the epoxidation reactions of binary Au-Pt, Au-Ru, Au-Rh and Au-Ir nanoalloys as catalysts can be found in Chapter 3.6.

## 2.7 Individual Contribution to Each Publication

In the following part my own contribution to each publication is listed. The corresponding author is marked by \*.

- Chapter 3.1

This publication is published in *Chemical Engineering Journal* **2008**, 144, 138 – 145 under the title ‘**A novel photoreactor for the production of electrosterically stabilised colloidal particles at larger scales**’ by M. Schrunner, B. Haupt, A. Wittemann\*.

My contributions to this work were the synthesis and characterization of the cationic SPB. A. Wittemann was partially involved in the development of the anionic SPB including their characterization. B. Haupt was involved in discussions concerning synthesis of SPB systems.

- Chapter 3.2

This publication is published in *Langmuir* **2007**, 23, 3615 – 3619 under the title ‘**Binding of oppositely charged surfactants to spherical polyelectrolyte brushes: A study by cryogenic transmission electron microscopy**’ by Larysa Samokhina, Marc Schrunner, Matthias Ballauff\*, Markus Drechsler.

My contributions to this work were the synthesis and electron microscopic characterization of the anionic SPB. The considerations and generation of the different mixtures were carried out by myself. M. Drechsler introduced me into the work at the TEM.

- Chapter 3.3

This publication is published in *Macromolecular Chemistry and Physics* **2007**, 208, 1542 – 1547 under the title ‘**Mechanism of the Formation of Amorphous Gold Nanoparticles within Spherical Polyelectrolyte Brushes**’ by Marc Schrunner, Frank Polzer, Yu Mei, Yan Lu, Björn Haupt, Matthias Ballauff\*, Astrid Gödel, Markus Drechsler, Johannes Preussner, Uwe Glatzel.

My contributions to this work were the experiments for synthesis and characterization of all systems. A. Gödel, M. Drechsler and J. Preussner, U. Glatzel were involved in discussions during my work on the TEM.



- **Chapter 3.4**

This publication is published in *Advanced Materials* **2008**, 20, 1928 – 1933 under the title **‘Stable bimetallic Gold-Platinum Nanoparticles Immobilized on Spherical Polyelectrolyte Brushes’** by Marc Schrunner, Sebastian Proch, Yu Mei, Rhett Kempe\*, Nobuyoshi Miyajima, Matthias Ballauff\*.

My contributions to this work were the synthesis and characterization of the nanoalloys and of the gold nanoparticles. The platinum nanoparticles were synthesized by Y. Mei. The examinations about catalytic activity were done in co-operation with S. Proch. The electron microscopy work were carried out together with N. Miyajima.

- **Chapter 3.5**

This publication is published in *Science* 2009, 323, 617 – 620 under the title **‘Single Nanocrystals of Platinum Prepared by Partial Dissolution of Au-Pt-Nanoalloys’** by Marc Schrunner, Matthias Ballauff\*, Yesahahu Talmon, Yaron Kauffmann, Jürgen Thun, Michael Möller, Josef Breu.

My contributions to this work were the synthesis and characterization of the nanoparticles. The electron microscopic work was carried out together with Y. Talmon and Y. Kauffmann during my stay at the TECHNION (Haifa). WAXS was conducted in co-operation with J. Thun and M. Möller.

- **Chapter 3.6**

This publication is to be submitted in **2008** under the title **‘Nanoalloys as efficient “green” catalysts for the epoxidation of alkenes by molecular oxygen’** by Marc Schrunner, Matthias Ballauff\*, Salem Deeb, Sebastian Proch, Rhett Kempe\*, Yaron Kauffmann, Jürgen Thun, Josef Breu.

My contributions to this work were the synthesis and characterization of the nanoparticles. The catalytic application of the particles were carried out together with S. Proch. The electron microscopic work was carried out together with Y. Talmon and Y. Kauffmann during my stay at the TECHNION (Haifa). WAXS was conducted in co-operation with J. Thun and M. Möller.

## 2.8 References

- [1] Guo, X.; Weiss, A.; Ballauff, M. *Macromolecules* **1999**, 32, 6043.
- [2] Ober, C. K.; Wegner, G. *Adv. Mater.* **1997**, 9, 17.
- [3] Holleman, A. F.; Wiberg, E. *Lehrbuch der Anorganischen Chemie*, Walter de Gruyter, Berlin **1995**.
- [4] Lou, J.; Maye, M. M.; Petkov, V.; Kariuki, N. N.; Wang, L.; Njoki, P.; Mott, D.; Lin, Y.; Zhong, C.-J. *Chem. Mater.* **2005**, 17, 3086.
- [5] Mott, D.; Luo, J.; Smith, A.; Njoki, P. N.; Wang, L.; Zhong, C.-J. *Nanoscale Res. Lett.* **2007**, 2, 12.
- [6] Bond, G. C. *Platinum Met. Rev.* **2007**, 51(2), 63.
- [7] Jin, R.; Cao, Y. W.; Mirkin, C. A.; Kelly, K. L.; Schatz, G. C.; Zheng, J. G. *Science* **2001**, 294, 1901.
- [8] Burda, C.; Chen, X.; Narayanan, El-Sayed, M. A. *Chem. Rev.* **2005**, 105, 1025.
- [9] Tian, N.; Zhou, Z.-Y.; Sun, S.-G.; Ding, Y.; Wang, Z. L. *Science* **2007**, 316, 732.
- [10] Mallat, T.; Baiker, A. *Chem. Rev.* **2004**, 104, 3037.
- [11] Enache, D. I.; Edwards, J.; Landon, P.; Solsona-Espriu, B.; Carley, A. F.; Herzing, A. A.; Watanabe, M.; Kiely, C. J.; Knight, D. W.; Hutchings, G. J. *Science* **2006**, 311, 362.
- [12] Stamenkovic, V. R.; Mun, B. S.; Arenz, M.; Mayrhofer, K. J. J.; Lucas, C. A.; Wang, G.; Ross, P. N.; Markovic, N. M. *Nater. Mater.* **2007**, 6, 241.
- [13] Tsunoyama, H.; Sakurai, H.; Negishi, Y.; Tsukuda, T. *J. Am. Chem. Soc* **2005**, 127, 9374.

## 3 Publications of this Thesis

### 3.1 A Novel Photoreactor for the Production of Electrosterically Stabilised Colloidal Particles at Larger Scales

*Marc Schrinner<sup>a</sup>, Björn Haupt<sup>a</sup>, Alexander Wittemann<sup>\*a</sup>*

<sup>a</sup> Physikalische Chemie I, University of Bayreuth, 95440 Bayreuth, Germany

Published in *Chemical Engineering Journal* 2008, 144, 138 – 145.

Author's personal copy

Chemical Engineering Journal 144 (2008) 138–145



Contents lists available at ScienceDirect

Chemical Engineering Journal

journal homepage: [www.elsevier.com/locate/cej](http://www.elsevier.com/locate/cej)

## A novel photoreactor for the production of electrosterically stabilised colloidal particles at larger scales

Marc Schrunner, Björn Haupt, Alexander Wittemann\*

Physikalische Chemie I, University of Bayreuth, Universitätsstr. 30, D-95440 Bayreuth, Germany

### ARTICLE INFO

#### Article history:

Received 28 April 2008

Received in revised form 23 June 2008

Accepted 3 July 2008

#### Keywords:

Colloidal particles

Polyelectrolyte brush

Polymer latex

Emulsion polymerization

Photopolymerization

Electrosteric stabilization

Suspension

Grafting from

### ABSTRACT

A novel photoreactor to facilitate electrosteric stabilization of colloidal polymer particles is presented. Anionic and cationic polystyrene particles having a diameter of ca. 100 nm and bearing a thin layer of photoinitiator are used as seed colloids. Anionic and cationic chains of weak or strong polyelectrolytes are grafted onto the surface of these particles. The polyelectrolyte chains are densely tethered onto the surface of the polymer particles. For this purpose, a commercial photoreactor setup developed for water and liquid waste treatment has been adapted. Compared to the photoreactor used earlier for photoemulsion polymerization, the new reactor largely shortens the reaction times and improves the reproducibility of the reaction. This is achieved by the higher UV power and controlled radiation times and power.

© 2008 Elsevier B.V. All rights reserved.

### 1. Introduction

Colloidal suspensions have found an almost unlimited broad range of technical applications in paper, leather, textile and construction industry but also in medicine and pharmacy [1]. Amongst others, they serve as coatings, inks, paints, lubricants, adhesives and foams [1]. The modification of the surface of colloidal particles is of wide interest to provide specific interactions among the particles or towards the external environment. In particular, the large interfacial area of colloidal particles requires sufficient stabilization to prevent phase separation and coagulation [2].

Stable colloidal suspensions can be achieved by incorporating ionic groups onto the particles or adsorbing surfactant molecules [3]. However, electrostatic stabilization is only operative at low ionic strength. A second kind of stabilization is achieved by either adsorbing or grafting polymer chains onto the surface of colloidal particles [4–6]. Non-ionic steric stabilization allows stabilization at high concentrations of added salt, which is required in many technical applications [1]. Combining both, electrostatic and steric stabilization, is a very effective way to stabilize colloidal suspensions [7,8]. The so-called electrosteric stabilization is provided

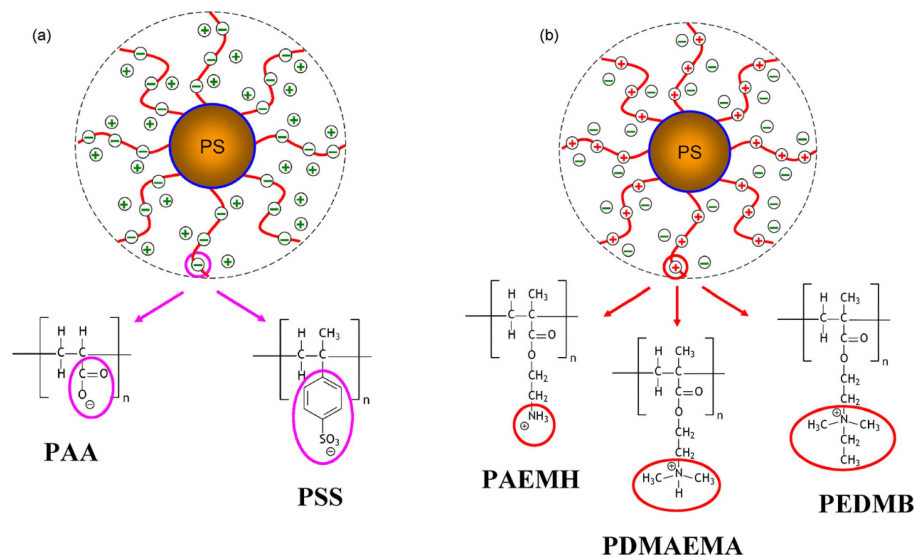
by dense polyelectrolyte brushes grafted onto the surface of the colloidal particles [9–11].

Polyelectrolyte brushes can be created by physisorption of polyelectrolytes or copolymers bearing one polyelectrolyte block onto the surface [12–14]. A stronger attachment to the surface is provided by chemically grafted polyelectrolytes [15]. Two techniques have been applied to synthesize surface grafted polymer brushes: preformed polymers of a desired end functionality are reacted with functional groups on the surface [10]. Due to the steric hindrance among the preformed polymers, a limited grafting density is attained by this “grafted to” method. This is avoided by surfaces bearing initiator functionalities, which are suitable for the brush synthesis from the surface [10]. Biesalski and Rühe used this “grafting from” method to synthesize polyacid brushes on planar surfaces [16]. Ballauff and coworkers prepared spherical polyelectrolyte brushes (SPB) consisting of either weak or strong polyelectrolytes onto the surface of polymer particles by free radical polymerization (Fig. 1) [17–19]. This technique is termed photoemulsion polymerization. It has been shown that these colloidal particles stabilised by polyelectrolyte brushes are stable even at high amounts of added salt and over a wide pH range [20,21]. Moreover, the SPB have already found various possible technological applications as carrier for proteins [22–24], catalytically active metal nanoparticles [18,25] and retention agents [26] for papermaking.

This wide range of applications created a high demand for SPB to further explore the properties of the material. Thus, we were

\* Corresponding author. Tel.: +49 921 55 2776; fax: +49 921 55 2780.

E-mail address: [Alexander.Wittemann@uni-bayreuth.de](mailto:Alexander.Wittemann@uni-bayreuth.de) (A. Wittemann).



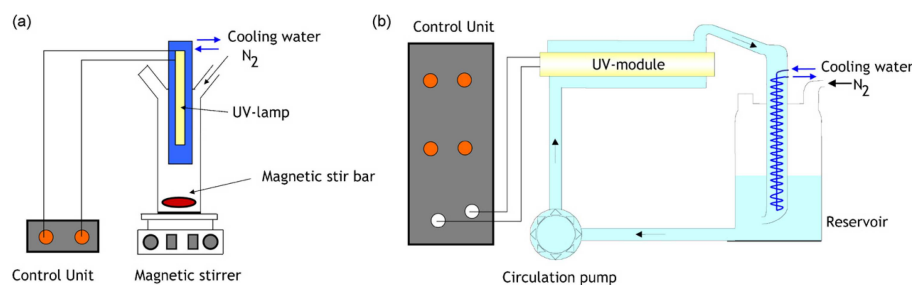
**Fig. 1.** The SPB consist of solid polystyrene particles of ca. 100 nm diameter bearing a dense layer of tethered anionic (a) or cationic polyelectrolytes (b). If chains of weak polyelectrolytes such as PAA and PAEMH are attached, the degree of charges of the SPB depends strongly on the pH, and as a consequence the electrostatic stabilization of the particles is influenced by the external pH. However, if chains of the strong polyelectrolytes PSS and PEDMB are bound, the amount of charges onto the SPB does not depend on the pH.

looking for a technique, which facilitates the process of photoemulsion polymerization. We assigned the reaction described in Ref. [17] to a commercial UV reactor system (aqua concept Laboclean LC Forschungsreaktor, Karlsruhe, Germany), which has been designed for water and liquid waste treatment, i.e., applications, that involve large throughputs or poor transmission (Fig. 2b). After adaptation to the present purpose, this novel reactor largely improves the efficiency of the photoemulsion polymerization by reduced reaction times, larger scales and reproducible reaction conditions. A detailed study on the formation of polyelectrolyte brushes onto model latexes using the novel UV reactor is presented.

## 2. Experimental

### 2.1. Materials

Purification of styrene (BASF, Ludwigshafen, Germany) was accomplished by washing with 10 wt% NaOH solution to remove the inhibitor followed by distillation under reduced pressure. Acrylic acid (AA, Sigma-Aldrich, Buchs, Switzerland) was distilled under reduced pressure to remove the inhibitor. Sodium styrene sulfonate (NaSS), *N,N*-dimethylaminoethyl methacrylate (DMAEMA), potassium persulfate (KPS), sodium dodecylsul-



**Fig. 2.** Photoreactor systems used to conduct photoemulsion polymerization; the schematic representation on the left shows the reactor used by Guo et al. [17]. A medium pressure mercury lamp (TQ 150 Z3, Heraeus Noblelight, Hanau, Germany; range of wave lengths 200–600 nm, power consumption 150 W) surrounded by a cooling quartz tube was directly placed in a 650 ml reactor glass vessel. The right-hand illustration gives a schematic rendition of the UV reactor (aqua concept Laboclean LC Forschungsreaktor, Karlsruhe, Germany) used in the present study. The suspension circulates continuously from a reservoir (here: 3000 ml) into a UV radiation chamber (power consumption reduced to 500 W) and via a condenser back into the reservoir. This setup allows for variable batch sizes that only depend on the size of the reservoir. Continuous circulation of the suspension allows for a highly turbulent flow and prevents the formation of deposits. Moreover, the electronic performance of the UV module enables a repetitious accuracy of the UV irradiation.

## Author's personal copy

140

M. Schrinner et al. / Chemical Engineering Journal 144 (2008) 138–145

fate (SDS), cetyltrimethylammonium bromide (CTAB),  $\alpha,\alpha'$ -azodiisobutyramidine dihydrochloride (V-50) and methacrylic acid hydrochloride were purchased from Sigma–Aldrich (Buchs, Switzerland) in analytical grade and used without further purification. 2-Aminoethylmethacrylate hydrochloride (AEMH) was obtained from Polysciences (Heidelberg, Germany) and Irgacure 2959 was provided by courtesy of Ciba Specialty Chemicals (Lampertheim, Germany). Deionized water obtained from a reverse osmosis water purification system (Academic A10, Millipore, Schwalbach, Germany) was used throughout the entire studies. All other chemicals and solvents were of analytical grade and were used as received.

#### 2.2. Synthesis of HMEM and EDMB

The photoinitiator (HMEM) was prepared by a Schotten–Baumann reaction of Irgacure 2959 and methacrylic acid hydrochloride as described in Ref. [17]. Purification was achieved by column chromatography on silica gel. The purity of the product was verified through NMR spectroscopy (AC 250, Bruker, Karlsruhe, Germany). *N*-Ethyl-*N,N*-dimethylaminoethyl methacrylate bromide (EDMB) serving as monomer in the synthesis of the cationic brushes was prepared, purified and characterized as described in Ref. [27].

#### 2.3. Synthesis of the PS core

The synthesis of anionic and cationic PS latex particles bearing a thin layer of photoinitiator was accomplished by emulsion polymerization using a 3 L double-jacket glass reactor (Büchi Glass, Uster, Switzerland) which was heated through a thermostat (R400 Lauda, Lauda-Königshofen, Germany). In a typical synthesis batch of anionic PS particles, 521 g of freshly distilled styrene was added to a solution of 7.28 g of SDS in 2.17 L of water. The mixture was deoxygenated by several vacuum/nitrogen purge cycles and brought gradually to 80 °C under N<sub>2</sub> atmosphere and continuous stirring (320 rpm). The polymerization was initiated by addition of 2.04 g KPS dissolved in 50 mL of water. After 1 h, the turbid suspension was cooled to 70 °C. A solution of 29.16 g HMEM dissolved in 22.4 mL of acetone was added dropwise (0.2 mL/min) to the suspension and the reaction was continued for a further 5 h.

The preparation of the cationic PS particles was performed along the same lines. Briefly, 208 g of styrene were added to a solution of 2.65 g CTAB in 846 mL of water. After several vacuum/nitrogen purge cycles the reaction mixture was heated to 80 °C. Twenty minutes after addition of the initiator (0.87 g V-50 dissolved in 100 mL of water) the suspension was cooled to 70 °C and 11.6 g of HMEM dissolved in 12.2 mL acetone were added (0.2 mL/min). The reaction was carried out under nitrogen atmosphere and continuous stirring (300 rpm) for 6 h.

All PS-co-HMEM latexes were filtrated through glass wool and purified by exhaustive ultrafiltration (cellulose nitrate membrane, pore diameter 50 nm, Schleicher & Schuell, Dassel, Germany) against water prior to the grafting of the brushes.

#### 2.4. Grafting of the polyelectrolyte brushes

The photopolymerization was carried out in a high-performance UV reactor setup (aqua concept Laboclean LC Forschungsreaktor, Karlsruhe, Germany) consisting of a UV radiation chamber, circulation pump and a 3000 mL reservoir with condenser (Fig. 2b). The spectrum of the light emitted by the Hg medium pressure lamp comprises a number of wavelengths in the range of 200–600 nm. The emission in the UV range between 200 and 300 nm is reinforced. The broadband spectrum the lamp offers makes the device

suitable for many applications such as disinfection, curing of paints and lacquers and other photochemical tasks. Here this setup is used for the buildup of polyelectrolyte brushes on the surface of PS latexes. Briefly, 50 g PS-co-HMEM particles suspended in 2 L of water were placed into the reservoir. External cooling by water recirculation (UWK 140/TP2, Thermo Haake, Karlsruhe, Germany) kept the temperature of the suspension below 32 °C. The desired amount of water-soluble monomer (AA, NaSS, AEMH or EDMB) was added and the reaction mixture was deoxygenated by several vacuum/nitrogen purge cycles. Every 5 min, minute amounts of the suspensions were taken to study the increase in brush thickness during the 30 min of UV irradiation.

#### 2.5. UV power of the photoreactor

The UV power of the Hg medium pressure lamp was determined every 10 operating hours. The rate of the UV-induced decomposition of hydrogen peroxide was used as a measure for the UV power. Briefly, 3000 mL of 0.2 M hydrogen peroxide solution were irradiated for 15 min under permanent external cooling at 8 °C. In regular intervals minute samples were taken. The concentration of hydrogen peroxide in the samples was determined by cerimetric titration with 0.002 M Ce(IV) solution and ferroin as indicator. The rate of the decomposition of hydrogen peroxide normalized to the output power of the lamp of 500 W was in the range of 2.1 mol H<sub>2</sub>O<sub>2</sub> per kWh.

#### 2.6. Methods

Cryogenic transmission electron microscopy (cryo-TEM) specimens were prepared by vitrification of thin liquid films of the suspensions supported by a copper grid (600 mesh, Science Services, Munich, Germany) in liquid ethane. The specimen was inserted into a cryo-transfer holder (CT3500, Gatan, Munich, Germany) and transferred to a Zeiss EM922 EFTEM (Zeiss NTS GmbH, Oberkochen, Germany) operating at an accelerating voltage of 200 kV. Images were recorded digitally by a CCD camera (UltraScan 1000, Gatan) and processed with a digital imaging system (Digital Micrograph 3.9, Gatan). More detailed information can be found in Ref. [19].

The distributions of the core particle sizes were recorded on a disc centrifuge (BI-DCP, Brookhaven Instruments Corporation, Holtsville, USA) and by transmission electron microscopy (TEM, H7, Hitachi High-Technologies, Krefeld, Germany). Dynamic light scattering (DLS) measurements were performed on an ALV-4000 (ALV, Langen, Germany) light scattering goniometer equipped with a He–Ne laser (uniphase 1145P-3083, Manteca, USA) which provides a wavelength of 632.8 nm, and an ALV-5000 multiple tau digital correlator (ALV). Hydrodynamic radii were obtained by a cumulant analysis [28] from the correlation functions.

Conductometric titration (Cond 197i, WTW, Weilheim, Germany) was employed to determine the total mass of polymer that has been attached to the polystyrene particles during photoemulsion polymerization (see Table 1). This method was based on the change in the electric conductance during acid–base titration or precipitation of hardly soluble silver salts. Minute amounts of the suspension were purified by exhaustive ultrafiltration against water. The carboxylic groups of the PAA brushes were titrated against standard solutions of sodium hydroxide. The amount of cationic polymers was determined by titration of the bromine or chloride counterions against a standard solution of 0.1 M AgNO<sub>3</sub>. The results were verified by elementary analysis (Vario EL III, elementar Analysengeräte, Hanau, Germany). The amount of PSS chains was quantified gravimetrically. To that end, the amount of solid present in the suspension was determined before and

**Table 1**  
Parameters of the model latexes used in the present study

SPB	$R^a$	$L_c^b$	$L_{water}^c$	$M_n^d$	$M_w^e$	PDI <sup>f</sup>	$m_{PS}/m_{PEL}^g$	$\sigma$ (nm <sup>-2</sup> ) <sup>h</sup>
PAA1	50	–	75	–	–	–	12.7	–
PAA2	50	79	75	13,600	30,000	2.2	8.1	0.13
PAA3	50	51	62	11,300	20,000	1.7	9.4	0.13
PAA4	50	–	112	–	–	–	9.2	–
PAA5	56	–	17	–	–	–	12.0	–
PSS1	56	–	65	–	–	–	2.7	–
PSS2	56	–	120	–	–	–	2.1	–
PAEMH1	45	68	54	16,000	31,000	1.9	8.5	0.11
PDMAEMA1	45	89	85	12,700	25,000	2.0	11.3	0.14
PEDMB1	45	75	68	15,000	35,000	2.3	9.7	0.13

The nomenclature of the SPB refers to the type of tethered polyelectrolytes (PAA1–5: poly(acrylic acid); PSS1–2: poly(styrene sulfonate); PAEMH1: poly(2-aminoethylmethacrylate hydrochloride); PDMAEMA1: poly(*N,N*-dimethylaminoethyl methacrylate); PEDMB1: poly(*N*-ethyl-*N,N*-dimethylaminoethyl methacrylate bromide)).

<sup>a</sup> Radius of the PS core.

<sup>b</sup> Contour length of the grafted polyelectrolyte chains.

<sup>c</sup> Brush thickness in water.

<sup>d</sup> Number-average molecular weight.

<sup>e</sup> Weight-average molecular weight of the polyelectrolyte chains.

<sup>f</sup> Polydispersity index ( $M_w/M_n$ ).

<sup>g</sup> Mass composition  $m_{PS}/m_{PEL}$  of the SPB where  $m_{PS}$  and  $m_{PEL}$  are the masses of the PS core and polyelectrolyte shell, respectively.

<sup>h</sup> Grafting density (number of chains per core surface).

after exhaustive ultrafiltration against water. The loss of solid during purification gives the amount of free PSS chains or unreacted monomers. Hence, the mass of tethered PSS chains is obtained as the difference between the mass of added NaSS and the mass of the removed solid.

To determine the molecular weight of the tethered chains, the grafted chains were cleaved off from the polystyrene particles. The anchoring groups of the attached polyelectrolyte chains contain an ester bond which stems from the former photoinitiator (Fig. 3). These ester bonds were hydrolysed in the presence of strong aqueous bases. To that end, the SPB particles were suspended in 2 M NaOH and kept at 120 °C for 14 days. Such a rather harsh treatment was necessary since negative coions such as the hydroxide ions are expelled from anionic brushes [29]. The latex particles were separated from the cleaved polyelectrolyte chains by filtration through a cellulose nitrate membrane of 50 nm pore size (Schleicher & Schuell) after neutralisation with hydrochloric acid. The removal of the large amount of added salt was accomplished by exhaustive ultrafiltration (regenerated cellulose membrane, MWCO 5000, Millipore) against deionized water. The completeness of the purification was monitored through the conductance of the filtrate. The purified polyelectrolyte chains were freeze-dried and analyzed using a Viscotek (Weingarten, Germany) triple-detection size-exclusion chromatography (SEC) system.

### 3. Results and discussion

The objective of the present study is to demonstrate the suitability of a novel UV reactor for photoemulsion polymerization. The reaction itself was carried out along the lines given in Ref. [17]. Fig. 3 gives a schematic view on the individual stages of the synthesis of latex particles bearing densely packed polyelectrolyte brushes. Briefly, a narrow-dispersed PS latex is prepared by emulsion polymerization [30]. In the stage of particle growth a copolymerizable photoinitiator is added to the PS seed particles under starved conditions [20]. Here HMEM was used as a model photoinitiator. Other photoinitiators that are polymerizable could be used as well [31]. HMEM is a vinyl monomer (Fig. 3) itself, but it is less hydrophobic than styrene. Thus, a thin shell of photoinitiator is formed onto the surface of the latex particles as the result of the copolymerization of styrene and the polymerizable photoinitiator. In the final step a

water-soluble monomer is added and the suspension is irradiated by UV light. Radicals formed on the surface of the latex particles initiate the polymerization of the water-soluble monomer which results in polymer brushes covalently attached to the latex particles (Fig. 3). One would expect that the strong turbidity of the PS latex might present a severe limitation for a photoreaction. However, the turbidity is even essential for the photopolymerization. This was explained by multiple elastic scattering of the UV light within the suspension which allows the photoreaction to take place [20].

The decomposition of the photoinitiator moieties on the surface of the latex particles gives not only rise to surface-bound radicals but also to free radicals in solution (Fig. 3). The free polymer chains in solution thus obtained are removed from the suspension by ultrafiltration against water. This is necessary to obtain a well-defined model system for the studies described below.

#### 3.1. Preparation of PS particles bearing photoinitiator moieties

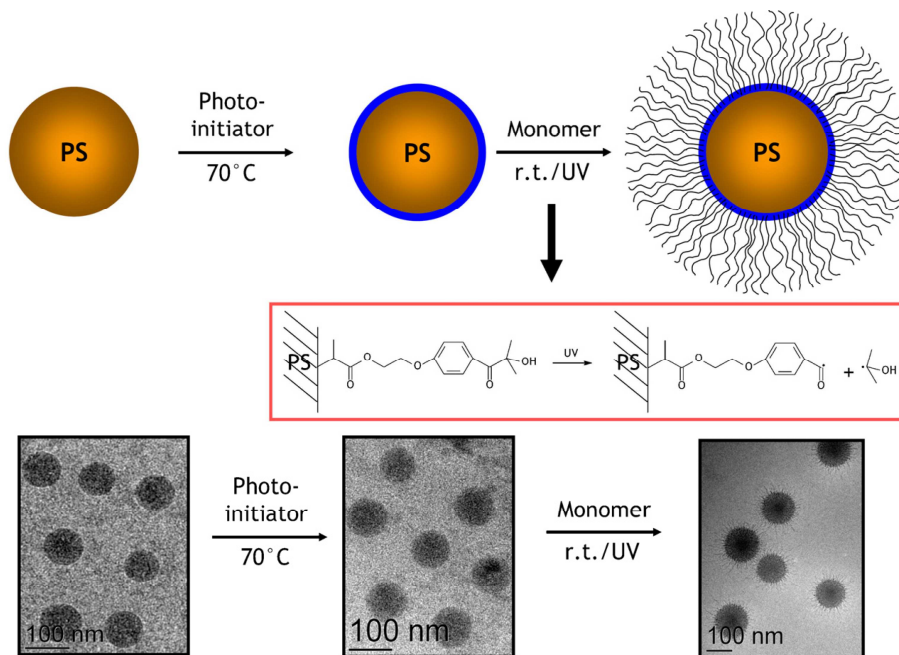
Both anionic and cationic polyelectrolyte brushes should be attached onto PS latex particles to probe the versatility of the photoemulsion polymerization as a tool to stabilize latex particles (Fig. 1). Thus, the PS particles that serve as carrier for the brushes and the monomer used to form the tethered chains must be like-charged. Otherwise electrostatic interactions among the PS particles and the growing polyelectrolyte chains would result in coagulation of the suspension. Thus, anionic and cationic PS latexes were synthesized following the procedure described above. The amounts of surfactant and initiator were chosen to obtain particles with diameters near 100 nm. The ionic nature of the initiator (KPS or V-50) leads to ionic groups on the surface of the PS particles which give the particles sufficient electrostatic stability prior to the grafting of the polyelectrolyte layer. The emulsion polymerization is carried out in a batch process at 80 °C until most of the styrene has reacted. Then the copolymerizable photoinitiator HMEM was added under starved conditions at 70 °C. At this stage of the reaction the PS particles are still swollen with styrene. Copolymerization of styrene and HMEM yielded a thin solid layer of photoinitiator onto the latex particles. Morphological studies by small angle X-ray scattering (SAXS) indicated that the thickness of the photoinitiator layer is in the order of two nanometers [15]. Thus, a well-defined thin



Author's personal copy

142

M. Schurriner et al. / Chemical Engineering Journal 144 (2008) 138–145



**Fig. 3.** Preparation of latex particles stabilised with long polyelectrolyte chains: at first polystyrene spheres were prepared by emulsion polymerization. The PS particles were coated with a thin layer of a polymerizable photoinitiator at a given conversion of styrene. The seed particles were extensively purified by ultrafiltration against water. Water-soluble monomers such as acrylic acid or styrene sulfonate were added. UV irradiation of the suspension led to surface-bound radicals and free radicals in solution. Both types of radicals initiated the polymerization of the water-soluble monomer. Hence, both polyelectrolyte chains anchored onto the PS seed particles and free chains in solution were obtained. The free chains in solution were removed by exhaustive ultrafiltration. Cryo-TEM micrographs demonstrate that well-defined core-shell particles can be made by this technique.

photoinitiator layer was obtained by this procedure. The size distribution of the PS particles was determined using an analytical disc centrifuge. The average diameter of the particles was in the order of 100 nm (Table 1). The polydispersity in particle size expressed as the weight-average diameter divided through the number-average diameter was less than 1.02. Since the PS particles are quite uniform in size, they are suitable seed particles for the built-up of well-defined core-shell particles during the photoreaction.

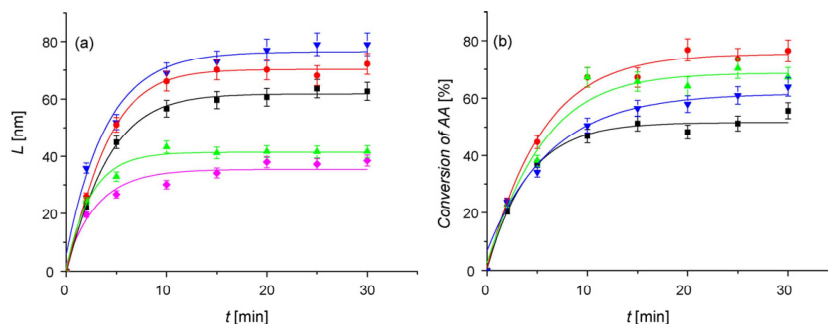
### 3.2. Synthesis of the spherical polyelectrolyte brushes: photoemulsion polymerization

The UV lamp of the photoreactor used in Ref. [17] was directly immersed into the suspension (Fig. 2a). Thus the volume was fixed by the size of the reaction vessel (650 mL) circumventing the UV module. In the present setup the reaction mixture circulates continuously from the reservoir into the UV radiation chamber and via a condenser back into the reservoir (Fig. 2b). The circulation of the suspension guarantees a highly turbulent flow and prevents the formation of deposits in the reactor. The electronic performance of the UV module allows for repetitious accuracy of the irradiation time and power. At regular intervals the power of the UV lamp was determined through the UV-induced decomposition of hydrogen peroxide. To ensure comparable reaction conditions the anionic and cationic brushes were prepared under similar UV powers of ca. 2.1 mol of decomposed  $\text{H}_2\text{O}_2$  per kWh.

The PS-co-HMEM latex particles were used as seeds to conduct polymerization in the suspension of the particles comprising a water-soluble monomer. The content of seed particles was fixed to 2.5 wt%. The highest concentration of monomer used in the experiments was 0.15 M. These concentration limits helped to prevent the recombination of growing polyelectrolyte chains attached to different latex particles and thus the formation of a network of crosslinked particles. The formation of individual particles of well-defined core-shell morphology under these premises becomes evident in the cryo-TEM images (Fig. 3).

Minute samples of the suspensions were taken during the photoemulsion polymerization to study the formation of the polyelectrolyte brushes onto the latex particles. DLS is well suited to study the thickness of SPB [20]. The hydrodynamic thickness of the brush layer is obtained by subtraction of the hydrodynamic radius of the SPB at a given reaction time from the radius of the seed particles. Fig. 4a contains data for the built-up of PAA brushes. The formation of the brush layer starts right after the UV radiation is started. A rapid increase of the brush thickness is obtained during the first minutes of irradiation. The reaction is completed after only 20 min of polymerization, i.e., maxima of the brush thickness and of the monomer conversion are attained. However, 240 min were necessary to come at the same stage of the polymerization with the setup used by Guo et al. (cf. Fig. 2 of Ref. [17]). Hence, the new reactor largely shortens the reaction times, which is mainly achieved by the increase of the UV power from 150 to 500 W.

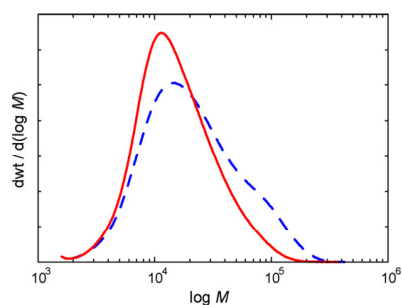




**Fig. 4.** (a) Hydrodynamic thickness  $L$  of brushes composed of PAA as the function of the reaction time  $t$ . Parameter is the amount of photoinitiator used in the synthesis of the PS-co-HMEM seed (squares: PAA1 0.5 mol% HMEM; down triangles: PAA4 1.0 mol% HMEM; up triangles: PAA3 2.0 mol% HMEM; circles: PAA2 4.0 mol% HMEM in respect of the content of styrene units of the core particles). The amount of acrylic acid was the same (40 mol% in regard to the content of styrene units of the core). Latex PAA5 (diamonds) was prepared using the same PS-co-HMEM seed as for PAA2. The lower brush thickness results from the lower amount of acrylic acid added (25 mol%). (b) Conversion of acrylic acid during the photoemulsion polymerization. An increasing amount of HMEM leads to a higher total conversion of monomer (squares: PAA1 0.5 mol% HMEM; down triangles: PAA4 1.0 mol% HMEM; up triangles: PAA3 2.0 mol% HMEM; circles: PAA2 4.0 mol% HMEM in respect of the content of styrene units of the core particles). Both experiments, namely the increase in particle size measured by DLS and the monomer conversion, clearly indicate that the formation of the brush is completed after a reaction time of 30 min.

The thickness of the brush layer  $L$  is governed by the osmotic pressure of the counterions of the polyelectrolyte chains [20,32]. The absolute number of counterions within the brush increases with the contour length  $L_c$  and grafting density  $\sigma$  of the polyelectrolyte chains. The brush thickness shown in Fig. 4a is governed by two opposing phenomena. In principle, the brush thickness should increase with the content of photoinitiator moieties as higher grafting densities increase the concentration of counterions entrapped within the brush. On the other hand, the monomer-to-initiator ratio decreases as the total amount of monomer is kept constant in all experiments. Moreover, since DLS radii are dominated by the longest chains of the brush, the polydispersity of the tethered chains has an additional impact on the brush height. This is discussed in conjunction with Fig. 5. Thus, an exact interpretation of the brush heights shown in Fig. 4a as the function of photoinitiator moieties and monomer concentration is rather difficult. However, if the photoinitiator content of the seed particles is kept constant, a lower monomer concentration yields a lower brush height as expected (see system PAA2 vs. PAA5 in Fig. 4a).

The total conversion of acrylic acid was determined through the content of solid in the suspension. To this end, the samples



**Fig. 5.** Molecular weight distributions (MWD) of sodium polyacrylate chains cleaved from PAA2 (dashed line) and PAA3 (solid line). The average molecular weights and polydispersity indices are gathered in Table 1. The polydispersities close to 2 are typical for a free radical polymerization.

of the suspension taken during the photoreaction were subdivided into amounts of 2 g. The volatile monomer and water was removed under reduced pressure at 80 °C. The conversion of acrylic acid was obtained as the difference between the total content of solid and the content of added seed particles (2.5 wt%) divided by the initial content of acrylic acid. The percentage of consumed acrylic acid comprises both PAA chains attached to the latex particles and free PAA chains in solution.

The monomer conversion (Fig. 4b) shows the same characteristics as the brush thickness  $L$  with reaction time  $t$  (Fig. 4a). The consumption of acrylic acid proceeds very fast at the earlier stages of the irradiation and a plateau value is attained after 15 min. The plateau consumption increased with the content of photoinitiator of the seed latex. A higher percentage of consumed monomer is also obtained if less monomer is added (not shown). For all five reactions studied the monomer consumption did not exceed 80%. Hence, the reaction is terminated without full consumption of acrylic acid. This does not mean that an excess of monomer was added since a higher brush thickness was obtained at higher monomer concentration (Fig. 4a). In fact, the mechanisms that terminate the growing of the chains on the seed particles should bring about incomplete conversion of monomer. These mechanisms are not known in detail. Such mechanisms might involve recombination with free chain radicals grown in solution or short-chain radicals. The latter ones could be formed by side reactions during photoradiation [31].

Since the photoinitiator is decomposed into surface-bound radicals and free radicals in solution, free polyelectrolyte chains are formed during the photopolymerization. The free chains were removed by exhaustive ultrafiltration against water. This purification step was used to determine the composition of the PSS brushes, i.e., the mass ratio of polystyrene to grafted polyelectrolyte ( $m_{PS}/m_{PEL}$ ). For this purpose the content of solid in the suspension before and after the removal of unbound PSS chains was determined. The difference between the mass of sodium styrene sulfonate added to the seed latex and the mass of free PSS chains is the mass of PSS attached to the latex particles. The relative experimental error of  $m_{PS}/m_{PEL}$  is 5% based on the relative error of the solid content of 0.4% and taking weighing errors and mass losses during synthesis and purification into account.

A different approach was applied for the brushes composed of PAA since the molar mass of acrylic acid is lower than the one of

sodium styrene sulfonate.  $m_{PS}/m_{PEL}$  was determined by conductometric titration of the carboxyl groups. The relative experimental error is 4%. The mass ratio  $m_{PS}/m_{PEL}$  obtained for the PAA and PSS brushes are summarized in Table 1. Between 29 and 52% of the total monomer is consumed to build up the polyelectrolyte brush. This percentage increases with the HMEM content of the seed latex and decreases with the initial monomer concentration. Division of this percentage by the total fraction of monomer consumed during the photoemulsion polymerization gives the ratio of PAA tethered to latex particles to free PAA (Table 1). Depending on the experiment, between 1.1 and 1.8 chains of PAA were grafted to the seed particles with respect to one free chain. One would expect a one-to-one ratio since the photoinitiator is decomposed into two radicals. However, recombination of free chain radicals with tethered chain radicals decreases the amount of free chains.

More specific information on the grafted polyelectrolyte chains is obtained through cleavage of the chains from the latex particles and characterization of the cleaved chains by SEC. We restricted such an analysis to selected samples (Table 1) since a large amount of the suspension is consumed to obtain a reasonable quantity of cleaved polyelectrolyte. The former photoinitiator moieties which serve now as anchor groups of the polyelectrolyte chains bear an ester group (Fig. 3). The hydrolysis was achieved over 15 days in the presence of 2 M NaOH at 120 °C [17]. The cationic chains comprising ester bonds in their monomer units (Fig. 3) were hereby converted into PAA chains. The average molecular weight and the polydispersity of the cleaved polyelectrolyte chains were obtained by SEC (Fig. 5). Polydispersity is defined as the weight-average molecular weight  $M_w$  divided by the number-average molecular weight  $M_n$ . The  $M_w/M_n$  values of the grafted polyelectrolyte chains are in the range of 2, as expected for a radical polymerization (Table 1).

Fig. 5 contains the molecular weight distributions of PAA cleaved from two different SPB. The grafting density  $\sigma$  is the same for both systems. The PAA chains cleaved from PAA3 show a quite narrow-dispersed molecular weight distribution for a radical polymerization. The distribution of the PAA chains of PAA2 exhibits a shoulder at higher molecular weights. This is explained by a recombination of free chain radicals with chain radicals grafted to the latex particles as already discussed above. Since chain termination is brought forth by radicals of low-molecular weight as well, the shoulder at higher molecular weight might be less distinctive in some experiments. The brush thickness was determined by DLS. Since DLS radii are mainly governed by the longest chains of the brush layer [20], PAA2 exhibits a higher brush thickness than PAA3 due to the fraction of PAA chains of higher molecular weight (Fig. 5).

From the number-average molecular weight  $M_n$ , the contour length  $L_c$  is obtained as the product of the number of monomer repeat units and the distance of two C–C bonds of 0.25 nm. The grafting density  $\sigma$  could be calculated as well since the average molecular weight  $M_n$  and the total mass of polyelectrolyte chains per particle expressed in  $m_{PS}/m_{PEL}$  are known. The grafting densities obtained were in the range of 0.13 polyelectrolyte chains per nm<sup>2</sup> surface of the latex particles, i.e., 4000 polyelectrolyte chains were covalently attached per latex particle of 100 nm diameter. The distance between two grafting points is 3 nm. Since the photoemulsion polymerization allows coating latex particles with a densely packed polyelectrolyte layer, dispersions of the resulting particles are electrostatically stabilised in an efficient manner. Much work has been devoted to the stabilizing nature of polyelectrolyte brushes [7,9,32–34]. This effect can be directly measured using a surface force apparatus [35]. The cryo-TEM images demonstrate that the polyelectrolyte chains are strongly stretched (Fig. 3). This is demonstrated in more detail in Ref. [19]. The fact that the tethered chains are strongly stretched together with the thickness of the densely packed layer of several tens of nanometers gives the

particles sufficient stabilization since aggregation among particles would demand a compression of the brush layer.

The novel photoreactor was designed for lab-scale experiments. As mentioned above it allows the fabrication of up to 100 g SPB in just 30 min. This amount could be further increased by using a larger reservoir. Such a quantity should be enough for most experimental studies. Larger UV reactors based on the same principle as the high-performance lab-reactor are commercially available which provide flow rates from 5 up to 1000 m<sup>3</sup>/h (aqua concept, Karlsruhe, Germany). Hence, such reactors would allow the electrostatic stabilization of several tons of particles per day for industrial applications. The production of the precursor latex particles does not present a limiting step for industrial applications since these particles can be made by emulsion polymerization which is a standard technique for the production of such particles [1]. The seed particles with sizes from 50 up to 300 nm can be made from all monomers such as styrene, vinyl acetate, vinyl chloride or acrylates that undergo radical polymerization, and which are hardly soluble in water [1,30]. Moreover, the need for a photoinitiator that is copolymerizable should not present an obstacle as well since such compounds are used in the coating industry for solvent-free lacquers [31]. In the present study, the photoinitiator HMEM was obtained through a one-step chemical modification of such a photoinitiator (Irgacure 2959, Ciba Specialty Chemicals, Lampertheim, Germany). Other copolymerizable photoinitiators that are poorly soluble in water such as benzoin acrylate can be used as well [31]. Hence, the photopolymerization presents a versatile technique since the chemical composition and dimensions of the particles can be adjusted in a wide range.

#### 4. Conclusion

In conclusion, affixing long polyelectrolyte chains to polymer particles by photoemulsion polymerization opens new perspectives for stabilised polymer suspensions. In principle, chains of any water-soluble vinyl monomer can be attached to colloidal particles bearing photoinitiator moieties. Hence, the technique presents a versatile tool to stabilize colloidal particles but also allows specific surface functionalization. The novel photoreactor helps to further explore the potential of this technique since a better control of the photoreaction is achieved, along with shorter irradiation times. Moreover, the flow-through UV module enables large-scale reaction processing. This renders the technique promising for industrial applications that involve stabilised colloids.

#### Acknowledgment

Financial support by the Deutsche Forschungsgemeinschaft within SFB 481 and Roche Diagnostics is gratefully acknowledged.

#### References

- [1] D. Urban, K. Takamura, *Polymer Dispersions and Their Industrial Applications*, Wiley-VCH, Weinheim, 2002.
- [2] J.N. Israelachvili, *Intermolecular and Surface Forces: With Applications to Colloidal and Biological Systems*, Academic Press, Amsterdam, 1985.
- [3] D.F. Evans, H. Wennerström, *The Colloidal Domain Where Physics, Chemistry and Technology Meet*, Wiley VCH, New York, 1999.
- [4] A.M.I. Ali, P. Pareek, L. Sewell, A. Schmid, S. Fujii, S.P. Armes, I.M. Shirley, *Soft Matter* 3 (2007) 1003.
- [5] R. Inoubli, S. Dagreou, M.-H. Delville, A. Lapp, J. Peyrelasse, L. Billon, *Soft Matter* 3 (2007) 1014.
- [6] P. Borget, F. Lafuma, C. Bonnet-Gonnet, *J. Colloid Interf. Sci.* 285 (2005) 136.
- [7] M.N. Tamashiro, E. Hernandez-Zapata, P.A. Schorr, M. Balastre, M. Tirrell, P. Pincus, *J. Chem. Phys.* 115 (2001) 1960.
- [8] G. Fritz, V. Schädler, N. Willenbacher, N.J. Wagner, *Langmuir* 18 (2002) 6381.
- [9] P. Pincus, *Macromolecules* 24 (1991) 2912.
- [10] J. Ruehe, M. Ballauff, M. Biesalski, P. Dziezok, F. Groehn, D. Johannsmann, N. Iloubeinov, N. Ilegenberg, R. Konradi, S. Minko, M. Motornov, R.R. Netz, M.

Author's personal copy

M. Schrunner et al. / Chemical Engineering Journal 144 (2008) 138–145

145

- Schmidt, C. Seidel, M. Stamm, T. Stephan, D. Usov, H. Zhang, *Adv. Polym. Sci.* 165 (2004) 79.
- [11] F. Zhou, W.T.S. Huck, *Phys. Chem. Chem. Phys.* 8 (2006) 3815.
- [12] H. Ahrens, S. Foerster, C.A. Helm, *Macromolecules* 30 (1997) 8447.
- [13] S.W. An, P.N. Thirtle, R.K. Thomas, F.L. Baines, N.C. Billingham, S.P. Armes, J. Penfold, *Macromolecules* 32 (1999) 2731.
- [14] T. Abraham, S. Giasson, J.F. Gohy, R. Jerome, *Langmuir* 16 (2000) 4286.
- [15] M. Ballauff, *Prog. Polym. Sci.* 32 (2007) 1135.
- [16] M. Biesalski, J. Rühe, *Macromolecules* 32 (1999) 2309.
- [17] X. Guo, A. Weiss, M. Ballauff, *Macromolecules* 32 (1999) 6043.
- [18] M. Schrunner, F. Polzer, Y. Mei, Y. Lu, B. Haupt, M. Ballauff, A. Gödel, M. Drechsler, J. Preussner, U. Glatzel, *Macromol. Chem. Phys.* 208 (2007) 1542.
- [19] A. Wittmann, M. Drechsler, Y. Talmon, M. Ballauff, *J. Am. Chem. Soc.* 127 (2005) 9688.
- [20] X. Guo, M. Ballauff, *Langmuir* 16 (2000) 8719.
- [21] X. Guo, M. Ballauff, *Phys. Rev. E* 64 (2001) 051406/1.
- [22] K. Anikin, C. Röcker, A. Wittmann, J. Wiedenmann, M. Ballauff, G.U. Nienhaus, *J. Phys. Chem. B* 109 (2005) 5418.
- [23] A. Wittmann, M. Ballauff, *Phys. Chem. Chem. Phys.* 8 (2006) 5269.
- [24] A. Wittmann, B. Haupt, M. Ballauff, *Phys. Chem. Chem. Phys.* 5 (2003) 1671.
- [25] Y. Lu, Y. Mei, M. Schrunner, M. Ballauff, M.W. Möller, J. Breu, *J. Phys. Chem. C* 111 (2007) 7676.
- [26] Y. Mei, C. Abetz, O. Birkert, V. Schädler, R.J. Leyrer, M. Ballauff, *J. Appl. Polym. Sci.* 102 (2006) 233.
- [27] S.M. Hamid, D.C. Sherrington, *Polymer* 28 (1987) 325.
- [28] B.J. Frisken, *Appl. Opt.* 40 (2001) 4087.
- [29] A. Jusufi, C.N. Likos, H. Löwen, *J. Chem. Phys.* 116 (2002) 11011.
- [30] R.G. Gilbert, *Emulsion Polymerization*, Academic Press, London, 1995.
- [31] J.-P. Fouassier, *Photoinitiation, Photopolymerization, and Photocuring: Fundamentals and Applications*, Hanser Verlag, Munich, 1995.
- [32] A. Jusufi, C.N. Likos, M. Ballauff, *Colloid Polym. Sci.* 282 (2004) 910.
- [33] B. Liberelle, S. Giasson, *Langmuir* 24 (2008) 1550.
- [34] H. Huang, E. Ruckenstein, *J. Colloid Interf. Sci.* 275 (2004) 548.
- [35] M. Balastre, F. Li, P. Schorr, J. Yang, J.W. Mays, M.V. Tirrell, *Macromolecules* 35 (2002) 9480.



### 3.2 Binding of Oppositely Charged Surfactants to Spherical Polyelectrolyte Brushes: A Study by Cryogenic Transmission Electron Microscopy

*Larysa Samokhina<sup>a</sup>, Marc Schrinner<sup>a</sup>, Matthias Ballauff<sup>\*a</sup>, Markus Drechsler<sup>b</sup>*

<sup>a</sup> Physikalische Chemie I, <sup>b</sup> Makromolekulare Chemie II, University of Bayreuth, 95440 Bayreuth, Germany

Published in *Langmuir* 2007, 23, 3615 – 3619.

## Binding of Oppositely Charged Surfactants to Spherical Polyelectrolyte Brushes: A Study by Cryogenic Transmission Electron Microscopy

Larysa Samokhina, Marc Schrinner, and Matthias Ballauff\*

Physikalische Chemie I, University of Bayreuth, 95440 Bayreuth, Germany

Markus Drechsler

Makromolekulare Chemie II, University of Bayreuth, 95440 Bayreuth, Germany

Received October 31, 2006. In Final Form: January 17, 2007

The formation of a complex between an anionic spherical polyelectrolyte brush (SPB) and the cationic surfactant cetyltrimethylammonium bromide (CTAB) is investigated. The SPB consists of long chains of the strong polyelectrolyte poly(styrene sulfonate) (PSS), which are bound chemically to a solid poly(styrene) core of 56 nm in radius. The SPB are dispersed in water, and the ionic strength is adjusted by addition of NaBr. The resulting complexes are investigated in dilute solution by dynamic light scattering, by electrophoretic light scattering, and by cryogenic transmission electron microscopy (cryo-TEM). The formation of the complex between the SPB and the surfactant can be monitored by a strong shrinking of the surface layer when adding CTAB to dilute suspensions (0.01 wt %) and by a decrease of the effective charge of the complexes. Complex formation starts at CTAB concentrations lower than the critical micelle concentration of this surfactant. If the ratio  $r$  of the charges on the SPB to the charge of the added surfactant is exceeding unity, the particles start to flocculate. Cryo-TEM images of the complexes at  $r = 0.6$  measured in salt-free solution show that the surface layer composed of the PSS chains and the adsorbed CTAB molecules is partially collapsed: A part of the chains form a dense surface layer while another part of the chains or aggregates thereof are still sticking out. This can be deduced from the cryo-TEM micrographs as well as from the hydrodynamic radius, which is still of appreciable magnitude. The 1:1 complex ( $r = 1.0$ ) exhibits a fully collapsed layer formed by the PSS chains and CTAB. If the complex is formed in the presence of 0.05 M NaBr,  $r = 0.6$  leads to globular structures directly attached to the surface of the core particles. All structures seen in the cryo-TEM images can be explained by a collapse transition of the surface layer brought about by the hydrophobic attraction between the polyelectrolyte chains that became partially hydrophobic through adsorption of CTAB.

### Introduction

Polyelectrolyte–surfactant complexes (PSC) have received a lot of attention recently, partly because of the fundamental interest in these systems and partly because of the potential application these systems may have.<sup>1–5</sup> The micellar complexes of the polyelectrolyte chains and the surfactant are formed in salt-free solutions at the critical aggregation concentration, which is much lower than the critical micelle concentration (cmc) in the pure surfactant solution.<sup>6</sup> In general, it is understood that the strong binding of the surfactant by the polyelectrolyte chains is driven by electrostatic as well as by hydrophobic interactions. Hence, the supramolecular structures resulting from this aggregation will depend directly on the details of the molecular structure.<sup>5–11</sup> The interaction of free polyelectrolyte chains with surfactants

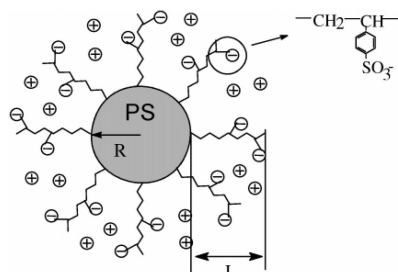
seems to be a well-studied problem by now and a rather clear understanding has emerged.

However, information on the interaction of surfactants with polyelectrolyte chains tethered to solid surfaces, that is, with polyelectrolyte brushes, seems to be scarce by now. While polyelectrolyte brushes have been the subject of intense research during the last 15 years,<sup>12–24</sup> only a few studies have been devoted to the interaction of these systems with surfactants in aqueous solution.<sup>25–27</sup> Thus, Pyshkina et al. studied the uptake of  $n$ -alkyltrimethylammonium bromides by dense planar brushes of poly(acrylic acid).<sup>25</sup> They found that the amount of bound

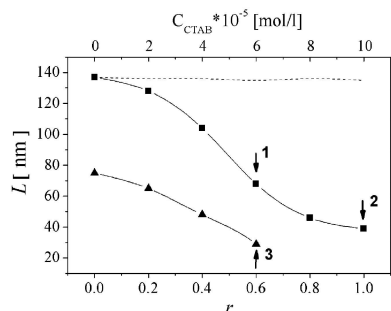
\* To whom correspondence should be addressed. E-mail: matthias.ballauff@uni-bayreuth.de.

- (1) Ober, C. K.; Wegner, G. *Adv. Mater.* **1997**, *9*, 17.
- (2) Zhou, S.; Chu, B. *Adv. Mater.* **2000**, *12*, 545.
- (3) Shpak, A. V.; Pirogov, A. V.; Slipigun, O. A. *Anal. Bioanal. Chem.* **2005**, *382*, 504.
- (4) Tao, Ch.; Zheng, S.; Moehwald, H.; Li, J. *Langmuir* **2003**, *19*, 9039.
- (5) *Polymer-Surfactant Systems*; Kwak, J. C. T., Ed.; Surfactant Science Series 77; Marcel Dekker: New York, 1998; p 7.
- (6) Kogej, K.; Škerjanc, J. *Langmuir* **1999**, *15*, 4251.
- (7) Kogej, K.; Evmenenko, G.; Theunissen, E.; Škerjanc, J.; Berghmans, H.; Reynaers, H.; Bras, W. *Macromol. Rapid Commun.* **2000**, *21*, 1226.
- (8) Kogej, K.; Evmenenko, G.; Theunissen, E.; Berghmans, H.; Reynaers, H. *Langmuir* **2001**, *17*, 3175.
- (9) Bronich, T. K.; Kabanov, A. V.; Kabanov, V. A.; Yu, K.; Eisenberg, A. *Macromolecules* **1997**, *30*, 3519.
- (10) Gao, Z.; Wasylishen, R. E.; Kwak, J. C. T. *J. Colloid Interface Sci.* **1988**, *126*, 371.
- (11) Hansson, P.; Lindman, B. *Curr. Opin. Colloid Interface Sci.* **1996**, *1*, 604.

- (12) Pincus, P. *Macromolecules* **1991**, *24*, 2912.
- (13) Borisov, O. V.; Birshtein, T. M.; Zhulina, E. B. *J. Phys. (Paris)* **1991**, *1*, 512.
- (14) Zhulina, E. B.; Borisov, O. V.; Birshtein, T. M. *Macromolecules* **1999**, *32*, 8189.
- (15) Ahrens, H.; Förster, S.; Helm, C. A. *Phys. Rev. Lett.* **1998**, *81*, 4172.
- (16) Biesalski, M.; Johannsmann, D.; Rühle, J. *J. Chem. Phys.* **2004**, *120*, 8807.
- (17) Rühle, J.; et al. *Adv. Polym. Sci.* **2004**, *165*, 79.
- (18) Advincula, R. C.; Brittain, W. J.; Caster, K. C.; Rühle, J., Eds. *Polymer Brushes*; Wiley-VCH: Weinheim, 2004.
- (19) Guo, X.; Ballauff, M. *Langmuir* **2000**, *16*, 8719.
- (20) Guo, X.; Ballauff, M. *Phys. Rev. E* **2001**, *64*, 051406.
- (21) Das, B.; Guo, X.; Ballauff, M. *Prog. Colloid Polym. Sci.* **2002**, *121*, 34.
- (22) Jusufi, A.; Likos, C. N.; Ballauff, M. *Colloid Polym. Sci.* **2004**, *282*, 910.
- (23) Wittemann, A.; Drechsler, M.; Talmon, Y.; Ballauff, M. *J. Am. Chem. Soc.* **2005**, *127*, 9688.
- (24) Tran, Y.; Auroy, P.; Lee, L.-T.; Stamm, M. *Phys. Rev. E* **1999**, *60*, 6984.
- (25) Pyshkina, O.; Sergeev, V.; Zevin, A.; Kabanov, V.; Gage, D.; Cohen, Stuart, M. *Langmuir* **2003**, *19*, 2000.
- (26) Konradi, R.; Rühle, J. *Macromolecules* **2005**, *38*, 6140.
- (27) Ishikubo, Akira Mays, Jimmy W.; Tirrell, Matthew. *Polym. Prepr.* **2005**, *46*, 27; Abstracts of Papers, 231st ACS National Meeting, Atlanta, GA, United States, March 26–30, 2006.

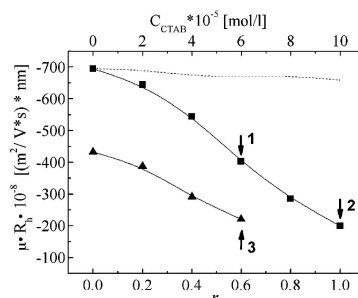


**Figure 1.** Schematic representation of a spherical polyelectrolyte brush. The colloidal particles consist of a poly(styrene) core onto which long chains of PSS have been grafted. The thickness  $L$  of the brush can be measured by dynamic light scattering.



**Figure 2.** Influence of complex composition on the brush thickness of polyelectrolyte spheres in the salt-free solution (squares) and in 0.05 M NaBr (triangles). The dashed line marks the respective change of  $L$  brought about by adding the same equivalent of NaBr to the solution. The arrows mark the compositions where the respective cryo-TEM images have been taken: arrow 1, Figure 4; arrow 2, Figure 5; arrow 3, Figure 6.

surfactant depends strongly on the grafting density. At lower grafting density, there was a second step in the binding isotherm, which was interpreted as the onset of a lamellar mesophase within the brush layer. Konradi and R  he studied the interaction of cationic surfactants on brushes obtained by chemical grafting of poly(methacrylic acid).<sup>26</sup> They determined the uptake of the surfactant, the degree of dissociation of the brush, and the height of the brush in a very detailed manner. A key result of this investigation is the uptake of surfactants and a concomitant decrease of the brush height takes place at very low surfactant concentrations. The authors explained this by the binding of the surfactant to the polyelectrolyte chains which thus become hydrophobic. In this way, a collapse transition is induced even if the uptake of surfactant is very small. At a critical concentration, which is found to be slightly lower than the cmc, the brush takes up a large amount of surfactant and shrinks further. In this regime, the degree of binding is approaching unity. From these results, Konradi and R  he suggested a model of the local structure that surmises the formation of spherical micellar structures by the surfactant within the brush layer. Finally, Tirrell and co-workers investigated the interactions of poly(styrenesulfonate) brushes in the presence of cationic surfactants.<sup>27</sup> Using the surface force apparatus, they also found contraction of the brush at very low surfactant concentrations. At sufficiently high surfactant concentration, they found the onset of attractive interaction between the brush layers, which was explained by hydrophobic forces.



**Figure 3.** Analysis of the electrophoretic mobility of the particles in presence of the surfactant CTAB. The mobility multiplied by the hydrodynamic radius  $R_h$  (see Figure 2) is plotted as the function of the charge ratio in the salt-free solution (squares) and in 0.05 M NaBr (triangles). The arrows mark the compositions where the respective cryo-TEM images have been taken: arrow 1, Figure 4; arrow 2, Figure 5; arrow 3, Figure 6.

All investigations done so far on complexes between polyelectrolyte brushes and surfactants have solely been done on planar systems. In this paper, we present the first investigation of the interaction of a spherical polyelectrolyte brush (SPB)<sup>18–23</sup> with a cationic surfactant cetyltrimethylammonium bromide (CTAB). We use SPB with long chains grafted to a poly(styrene) core of 56 nm in radius. The structure of these particles is shown schematically in Figure 1. The polyelectrolyte shell is made up by the strong electrolyte poly(styrenesulfonate) (PSS), which is charged regardless of the pH or salt concentration within the system.<sup>20</sup> In this quenched polyelectrolyte brush,<sup>18,20</sup> the pH is therefore not a decisive variable. The grafting density of the brush is of the order of  $0.1 \text{ nm}^{-2}$ . These well-defined core-shell latexes were prepared by photoemulsion polymerization.<sup>19</sup> Previous work done on these systems has demonstrated that spherical polyelectrolyte brushes present well-defined model systems that can be compared directly to the respective planar brushes.<sup>18–23</sup>

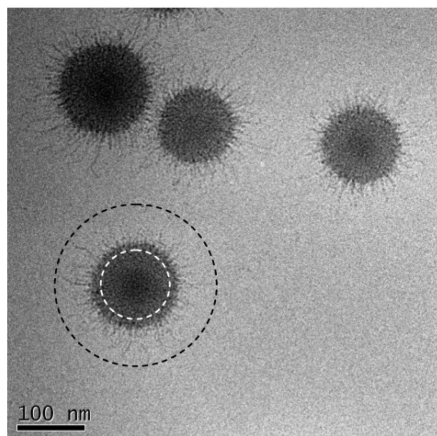
Two aspects of the previous work on SPB are central for the present study: (i) Nearly all counterions are confined within the brush layer and thus create an enormous osmotic pressure within this layer.<sup>12,13</sup> For the quenched SPB under consideration here, this has been shown directly by osmotic measurements.<sup>21</sup> Most of the confined counterions are directly bound to the polyelectrolyte chains.<sup>28</sup> (ii) Spherical polyelectrolyte brushes present an ideal model system for studies by cryogenic transmission electron microscopy (cryo-TEM).<sup>23</sup> The suspension of the particles is vitrified by rapid freezing and the spatial structure of the particles can be studied directly; no staining or other preparatory steps are necessary. Hence, the formation and the spatial structure of the complex of the SPB with the surfactant CTAB can be seen and analyzed directly.

### Materials and Methods

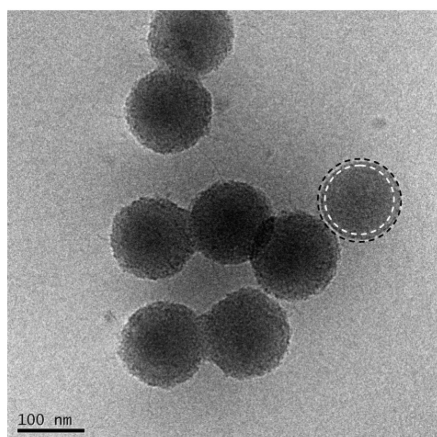
**Reagents.** Sodium bromide (Merck, analytical grade) and hexadecyltrimethylammonium bromide were used as received. Water was purified by reverse osmosis and subsequent ion exchange (Millipore Milli-Q). The SPB nanoparticles synthesized and characterized as described previously<sup>19,20</sup> have low polydispersity as determined by transmission electron microscopy. The grafting

(28) Dingenouts, N.; Patel, M.; Rosenfeldt, S.; Pontoni, D.; Narayanan, T.; Ballauff, M. *Macromolecules* **2004**, *37*, 8152.





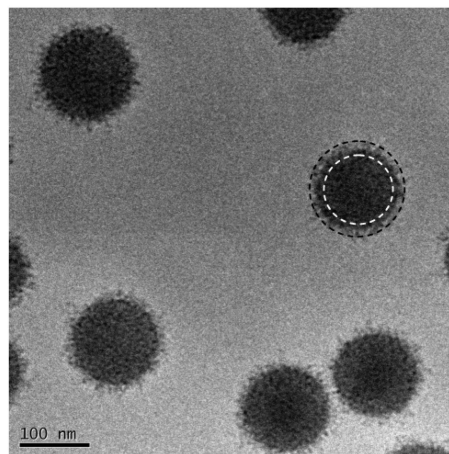
**Figure 4.** Cryo-TEM image of the PSC at a charge ratio of 0.6 in salt-free solutions (see arrow 1 in Figures 2 and 3). The radius of core indicated by a short-dashed line is 56 nm. The radius of polyelectrolyte–surfactant shell obtained from the DLS experiment is indicated as a long-dashed line.



**Figure 5.** Cryo-TEM image of the PSC at a charge ratio  $r = 1$  in salt-free solutions (see arrow 2 in Figures 2 and 3). The radius of core indicated by a short-dashed line is 56 nm. The radius of polyelectrolyte–surfactant shell obtained from the DLS experiment is indicated as a long-dashed line.

density is of the order of  $0.1 \text{ nm}^{-2}$ . The hydrodynamic radius is 188 nm as measured by dynamic light scattering (DLS) in 1 mM NaBr solution.

The aqueous solutions of polyelectrolyte–surfactant nanoparticle complexes were prepared by mixing concentrated solutions of the respective surfactant and the latex suspension (0.1 wt %) in order to get the required charge ratio  $r$ . This parameter characterizes a degree of binding of surfactant monomers by the brush surface and is calculated as the ratio of the number of positive charged ions to the total number of sulfonate groups in the polyelectrolyte layer. The latter number can be determined precisely from titration experiments. In order to ensure equilibrium, all samples were prepared a day before doing the analysis.



**Figure 6.** Cryo-TEM image of the PSC at a charge ratio of 0.6 in 0.05 M NaBr (see arrow 3 in Figures 2 and 3). The radius of polyelectrolyte–surfactant shell is  $\sim 30 \text{ nm}$  and corresponds to the one obtained from the DLS experiment (long-dashed circle).

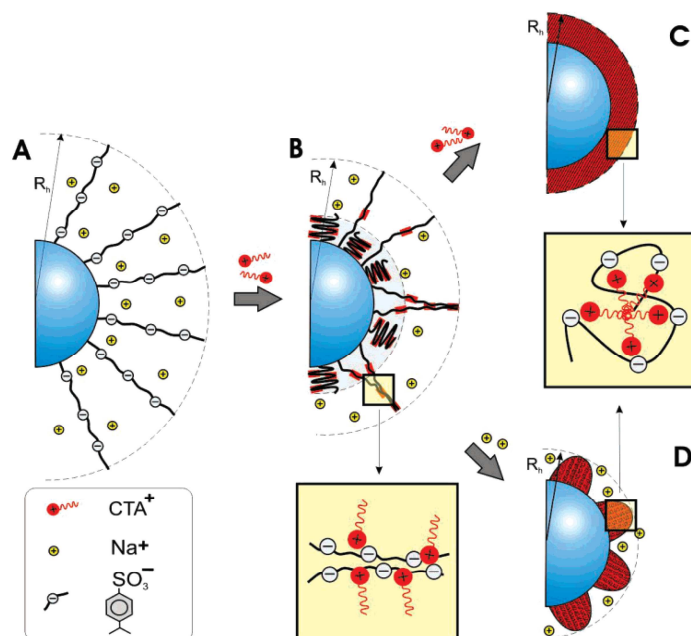
**Methods.** Cryo-TEM specimens were prepared by vitrification of thin liquid films supported on a TEM copper grid (600 mesh) in liquid ethane at its freezing point. Details of the procedure may be found in ref 23. The size (hydrodynamic radius) and electrophoretic mobility of the spherical nanoparticles were studied by dynamic and electrophoretic light scattering methods. The measurements were carried out with the Zetasizer Nano ZS, Malvern Instruments (4-mW He–Ne laser of 633 nm) at  $25^\circ\text{C}$  under an angle of  $173^\circ$ . For all our samples, the folded capillary cells (Malvern Instruments) were used in the electrophoretic mobility study and glass cuvettes to measure the size. Scattering data were analyzed by the CONTIN algorithm to estimate the diameter of the nanoparticles.

### Results and Discussion

As demonstrated in previous investigations, DLS is ideally suited to determine the overall size of the spherical polyelectrolyte brushes in solution.<sup>19,20</sup> DLS leads to the hydrodynamic radius  $R_H$  of the particles with great precision. Since the radius  $R$  of the practically monodisperse core particles<sup>19</sup> is known precisely, the thickness  $L$  of the polyelectrolyte layer on the surface of these core particles (see Figure 1) can be obtained through  $L = R_H - R$ . Previous work done by DLS on quenched SPB has demonstrated that  $L$  decreases with increasing salt concentration.<sup>20</sup> This is due to the increasing ionic strength, which causes the transition from the osmotic brush to the salted brush at high salt concentration.<sup>12,13,15,18–20</sup> However, while electrostatic interaction will determine the brush height  $L$  at low salt concentrations, ion-specific interactions may play a role at higher salt concentrations and may even lead to a total collapse of the brush layer.<sup>16,29</sup> For the SPB, this is followed by a flocculation of the particles.<sup>29</sup> The phase transition within the brush layer can be reversed at higher concentrations of added salt leading to a salting-in again.<sup>29</sup> These investigations have also demonstrated that equilibrium may always be attained in the brush layers due to their relatively small height  $L$  of the brush layer (30–200 nm).

(29) Mei, Y.; Ballauff, M. *Eur. Phys. J. E* **2005**, *16*, 341.





**Figure 7.** Schematic model of the spatial structure of the complexes from spherical polyelectrolyte brushes and the cationic surfactant CTAB. Model A corresponds to the spherical polyelectrolyte brush in salt-free solution, that is, with sodium counterions. Models B and C refer to the complex of the brush particles with CTAB at  $r = 0.6$  (B) and  $1.0$  (C) at a low ionic strength. This corresponds to the cryo-TEM images in Figures 4 and 5, respectively. Model D refers to the structure formed by the brush particles and the surfactant at a higher ionic strength (50 mM NaBr). The corresponding cryo-TEM image is shown in Figure 6.

Figure 2 displays the brush thickness  $L$  of the SPB measured in dilute solution (0.01 wt %) in the presence of an increasing concentration of CTAB. The parameter of the curves is the ionic strength in solution. At lowest ionic strength (squares in Figure 2), there is a marked decrease of  $L$  even at the smallest surfactant concentration. It needs to be noted that the concentration of CTAB is far below its cmc ( $10^{-3}$  M) but of the same order of magnitude as the critical association concentration of free PSS chains (see ref 6). The dashed line shows the experimental data obtained by DLS upon addition of the same amount of NaBr.

Virtually no shrinking takes place due to screening of charges at these low concentrations. This indicates that the interaction of CTAB with the brush layer is mainly determined by hydrophobic interaction of the alkyl chains of the surfactant with the hydrophobic parts of PSS chains.

Adding salt leads to a marked shrinking of the brush layer as already observed in previous investigations.<sup>15–17,19,20,26</sup> If added salt is present, adding CTAB leads to a marked shrinking as well that, however, is less pronounced than in the case of salt-free solutions. Moreover, a new feature enters above  $r = 0.6$ : Here the suspension flocculates, and it is evident that the colloidal stabilization of the SPB by the polyelectrolyte chains is not operative anymore.

Figure 2 indicates that there must be a strong binding of CTAB even at lowest surfactant concentrations. This is well supported by a qualitative analysis of the electrophoretic mobility  $\mu$  of the SPB as the function of CTAB concentration. Neglecting the contribution of the counterions to the measured mobility,  $\mu$  is

proportional to the effective charge of the particles and inversely proportional to its hydrodynamic radius  $R_H$ .<sup>30</sup> Figure 3 therefore displays the product of  $\mu$  and the hydrodynamic radius  $R_H$ . From the strong decrease of the effective charge that is evident from Figure 3 we conclude that virtually all of the CTAB molecules in the system are taken up by the brush layer. This is in accordance with previous studies.<sup>26</sup>

As already mentioned in the Introduction, cryo-TEM allows us to observe directly the structure of the complex between the SPB and CTAB. It should be noted that the surface layer of the PSS chains in the absence of CTAB is practically invisible in the cryo-TEM images. The contrast provided by the sodium counterions is too small and heavy ions such as, for example, cesium or iodine counterions would be needed.<sup>23</sup>

We first discuss the experiments done in salt-free solutions. The cryo-TEM images of PSS/CTAB complexes shown in Figure 4 and Figure 5 refer to the charge ratio  $r = 0.6$  (arrow 1 in Figures 2 and 3) and  $r = 1.0$  (arrow 2 in Figures 2 and 3, respectively), both taken in salt-free solutions. Both clearly indicate the core-shell morphology of the SPB and their complexes with CTAB. The larger long-dashed lines around one particle indicate the overall dimensions as determined by DLS while the smaller dashed circle indicates the size of the core. Figure 4 and Figure 5 now give a clear idea of the structural transition effected by adding CTAB: The contraction of the surface layer as measured through the decrease of  $L$  (see Figure

(30) Evans, D. F.; Wennerström, H. *The Colloidal Domain Where Physics, Chemistry, and Technology Meet*; Wiley-VCH: New York, 1994.

2) is brought about by a strong adsorption of surfactant to the polyelectrolyte chains. At  $r = 0.6$  displayed in Figure 4, chainlike objects extending from the surface become visible. Since single chains are practically invisible under the present conditions, we conclude that a part of the chains have aggregated to form bundles. However, the hydrodynamic radius of the particles is still considerably higher than the extension of the chains or aggregates seen in Figure 4. Obviously, there must be a part of the chains that do not aggregate but remain strongly stretched as in the surfactant-free state.

Figure 5 shows that the surface layer is entirely collapsed if the charge ratio  $r$  is adjusted to unity. The surfactant has been fully adsorbed by the polyelectrolyte brush layer, and the now hydrophobic chains of the polyelectrolyte/surfactant complex form a dense layer. Since  $r = 1$ , all electrostatic repulsion is gone and the bundlelike aggregates seen for  $r = 0.6$  must collapse. This is also evident from the hydrodynamic radius indicated by the larger dashed circle in Figure 5. Here  $R_H$  agrees with the dimensions of the particles visible by cryo-TEM. The full collapse of the chains attached to the surface must obviously lead to a total loss of colloidal stability. Hence, the complex of the SPB and CTAB must flocculate, which is indeed observed. This is also evident from Figure 5 showing clusters of aggregated SPB spheres.

Figure 6 displays the cryo-TEM micrographs referring to a charge ratio  $r = 0.6$  but at higher ionic strength (0.05 M NaBr). Evidently, the long bundlelike aggregates are gone and much smaller globular structures become visible that are attached directly to the surface. Moreover, the hydrodynamic radius (see larger dashed line in Figure 6) virtually coincides with the overall dimensions of the particles. Thus, the rather high ionic strength leads to a screening of the mutual repulsion of the still negatively charged surface structures at  $r = 0.6$ . The colloidal stability is very weak, and adding more surfactant at this ionic strength is followed by flocculation. However, the residual interaction between the complexes attached to the surface prevents the formation of a dense surface layer as observed at  $r = 1.0$  (see Figure 5).

All findings discussed in conjunction with Figures 2–6 suggest that the adsorption of the hydrophobic  $\text{CTA}^+$  ions leads to marked structural changes at the surface of the spherical polyelectrolyte brushes. A possible explanation of these observations, in particular of Figure 4, may be sought in a collapse of the brush layer due to the partial hydrophobization of the polyelectrolyte chains by the adsorbed CTAB. Recent theoretical models suggest that under certain conditions the collapse of a polymer or polyelectrolyte brush can be accompanied by an intrabrush microphase segregation and bimodal distribution of the chains with respect to their extension above the surface. Hence, a dense layer is formed near the grafting surface by a population of collapsed chains, while other chains remain extended in the solution and form a dilute peripheral part of the brush. This part determines the hydrodynamic radius. In particular, in ref 31 this mechanism was proposed in the case of brush collapse due to formation of

clusters comprising multiple monomers of grafted chains. Pryamitsyn et al.<sup>32</sup> have demonstrated that a weakly dissociated polyelectrolyte brush may undergo a collapse transition in a poor solvent resulting in a bimodal distribution of the surface chains. A bimodal chain end distribution has also been predicted in ref 33 where complexation of nonionic polymer brushes with surfactants has been considered. This theoretical model is in qualitative agreement with the interpretation of Figure 4. A part of the chains not included in this surface layer is seen from the hydrodynamic radius, which is still of appreciable magnitude. Hence, there must be a bimodal chain end distribution.

### Conclusion

Figure 7 summarizes the above findings in a schematic manner: At low ionic strength, that is, without added salt, the surfactant ions form a complex with the polyelectrolyte chains on the surface of the SPB already at lowest concentrations of the surfactant. This strong tendency for assembly is driven by ionic attraction and by the hydrophobic interaction of the alkyl moieties. This was already obvious from previous investigations using planar brushes.<sup>25–27</sup> The entirely new feature shown here by cryo-TEM is the formation of bundlelike aggregates at finite charge ratio  $r$  leading to a laterally inhomogeneous surface layer (see Figure 4). The peculiar structure is thus indicative for a collapse transition<sup>31</sup> of the surface layer due to the partial hydrophobization of the polyelectrolyte chains. This is shown schematically in Figure 7B. This transition within the brush layer leads to a bimodal distribution of the chains where a part is localized in a dense surface layer and another part still is stretching out as is seen from the hydrodynamic radius of the particles. If the ionic strength is increased by adding NaBr, the collapse of the brush induced by added surfactant is not accompanied by intrabrush segregation and only collapsed (relatively dense) layer proximal to the surface is found. Moreover, in this regime, the collapsed layer may lose its lateral continuity and split into pinched collapsed domains (see Figure 7D). Only if  $r = 1$ , at total collapse is seen regardless of the salt concentration (Figure 7C) and the PSS chains together with the CTAB form a dense homogeneous layer on the surface of the core. The balance of hydrophobic attraction and electrostatic repulsion can therefore lead to a collapse transition of the surface layer, which is laterally inhomogeneous.

**Acknowledgment.** The authors are indebted to O. Borisov for helpful discussions. Financial support by the European Community's Sixth Framework Programme through a Marie Curie Research Training Network POLYAMPHI, and by the Deutsche Forschungsgemeinschaft, SFB 481 Bayreuth, is gratefully acknowledged.

LA063178T

(31) Wagner, M.; Brochard-Wyart, F.; Hervet, H. and de Gennes, P.-G. *Colloid Polym. Sci.* **1993**, 271, 621.

(32) Pryamitsyn, V. A.; Leermakers, F. A. M.; Fleer, G. J.; Zhulina, E. B. *Macromolecules* **1996**, 29, 8260.

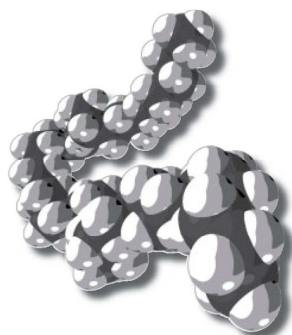
(33) Currie, E. P. K.; Fleer, G. J.; Cohen, Stuart, M. A.; Borisov, O. V. *Eur. Phys. J. E.* **2000**, 1, 27.

### 3.3 Mechanism of the Formation of Amorphous Gold Nanoparticles within Spherical Polyelectrolyte Brushes

*Marc Schrunner<sup>a</sup>, Frank Polzer<sup>a</sup>, Yu Mei<sup>a</sup>, Yan Lu<sup>a</sup>, Björn Haupt<sup>a</sup>, Matthias Ballauff<sup>\*a</sup>, Astrid Gödel<sup>b</sup>, Markus Drechsler<sup>b</sup>, Johannes Preussner<sup>c</sup>, Uwe Glatzel<sup>c</sup>*

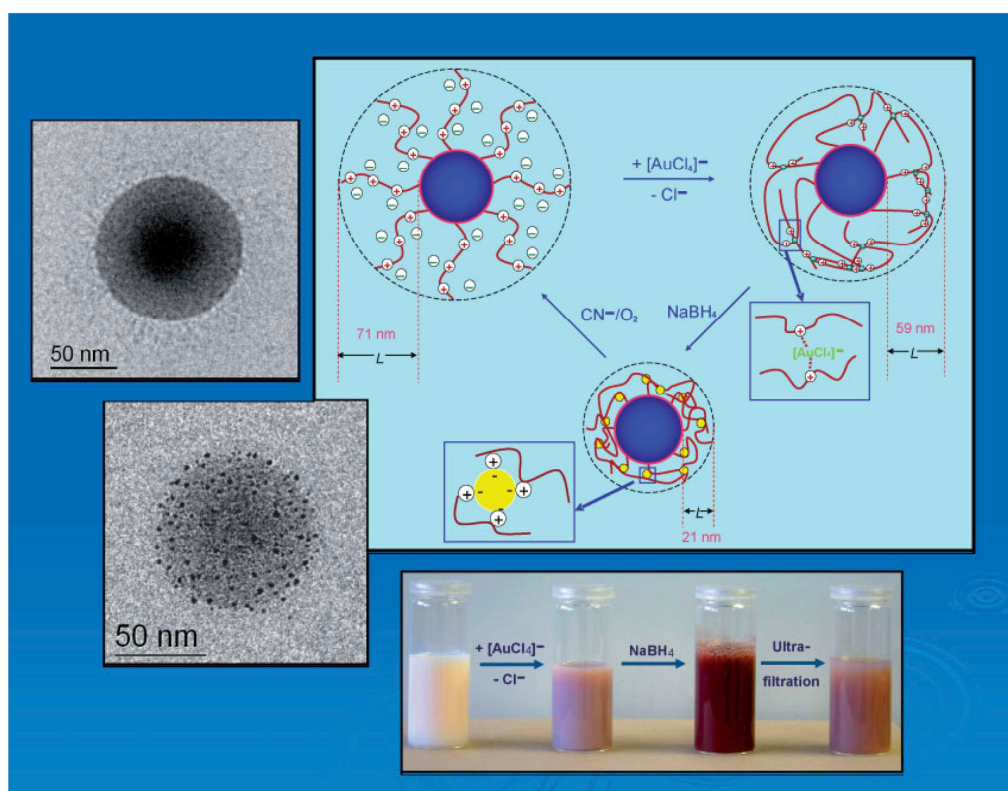
<sup>a</sup> Physikalische Chemie I, <sup>b</sup> Makromolekulare Chemie II, <sup>c</sup> Metallische Werkstoffe, University of Bayreuth, 95440 Bayreuth, Germany

Published in *Macromolecular Chemistry and Physics* 2007, 208, 1542 – 1547.



# Macromolecular Chemistry and Physics

Founded by  
Hermann Staudinger



14/2007

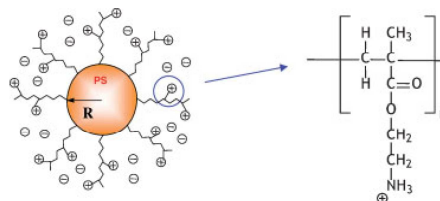


WILEY-VCH

# Mechanism of the Formation of Amorphous Gold Nanoparticles within Spherical Polyelectrolyte Brushes

Marc Schrunner, Frank Polzer, Yu Mei, Yan Lu, Björn Haupt, Matthias Ballauff,\* Astrid Gödel, Markus Drechsler, Johannes Preussner, Uwe Glatzel

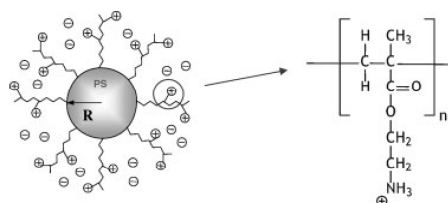
We present a comprehensive investigation on the formation of gold nanoparticles in spherical polyelectrolyte brushes. These colloidal carrier particles consist of a solid polystyrene core onto which long cationic polyelectrolyte chains are grafted. Immersed in water these polyelectrolyte chains can be used to enrich  $\text{AuCl}_4^-$  ions. The metal ions thus confined in the polyelectrolyte layer can be reduced to gold nanoparticles of approximately 1 nm diameter. Cryogenic transmission electron microscopy shows that the Au particles are located near the surface and exhibit a narrow size distribution. Measurements by dynamic light scattering demonstrate that the polyelectrolyte chains are located near the surface of the core particles. This is explained by a crosslinking of the cationic polyelectrolyte chains by the nanoparticles that carry a negative charge. If the Au nanoparticles are removed, the spherical polyelectrolyte brushes re-expand. High-resolution electron microscopy together with wide-angle X-ray scattering measurements demonstrates that the Au nanoparticles are amorphous. We demonstrate that these Au nanoparticles exhibit catalytic activity for hydrogenation reactions that is slightly below the one of Pt and Pd nanoparticles.



## Introduction

Metallic nanoparticles are at the center of modern nanotechnology since these particles may exhibit optical or catalytic properties that differ significantly from the bulk properties of the respective metal.<sup>[1–8]</sup> In particular, gold nanoparticles (Au-NPs) have recently been the subject of a large number of publications.<sup>[9–11]</sup> It has been demonstrated that Au-NPs of diameters between 1 and 10 nm have interesting optical properties<sup>[5]</sup> and can be used in catalysis.<sup>[12–14]</sup> In nearly all cases reported so far

M. Schrunner, F. Polzer, Y. Mei, Y. Lu, B. Haupt, M. Ballauff  
Physikalische Chemie I, University of Bayreuth, 95440 Bayreuth,  
Germany  
E-mail: Matthias.Ballauff@uni-bayreuth.de  
A. Gödel, M. Drechsler  
Makromolekulare Chemie II, University of Bayreuth, 95440  
Bayreuth, Germany  
J. Preussner, U. Glatzel  
Metals and Alloys, University of Bayreuth, 95440 Bayreuth,  
Germany



**Figure 1.** Scheme of the cationic spherical polyelectrolyte brushes used as carriers for the Au nanoparticles. Linear cationic polyelectrolytes of poly(2-aminoethyl methacrylate) are densely grafted onto a solid PS core ( $R_H = 45$  nm). The  $\text{AuCl}_4^-$  ions are introduced as counter-ions and reduced within the brush layer to yield the Au nanoparticles.<sup>[19,20]</sup>

the size and the colloidal stability of the Au-NPs must be adjusted by surface-active agents such as, e.g., thiol-containing moieties.<sup>[15–18]</sup> Evidently, ligands attached chemically to the surface of Au-NPs must profoundly influence their electronic structure and hence change the optical properties concomitantly. Moreover, long alkyl or polymer chains attached to the surface of the nanoparticles will limit the access of reactants to the surface and thus influence the catalytic properties of the Au-NPs.

Recently, we demonstrated that spherical polyelectrolyte brushes (SPBs) can be used for the generation and stabilization of metallic nanoparticles.<sup>[19,20]</sup> These SPBs consist of a solid polystyrene (PS) core onto which long anionic or cationic polyelectrolyte chains are grafted. The structure of these particles is shown schematically in Figure 1. Immersed in water, these SPBs will swell to form a dense layer of polyelectrolyte chains on the surface of the core particles.<sup>[21–24]</sup> The counter-ions of the polyelectrolyte chains are nearly fully localized within this layer.<sup>[25]</sup> We have demonstrated that this confinement of the counter-ions may be used to immobilize metal ions.

Reduction of these immobilized metal ions with  $\text{NaBH}_4$  leads to nanoparticles of the respective metal.<sup>[19,20]</sup>

Work on platinum nanoparticles (Pt-NPs) immobilized in this way has demonstrated an unexpected high colloidal stability of these composite systems despite the absence of any additional stabilizing agent.<sup>[20]</sup> Here, we elucidate the mechanism of the formation of the metal nanoparticles in cationic SPBs in detail. The aim of the present study is to gain a better understanding of the structure of the composite particles and the reasons for their high stability.

## Experimental Part

### Materials

Cationic spherical polyelectrolyte brushes carrying chains of poly(2-aminoethyl methacrylate hydrochloride) (PAEMH) were synthesized as described recently.<sup>[19,21]</sup> The radius  $R$  of the core particles was 45 nm, the average contour length  $L_c$  of the grafted chains was 165 nm and the grafting density (number of chains per unit area)  $\sigma = 0.0017 \text{ nm}^{-2}$ . The entire number of charged groups in the polyelectrolyte layer was determined precisely by conductometric titration.<sup>[19]</sup>

In a typical experiment the Au-NPs were generated as follows: 120 mL of the latex (0.85 wt.-%) in pure water was placed in an ultrafiltration cell (NC 10 membrane filters, cellulosenitrate, Schleicher & Schuell, Germany) and 2 L of  $2.4 \times 10^{-4} \text{ M}$   $\text{HAuCl}_4$  solution were passed through the cell. Subsequently, 12 L of deionized water were passed through the cell to remove free  $\text{AuCl}_4^-$  ions. The suspension attained a yellowish color, which indicates an exchange of the counter-ions in the brush layer from  $\text{Cl}^-$  to  $\text{AuCl}_4^-$ . The suspension (30 mL) was diluted with 30 mL of deionized water and mixed slowly (see Table 1, samples 1–6) with a  $1.2 \times 10^{-3} \text{ M}$  solution of  $\text{NaBH}_4$  with stirring under an atmosphere of nitrogen. In one experiment (see Table 1, sample 7) the mixing was rapid. The reduction of the  $\text{AuCl}_4^-$  ions could be clearly seen by a change of color from yellowish to reddish. After completion of the reaction the suspension was again placed in an

**Table 1.** Experimental details and characterization of the synthesized Au-NPs.

Sample	$n(\text{AuCl}_4^-)^a$ mol	$r(\text{AuCl}_4^-)^b$	$w(\text{Au})^c$ %	$n(\text{Au})/n(\text{Red})^d$	$d_{\text{Au}}^e$ nm	Morphology <sup>f</sup>
1	$2.11 \times 10^{-4}$	1/8	7.5	1/1	$1.25 \pm 0.25$	Amorphous
2	$4.22 \times 10^{-4}$	1/4	7.5	1/1	$1.75 \pm 0.25$	Amorphous
3	$8.44 \times 10^{-4}$	1/2	7.5	1/1	$2.0 \pm 0.5$	Crystalline
4	$2.11 \times 10^{-4}$	1/8	7.5	1/1	$1.25 \pm 0.25$	Amorphous
5	$2.11 \times 10^{-4}$	1/8	8.5	1/2	$1.25 \pm 0.25$	Amorphous
6	$2.11 \times 10^{-4}$	1/8	9.5	1/3	$1.25 \pm 0.25$	Amorphous
7	$1.13 \times 10^{-3}$	2/3	9.8	2/3	$3.0 \pm 0.5$	Crystalline

<sup>a</sup>) Amount of  $\text{AuCl}_4^-$  introduced during ultrafiltration; <sup>b</sup>) Ratio of amount of introduced  $\text{AuCl}_4^-$  ions related to the total number of charges on the surface of the carrier particles; <sup>c</sup>) Content of Au-NPs of the composite system; <sup>d</sup>) Ratio of  $\text{AuCl}_4^-$  ions to the reducing agent  $\text{NaBH}_4$  used in the synthesis of Au-NPs; <sup>e</sup>) Diameter of generated Au-NPs generated on the carrier particles; <sup>f</sup>) Indicates the structure of the Au-NPs.



ultrafiltration cell and a fifty-fold volume of deionized water was passed through the cell. The purification was monitored by measuring the conductivity of the serum. The content of gold in the composite particles was determined by C, H, and N elemental analysis after burning off the organic material at 950 °C.

The Au-NPs were dissolved<sup>[26]</sup> by the dropwise addition of 2 mL of a  $6.12 \times 10^{-3}$  M NaCN solution to 30 mL of a suspension (0.2 wt.-%) at room temperature. The solution was flushed slowly with air in order to achieve a full oxidation of the Au-NPs. After  $\approx 3$  h the suspension had the white color of the latex without Au-NPs.

### Methods

Cryogenic transmission electron microscopy (cryo-TEM) was carried out as described previously.<sup>[27]</sup> High-resolution TEM (HR-TEM) was done using a Zeiss Libra 200 FE. Wide-angle X-ray scattering (WAXS) measurements were performed using a Bruker-AXS D8 Advance. Dynamic light scattering (DLS) was done using a Peters ALV 4000 light scattering goniometer.

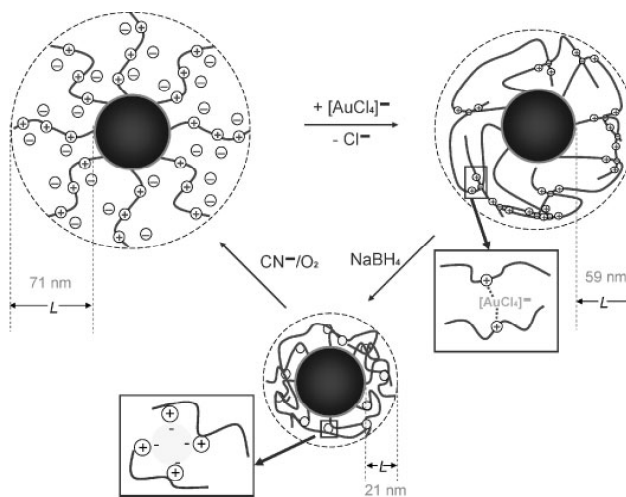
The catalytic activity was investigated using the model reaction of the reduction of 4-nitrophenol by  $\text{NaBH}_4$  to 4-aminophenol. In a typical run, 5 mL of a 4-nitrophenol solution ( $0.1 \text{ mmol} \cdot \text{L}^{-1}$ ) was added to an amount of sodium borohydride (0.0019 g). After mixing these solutions, we added a given number of the interesting metal nanoparticles to start the reduction. The progress of reduction was monitored by measuring the extinction of the reaction mixture at 400 nm as a function of time using a Lambda 650 spectrometer (Perkin Elmer).

## Results and Discussion

### Generation of the Au-NPs

The generation of the Au-NPs takes place only within the polyelectrolyte layer of the carrier particles as shown in Figure 2. The  $\text{AuCl}_4^-$  ions are introduced as counter-ions of the brush layer and all metal ions not firmly bound in this layer are flushed away by ultrafiltration. Hence, only the reduction of these immobilized  $\text{AuCl}_4^-$  ions will lead to well defined Au NPs.

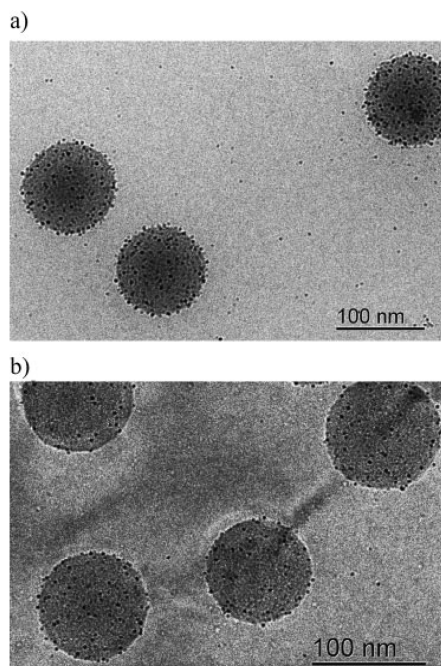
All stages of the formation of the nanoparticles within the brush layer can be followed easily by DLS, which determines the hydrodynamic radius  $R_H$  of the particles. Since the radius  $R$  of the core particles is exactly known, the thickness  $L$  of the surface layer can be obtained by  $L = R_H - R$  throughout all stages of the synthesis of the particles.



**Figure 2.** Scheme for the generation of Au-NPs and their dissolution with  $\text{CN}^-/\text{O}_2$ . In the first step  $\text{Cl}^-$  ions are exchanged against  $\text{AuCl}_4^-$  ions. The excess  $\text{AuCl}_4^-$  ions are removed subsequently by ultrafiltration. Replacing  $\text{Cl}^-$  ions by  $\text{AuCl}_4^-$  ions leads to a decrease of the layer thickness  $L$  from 71 to 59 nm. In the next step Au-NPs are generated by reduction of the confined  $\text{AuCl}_4^-$  counter-ions by  $\text{NaBH}_4$ . Here,  $L$  decreased to only 21 nm. In the last step Au-NPs are dissolved by complexation with  $\text{CN}^-/\text{O}_2$ . The original thickness of the surface layer is recovered in this step.

Figure 2 displays all results in a schematic fashion. Even low concentrations of  $\text{AuCl}_4^-$  ions lead to a considerable shrinkage of the polyelectrolyte layer on the surface of the core particles. Adding  $\text{AuCl}_4^-$  ions leads to a decrease of the surface layer thickness from 71 to 59 nm. This shrinkage of the surface layer is a result of partial crosslinking of the polyelectrolyte chains by the  $\text{AuCl}_4^-$  ions.<sup>[19]</sup> The  $\text{AuCl}_4^-$  ions are partially complexed by the polyelectrolyte chains. In this way the  $\text{AuCl}_4^-$  ions create a rather densely crosslinked mesh of polyelectrolyte chains. The local concentration of  $\text{AuCl}_4^-$  ions is, therefore, enlarged considerably. In the next step the reducing agent  $\text{NaBH}_4$  is added. This is followed by a collapse of the surface layer as the latter decreases to a thickness 21 nm. The micrographs of the resulting composite particles obtained by cryo-TEM are shown in Figure 3. It demonstrates that small Au-NPs have been formed in this step. The rate of the reducing step has a profound influence in that much smaller nanoparticles are generated by slower reduction (see Figure 3a and b). The present data, therefore, point to the preferred formation of small and amorphous particles if the reduction is slow. This problem, however, is in need of further investigation.

The marked decrease of  $L$  is not caused by ionic impurities introduced during the reduction step. This



**Figure 3.** Cryo-TEM images of Au-NP/SPB-composite particles. The Au-NPs are visible as black dots attached near to the surface: a) Table 1, sample 7 (crystalline), b) Table 1, sample 1 (amorphous).

can be shown by purifying the composite particles by extensive ultrafiltration against deionized water, which leads only to a moderate increase of  $L$  from 21 to 26 nm. Another reason for the decrease of the hydrodynamic radius may be sought in a degradation of the polyelectrolyte layers by cleavage or other side reactions. This explanation can be easily refuted by dissolution of the Au-NPs upon addition of NaCN in the presence of  $O_2$ . This process leads again to  $L = 69$  nm, which is identical to the starting value of 71 nm within the given limits of error. Hence, the polyelectrolyte chains of the brush layer are condensed by the Au-NPs as shown schematically in Figure 2. After the dissolution of the Au-NPs, the chains stretch again and assume their previous conformation.

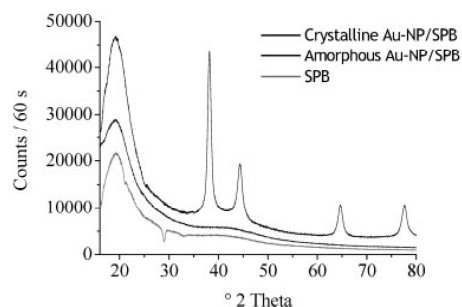
Hence, the Au-NPs formed by reduction within the brush layer lead to an additional crosslinking of the polyelectrolyte chains that extends far beyond the crosslinking effect<sup>[19]</sup> of the  $AuCl_4^-$  ions. This attractive interaction can possibly be related to a negative charge of the Au-NPs. Thus, the Au-NPs crosslink the polyelectrolyte chains by ionic interactions. A more direct

proof of the negative charge of the Au-NPs may be obtained by directly measuring their electrophoretic mobility. However, we know of no method that generates free and stable nanoparticles of such a small size in solution. Nevertheless, all results presented schematically in Figure 2 demonstrate that the Au-NPs and the cationic polyelectrolyte chains are intertwined in a dense mesh, which keeps the nanoparticles firmly bound to the surface of the core particles. This is the reason for the unusual stability of the composite particles mentioned above.

Additional experiments demonstrated that an excess of  $AuCl_4^-$  ions may lead to the formation of large and more polydisperse particles (Table 1, sample 7) or even coagulation of the carrier particles. In order to elucidate the influence of the various parameters, we varied the amount of added  $AuCl_4^-$  ions as well as the amount of the reducing agent  $NaBH_4$ . The Au-NP content of the composite particles could be varied from 7.5 to 9.5 wt.-% by using an excess of  $NaBH_4$  during the reduction. The size of the Au-NPs could be varied between 1 and 3.0 nm by varying the amount of bound  $AuCl_4^-$  ions. Table 1 (samples 1–6) summarize the results obtained by varying the amounts of  $AuCl_4^-$  ions and  $NaBH_4$  obtained by slowly reducing the  $AuCl_4^-$  ions.

#### Structure of the Au-NPs

The structure of the Au-NPs can be studied in further detail by HR-TEM and WAXS. In a previous study, we found that Au-NPs with sizes of  $\approx 3$  nm are crystalline.<sup>[19]</sup> However, Lu et al.<sup>[28]</sup> recently demonstrated that amorphous palladium-nanoparticles (Pd-NPs) can be synthesized. We have studied the crystal structure of the generated Au-NPs by HR-TEM and WAXS. The HR-TEM micrographs



**Figure 4.** Results of WAXS measurements of the Au-NPs on the spherical polyelectrolyte brushes. The uppermost scattering curve shows the WAXS diagram for crystalline Au-NPs having a size in the range of 3 nm (Table 1, sample 7). In the middle, the scattering curve for amorphous Au-NPs on SPB is shown (Table 1, sample 1). The lowermost curve is the scattering curve of the carrier particle without Au-NPs.



do not show any crystal planes. However, this analysis may be hampered by a limited resolution or the strong background caused by the core particles. In order to solve this problem further, we performed WAXS measurements. Figure 4 shows the comparison of the WAXS analysis of crystalline particles in the range of 2–3 nm on SPBs and for the amorphous Au-NPs in the range of 1.3 nm. Evidently, the small particles exhibit no Bragg reflections that are clearly visible for the larger Au-NPs. Clusters such as the Au<sub>55</sub>-cluster would exhibit characteristic WAXS profiles.<sup>[29]</sup> Hence, we conclude that the small Au-NPs generated on the spherical polyelectrolyte brushes are amorphous, similar to the amorphous Pd-NPs studied recently.<sup>[28]</sup>

### Catalytic Activity

Having discussed the synthesis and morphology of the Au-NPs, we now turn to a comparison of the catalytic properties of gold, platinum, and palladium nanoparticles. The catalytic activity of the Au-NPs can be monitored by UV-vis spectroscopy using the reduction of 4-nitrophenol to 4-aminophenol with an excess of NaBH<sub>4</sub> in aqueous solution. This reaction has repeatedly been used to test the catalytic activity of metal nanoparticles<sup>[20,30–33]</sup> and can now be regarded as a benchmark reaction for this purpose. In this way the measured results can be directly compared to the data supplied in the literature.<sup>[20,31–32]</sup> The rates of reduction were assumed to be independent of the concentration of NaBH<sub>4</sub> since this reagent was used in large excess compared to 4-nitrophenol.<sup>[30]</sup> Therefore, the kinetic data can be fitted by a first-order law.<sup>[20]</sup> Moreover, the apparent rate constant  $k_{app}$  was assumed to be proportional to the surface  $S$  of the metal nanoparticles present in the system.<sup>[20,31]</sup>

$$-\frac{dc_t}{dt} = k_{app} \cdot c_t = k_1 \cdot S \cdot c_t \quad (1)$$

where  $c_t$  is the concentration of 4-nitrophenol at time  $t$ ,  $k_1$  (s<sup>-1</sup>·m<sup>-2</sup>·L) is the rate constant normalized to  $S$ , and  $S$  itself is the surface area of the metal nanoparticles normalized to the unit volume of the system. In all cases the reduction of 4-nitrophenol was done with a high excess of NaBH<sub>4</sub>.<sup>[20,31]</sup> In order to obtain the activation energy of this reaction, measurements were performed at different temperatures. The resulting rate constants  $k_{app}$  can then be plotted versus  $S$ .<sup>[20,31]</sup>

For a test of the catalytic activity of the Au-NPs we used the following conditions: [4-Nitrophenol] =  $1 \times 10^{-4}$  M,  $T = 293.15$  K, and  $n(\text{NaBH}_4) = 1 \times 10^{-2}$  M. We obtain the following rate constant  $k_1 = 5.1 \times 10^{-1}$  s<sup>-1</sup>·m<sup>-2</sup>·L. This value is slightly lower than the ones recently

obtained for Pt-NP ( $k_1 = 5.62 \cdot 10^{-1}$  s<sup>-1</sup>·m<sup>-2</sup>·L) and Pd-NP ( $k_1 = 1.10$  s<sup>-1</sup>·m<sup>-2</sup>·L).<sup>[20,31]</sup> The activation energy of Au-NPs calculated from the data (43 kJ·mol<sup>-1</sup>) is of the same magnitude as the one found previously for Pt-NPs<sup>[20]</sup> or Pd-NPs<sup>[31]</sup> (both in the range of 44 kJ·mol<sup>-1</sup>). These data demonstrate that the Au-NPs exhibit a comparable catalytic activity for the reduction of 4-nitrophenol as the platinum or palladium nanoparticles studied recently.<sup>[20,31]</sup> There are differences between the catalytic activities, which increase in the series Au < Pt < Pd. In principle, two different reasons may be invoked to explain this finding: First, the activity may be related to a specific property of the metal. However, the fact that the three metals under consideration so far lead to the same activation energy may point to another possible reason: The substrates may exhibit an interaction with the surface of the particles that depends on the metal. This should become obvious when probing the catalytic activity of the particles for different ratios of the substrates and the total surface  $S$  over a wider range than used for the previously described analysis. Work along these lines is under way at present.

### Conclusion

We have elucidated the mechanism of the formation of Au-NPs within a cationic spherical polyelectrolyte brush. The excellent stability of the composite particles was traced back to a strong attraction between the Au-NPs and the polyelectrolyte chains, most probably caused by a negative surface charge of the Au-NPs. Cryo-TEM demonstrates that the Au-NPs are located near the surface and have sizes in the range of 1 to 2 nm at the most. HRTEM and WAXS show that the Au-NPs thus generated are amorphous. The Au-NPs are catalytically active, as has been shown by the reduction of 4-nitrophenol with NaBH<sub>4</sub>.

Acknowledgements: Financial support by the *Deutsche Forschungsgemeinschaft*, SFB 481, Bayreuth, by the *BASF-AG*, and by the *Fonds der Chemischen Industrie* is gratefully acknowledged.

Received: March 22, 2007; Revised: May 14, 2007; Accepted: May 15, 2007; DOI: 10.1002/macp.200700161

Keywords: catalysis; gold nanoparticles; polyelectrolytes; spherical polyelectrolyte brushes

[1] A. Henglein, *Chem. Rev.* **1989**, 89, 1861.

[2] A. P. Alivisatos, *Science* **1996**, 271, 933.

[3] R. G. Osichin, *Science* **1996**, 273, 1690.

- [4] C. Burda, X. Chen, R. Narayanan, M. A. El-Sayed, *Chem. Rev.* **2005**, *105*, 1025.
- [5] K. Watanabe, D. Menzel, N. Nilius, H.-J. Freund, *Chem. Rev.* **2006**, *106*, 4301.
- [6] Y. Negishi, T. Tsukuda, *J. Am. Chem. Soc.* **2003**, *125*, 4046.
- [7] H. Tsunoyama, H. Sakurai, N. Ichikuni, Y. Negishi, T. Tsukuda, *Langmuir* **2004**, *20*, 11293.
- [8] H. Tsunoyama, H. Sakurai, Y. Negishi, T. Tsukuda, *J. Am. Chem. Soc.* **2005**, *127*, 9374.
- [9] P. Pyykkö, *Angew. Chem.* **2004**, *116*, 4512.
- [10] M.-C. Daniel, D. Astruc, *Chem. Rev.* **2004**, *104*, 293.
- [11] G. Schmid, B. Corain, *Eur. J. Inorg. Chem.* **2003**, 3081.
- [12] D. Astruc, F. Lu, J. R. Aranzaes, *Angew. Chem.* **2005**, *117*, 8062.
- [13] M. D. Hughes, Y.-J. Xu, P. Jenkins, P. McMorn, P. Landon, D. I. Enache, A. F. Carley, G. A. Attard, G. J. Hutchings, F. King, E. H. Stitt, P. Johnston, K. Griffin, C. J. Kiely, *Nature* **2005**, *437*, 1132.
- [14] B. Yoon, H. Häkkinen, U. Landmann, A. S. Wörz, J.-M. Antonietti, S. Abbet, K. Judai, U. Heiz, *Science* **2005**, *307*, 403.
- [15] T. Yonezawa, T. Kunitake, *Colloids Surf. A* **1999**, *149*, 193.
- [16] L. Sun, R. M. Crooks, V. Chechik, *Chem. Commun.* **2001**, 359.
- [17] A. Labande, J. Ruiz, D. Astruc, *J. Am. Chem. Soc.* **2002**, *124*, 1782.
- [18] A. G. Kanaras, F. S. Kamounah, K. Schaumburg, C. J. Kiely, M. Brust, *Chem. Commun.* **2002**, 2294.
- [19] G. Sharma, M. Ballauff, *Macromol. Rapid Commun.* **2004**, *25*, 547.
- [20] Y. Mei, G. Sharma, Y. Lu, M. Drechsler, T. Irrgang, R. Kempe, M. Ballauff, *Langmuir* **2005**, *21*, 12229.
- [21] X. Guo, A. Weiss, M. Ballauff, *Macromolecules* **1999**, *32*, 6043.
- [22] X. Guo, M. Ballauff, *Langmuir* **2000**, *16*, 8719.
- [23] X. Guo, M. Ballauff, *Phys. Rev. E* **2001**, *64*, 051406.
- [24] Y. Mei, A. Wittemann, G. Sharma, M. Ballauff, Th. Koch, H. Gliemann, J. Horbach, Th. Schimmel, *Macromolecules* **2003**, *36*, 3452.
- [25] P. Pincus, *Macromolecules* **1991**, *24*, 1912.
- [26] T. Pal, A. Ganguly, *Analyst* **1987**, *112*, 1327.
- [27] A. Wittemann, M. Drechsler, Y. Talmon, M. Ballauff, *J. Am. Chem. Soc.* **2005**, *127*, 9688.
- [28] W. Lu, B. Wang, K. Wang, X. Wang, J. G. Hou, *Langmuir* **2003**, *19*, 5887.
- [29] R. E. Benfield, D. Grandjean, M. Kröll, R. Pugin, T. Sawitowski, G. Schmid, *J. Phys. Chem. B* **2001**, *105*, 1961.
- [30] S. Praharaj, S. Nath, S. K. Gosh, S. Kundu, T. Pal, *Langmuir* **2004**, *20*, 9889.
- [31] Y. Mei, Y. Lu, F. Polzer, M. Ballauff, M. Drechsler, *Chem. Mater.* **2007**, *19*, 1062.
- [32] G. Sharma, Y. Mei, Y. Lu, M. Ballauff, T. Irrgang, S. Proch, R. Kempe, *J. Catal.* **2007**, *246*, 10.
- [33] S. Panigrahi, S. Basu, S. Praharaj, S. Pande, S. Jana, A. Pal, S. K. Gosh, T. Pal, *J. Phys. Chem. C* **2007**, *111*, 4596.

### 3.4 Stable Bimetallic Gold-Platinum Nanoparticles Immobilized on Spherical Polyelectrolyte Brushes

*Marc Schrunner<sup>a</sup>, Sebastian Proch<sup>b</sup>, Yu Mei<sup>a</sup>, Rhett Kempe<sup>\*b</sup>, Nobuyoshi Miyajima<sup>c</sup>, Matthias Ballauff<sup>\*a</sup>*

<sup>a</sup> Physikalische Chemie I, <sup>b</sup> Anorganische Chemie II, <sup>c</sup> Bayerisches Geoinstitut, University of Bayreuth, 95440 Bayreuth, Germany

Published in *Advanced Materials* 2008, 20, 1928 – 1933.

DOI: 10.1002/adma.200702421

## Stable Bimetallic Gold–Platinum Nanoparticles Immobilized on Spherical Polyelectrolyte Brushes: Synthesis, Characterization, and Application for the Oxidation of Alcohols\*\*

By Marc Schrinner, Sebastian Proch, Yu Mei, Rhett Kempe,\*  
Nobuyoshi Miyajima, and Matthias Ballauff\*

Metallic nanoparticles have recently received much attention as catalysts. In particular, gold nanoparticles have been shown to be excellent catalysts for oxidation reactions.<sup>[1–5]</sup> Thus, in 1989 Haruta reported the low-temperature oxidation of CO by molecular oxygen using gold nanoclusters.<sup>[3]</sup> Catalysis under very mild conditions at room temperature is of particular interest. Recently, Miyamura et al. demonstrated that the aerobic oxidation of alcohols can be performed at room temperature by using gold nanoclusters stabilized by a polymer.<sup>[6]</sup> Nanometer-scale alloy particles composed of gold and platinum metals may be prepared that exhibit improved catalytic activities as compared to the pure Au nanoparticles.<sup>[5,7–10]</sup> In particular, Enache et al. were able to show that Au–Pd nanocrystals present excellent catalysts for the oxidation of primary alcohols.<sup>[11]</sup> Bimetallic Au–Pt nanoparticles (Au–Pt NPs) have been used recently in electrocatalysis.<sup>[12,13]</sup> Here, the question arises whether the alloy exhibits a miscibility gap, as in the bulk phase, or whether a homogeneous solid solution can be achieved.<sup>[14–19]</sup> Lou et al. showed that the lattice parameter of alloy nanoparticles scales linearly with the relative Au–Pt content in the composition.<sup>[14]</sup> On the other hand, De and Rao reported the formation of core/shell nanoparticles of Au and Pt at elevated temperatures.<sup>[16]</sup> Recent theoretical work suggests that the catalytic properties

of Au–Pt-NPs are superior to those containing Pt or Au alone.<sup>[19]</sup> Hence, Au–Pt NPs should be highly suitable for oxidation reactions under very mild conditions as, for example, in aqueous solutions at room temperature.

A central problem of the usage of catalytic nanoparticles is their stabilization against coagulation as well as their handling. Often, nanoparticles are stabilized by alkyl chains attached through thiol bonds to the surface of the metal.<sup>[5,20,21]</sup> However, the strong interaction of the thiol group with the surface of the nanoparticles may alter the catalytic properties of the metal profoundly. Also, filtering off nanoparticles after use in catalysis may be difficult. Leaching of heavy metal or even dissolution may be another problem when using metal nanoparticles as catalyst.

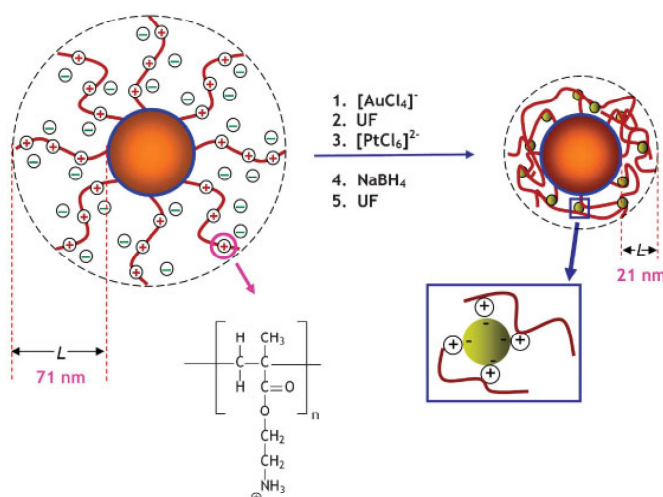
Recently, we have found that spherical polyelectrolyte brushes<sup>[22]</sup> (SPBs) present ideal carrier systems for nanoparticles.<sup>[23–25]</sup> Figure 1 shows these colloidal particles in a schematic manner: Long polyelectrolyte chains are attached to colloidal core particles (diameter: ca. 100 nm) made of polystyrene. Most of the counterions balancing the charge of the polyelectrolyte chain are confined<sup>[26]</sup> within the surface layer when the particles are immersed in water. Hence, metal ions such as, for example,  $[\text{AuCl}_4]^-$  can be immobilized within the polyelectrolyte layer. Reduction by  $\text{NaBH}_4$  under suitable conditions then leads to the formation of metal nanoparticles<sup>[23–25]</sup> localized on the surface of the colloidal carrier particles.

Here we use the spherical polyelectrolyte brushes for the generation of stable homogeneous nanoparticles composed of a Au–Pt alloy and analyze their catalytic activity. Figure 1 shows the method of synthesis employed here: First,  $[\text{AuCl}_4]^-$  ions are immobilized as counterions within the surface layer of cationic polyelectrolyte chains. Because we know the total number of charges on the surface of the core particles, the number of  $[\text{AuCl}_4]^-$  ions can be adjusted precisely in order to replace only a certain fraction of the  $\text{Cl}^-$ -counterions. After ultrafiltration,  $[\text{PtCl}_6]^{2-}$  ions are introduced in the same manner. A possible excess of metal ions is flushed away by ultrafiltration. Finally, reduction by  $\text{NaBH}_4$  leads to nanoparticles of the Au–Pt alloy of a given composition.

The advantages of this way of generating metallic nanoparticles are obvious: Because of the confinement of the

[\*] Prof. R. Kempe, S. Proch  
Inorganic Chemistry II  
University of Bayreuth  
95440 Bayreuth (Germany)  
E-mail: kempe@uni-bayreuth.de  
Prof. M. Ballauff, M. Schrinner, Y. Mei  
Physical Chemistry I  
University of Bayreuth  
95440 Bayreuth (Germany)  
E-mail: matthias.ballauff@uni-bayreuth.de  
Dr. N. Miyajima  
Bayerisches Geoinstitut  
University of Bayreuth  
95440 Bayreuth (Germany)

[\*\*] We acknowledge financial support by the Deutsche Forschungsgemeinschaft, SFB 481, Bayreuth, and by BASF AG. This work was also supported by NanoCat, an International Graduate Program within the Elitenetzwerk Bayern. Supporting Information is available online from Wiley InterScience or from the authors.



**Figure 1.** SPBs used as carriers for bimetallic Au–Pt NPs. Linear cationic polyelectrolytes of poly(2-aminoethyl methacrylate) are densely grafted onto a solid polystyrene (PS) core ( $R_1 = 45$  nm). The thickness of the polyelectrolyte layer  $L$  is about 71 nm [22].  $[\text{AuCl}_4]^-$  and  $[\text{PtCl}_6]^{2-}$  ions are introduced as counterions and reduced within the brush layer to generate bimetallic Au–Pt NPs. In a first step, a given number of the  $\text{Cl}^-$  counterions is replaced by  $[\text{AuCl}_4]^-$  ions. Ultrafiltration removes  $[\text{AuCl}_4]^-$  ions that have not been adsorbed. Finally,  $[\text{PtCl}_6]^{2-}$  ions are introduced and the system is purified again by ultrafiltration. Reduction is achieved by adding  $\text{NaBH}_4$ . All steps can be followed by dynamic light scattering, which allows to measure the thickness  $L$  of the surface layer.

counterions, nanoparticles are only generated within the polyelectrolyte layer. Stabilization of the nanoparticles against aggregation is effected by the colloidal carrier particles. Moreover, the handling of composite particles of a size of ca. 150 nm can be done easily. Because the metal nanoparticles carry no group stabilizing their surface, they exhibit a high catalytic activity.<sup>[22–24]</sup>

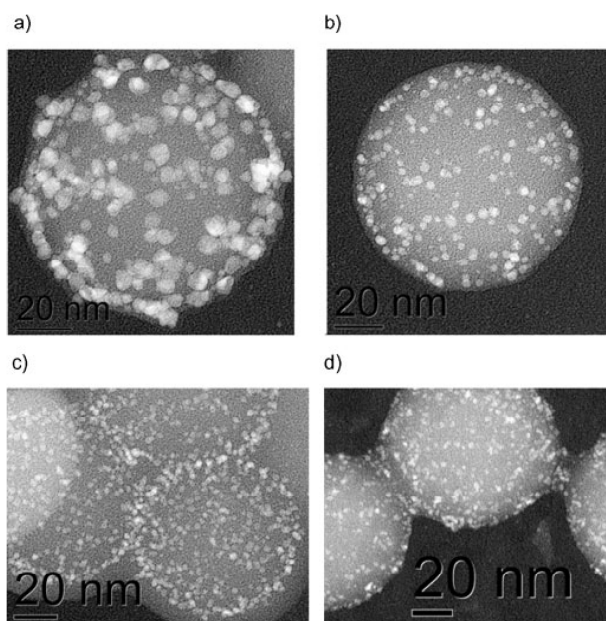
As indicated in Figure 1, the uptake of the metal ions that replace the chloride ions are also followed by a shrinking of the

surface layer. The thickness  $L$  of the surface layer, measured by dynamic light scattering, shrinks considerably when adding  $\text{AuCl}_4^-$  ions (see Fig. S1, Supporting Information). In order to avoid any surplus of free metal ions, the suspension is purified after this step by ultrafiltration against pure water. A further decrease of  $L$  is seen when adding the  $[\text{PtCl}_6]^{2-}$  ions in the next step. Hence, a mixture of ions of both ions is held firmly within the polyelectrolyte layer as a result of complexation.<sup>[25]</sup> The reduction is then followed by a further drastic reduction of  $L$  to

**Table 1.** Composition of the Au–Pt nanocomposites.

System[a]	$n([\text{AuCl}_4]^-)$ [mol]; $n([\text{PtCl}_6]^{2-})$ [mol][b]	Au/Pt[c] Theor.	Au/Pt[d] Exp.	Exp. metal content[e] [wt %]	$d_{\text{Au-Pt}}[f]$ [nm]
Au <sub>73</sub> Pt <sub>27</sub>	$3.30 \cdot 10^{-4}$ $0.82 \cdot 10^{-4}$	80:20	73:27	8.210	$4.0 \pm 0.5$
Au <sub>55</sub> Pt <sub>45</sub>	$2.47 \cdot 10^{-4}$ $1.65 \cdot 10^{-4}$	60:40	55:45	9.029	$3.0 \pm 0.5$
Au <sub>45</sub> Pt <sub>55</sub>	$1.65 \cdot 10^{-4}$ $2.47 \cdot 10^{-4}$	40:60	45:55	7.935	$2.0 \pm 0.5$
Au <sub>25</sub> Pt <sub>75</sub>	$0.82 \cdot 10^{-4}$ $3.30 \cdot 10^{-4}$	20:80	25:75	6.798	$1.3 \pm 0.5$
Au <sub>48</sub> Pt <sub>52</sub>	$1.03 \cdot 10^{-4}$ $1.03 \cdot 10^{-4}$	50:50	48:52	8.543	$2.0 \pm 0.5$
Au <sub>46</sub> Pt <sub>54</sub>	$0.52 \cdot 10^{-4}$ $0.52 \cdot 10^{-4}$	50:50	46:54	8.209	$1.8 \pm 0.5$

Sample name, amount of  $[\text{AuCl}_4]^-$  and  $[\text{PtCl}_6]^{2-}$  introduced during ultrafiltration. Theoretical ratio of Au and Pt on the SPB. Measured ratio Au/Pt in Au–Pt NPs. Total content of metal. Diameter of generated Au NPs generated on the carrier particles.

ADVANCED  
MATERIALS

**Figure 2.** TEM images from samples a)  $\text{Au}_{73}\text{Pt}_{27}$ , b)  $\text{Au}_{55}\text{Pt}_{45}$ , c)  $\text{Au}_{45}\text{Pt}_{55}$ , and d)  $\text{Au}_{25}\text{Pt}_{75}$  (see Table 1). For sake of clarity the contrast has been inverted.

approximately 20 nm. The same strong reduction was already found when synthesizing pure Au nanoparticles in the same carrier system.<sup>[23,24]</sup> The explanation for this strong reduction is schematically given in Figure 1: The metal nanoparticles carry, most probably, a negative surface charge. Thus, they strongly interact with the cationic polyelectrolyte chains. This is one of the reasons for the excellent stability of the composite of the colloidal carrier and the metal nanoparticles.

Six different ratios of Au to Pt have been used for generating the alloy nanoparticles. Table 1 summarizes the resulting compositions. As shown by elemental analysis, the measured compositions are rather close to the ratio adjusted through ion exchange. The total content of metal ranges from 7–9 wt %. It demonstrates that practically all metal ions introduced previously have been reduced to metallic nanoparticles. Moreover, Table 1 demonstrates that the synthesis of the Au–Pt NPs is highly reproducible. In the following the composite systems are named according to the composition of the alloy (see Table 1).

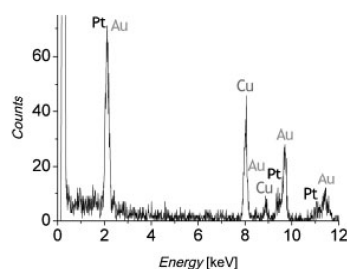
Figure 2 displays the images of four different particles obtained by transmission electron microscopy (TEM). Evidently, well-defined metallic nanoparticles have obtained for all ratios Au/Pt used herein. The average size of the

nanoparticles is given in Table 1, and decreases with increasing content of Pt. Moreover, the  $\text{Au}_{73}\text{Pt}_{27}$  particles have an irregular shape while a higher content of Pt leads to nearly perfect spherical particles. The reasons for these findings are not yet clear.

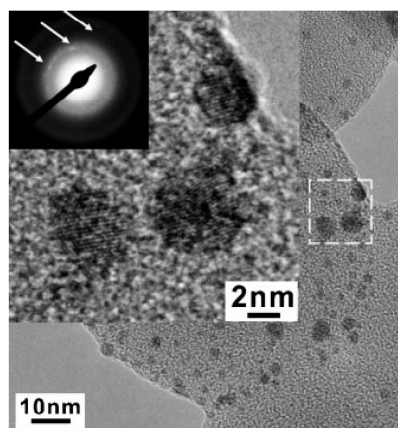
However, these microscopy images do not lead to any conclusion as to whether we see one sort of alloy particles, or two sorts of pure metal particles. Energy-dispersive X-ray (EDX) spectra of single nanoparticles, however, immediately demonstrated that the metal nanoparticles consist of an alloy. Figure 3 displays the EDX spectrum of one single nanoparticle from sample  $\text{Au}_{73}\text{Pt}_{27}$ . The peaks of both Au and Pt peaks are clearly visible. Moreover, spectra from an entire composite particle carrying approximately 30–50 nanoparticles superimpose with the spectra of an entire composite particle containing many nanoparticles (see Fig. S2, Supporting Information).

Hence, EDX demonstrates that the nanoparticles seen in the TEM images (Fig. 2) are true alloys.

Because Au and Pt exhibit a miscibility gap in bulk, the question arises whether the present method of preparation leads to a random mixture of metal atoms<sup>[14]</sup> or a core/shell structure of the particle.<sup>[16]</sup> This problem can directly be solved by high-resolution transmission electron microscopy (HR-TEM). Figure 4 displays the HR-TEM of  $\text{Au}_{73}\text{Pt}_{27}$ . The crystal lattice is directly seen



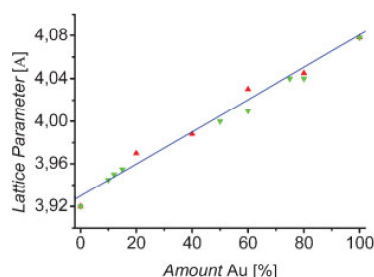
**Figure 3.** EDX spectrum of one single Au–Pt-NP on the surface of the carrier particle. The copper peaks are from the copper grid used as support in the measurements.



**Figure 4.** TEM image of  $\text{Au}_{73}\text{Pt}_{27}$  composite particles, with a HR-TEM image of three particles (lattice imaging) and the diffractogram in the insets.

throughout the entire particle. Moreover, electron diffraction (inset of Fig. 4) demonstrates the crystalline state of the nanoparticles.

A more detailed analysis of the crystal spacing as a function of the Au/Pt ratio can be done by wide-angle X-ray scattering (WAXS). The WAXS diffractograms (see Fig. S3, Supporting Information) exhibit a marked broadening of the peaks owing to their small size. A similar finding was already reported for Au–Pt nanoparticles synthesized by Lou et al.<sup>[14]</sup> The lattice spacing depend linearly on the composition (Vegard's law<sup>[19]</sup>). The lattice spacings obtained here are shown in Figure 5, together with the data of Lou et al.<sup>[14]</sup> Hence, sufficiently small Au–Pt nanoparticles form true solid solutions, and the bimetallic particles that form true solid solutions are expected to exhibit different chemical properties than the core/shell



**Figure 5.** Plot of the lattice parameter dependence on the composition of the alloy particle. (Red triangles: own measured values; green triangles: data from Zhong et al. [14].)

particles described in Ref. <sup>[11]</sup> Of course, the solid solution is not an equilibrium state, and heating the nanoparticles would certainly lead to demixing and a marked change of internal morphology.<sup>[16]</sup> It should be kept in mind, however, that the synthesis of these nanoparticles proceeds at room temperature. Thus, we demonstrated that well-defined homogeneous alloy nanoparticles can be obtained on spherical polyelectrolyte brushes without further stabilizing agents.

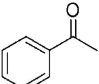
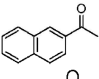
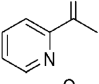
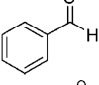
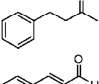
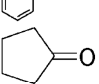
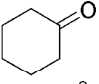
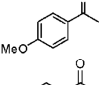
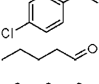
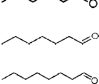
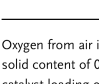
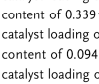
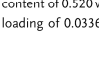

We now turn to the catalytic activity of the alloy nanoparticles. The catalytic oxidation of alcohols to aldehydes in presence of gold nanoparticles was studied by Miyamura et al.<sup>[6]</sup> The Au nanoparticles were stabilized by polystyrene in mixtures of dichloromethane and water. Platinum nanoparticles stabilized by a suitable resin were used by Yamada et al. for the aerobic oxidation of alcohols to aldehydes.<sup>[27]</sup> Here, we test for the first time the catalytic activity of Au–Pt alloys for this reaction. All reactions were carried out at room temperature using aerobic conditions. In one case the oxidation was carried out using pure  $\text{O}_2$  in order to determine the oxygen consumption. A total of 14 different alcohols was used and the conversion was determined after a given time. Table 2 gathers the results including the turnover numbers. Most notably, no phase transfer catalyst is needed for this reaction and the reaction conditions are very mild. A strong base is needed for the oxidation to proceed<sup>[27]</sup> otherwise small yields on the order of only 5% are achieved. Gas chromatography revealed that no byproduct is obtained under these conditions. This could be further confirmed by carrying out the oxidation of benzyl alcohol in presence of pure oxygen (see Supporting Information). We find full conversion within the given limits of error. Hence, water is the only product formed by this reaction (besides the aldehyde or ketone). These findings, and the data gathered in Table 2, demonstrate that a smaller yield can be traced back to a smaller reactivity, not to possible side reactions. The reactivity of the aliphatic substrate is much less than the one measured for the aromatic ones. Most probably, this is due to the stronger adsorption of the aromatic moieties on the metal surface (see Table 2).

A central question to be asked when considering technical applications of these catalysts is their stability against coagulation or dissolution. We find that systems containing pure Au nanoparticles are much less stable than the alloy particles. Substrates containing phenylgroups lead to considerable leaching of gold and even coagulation (see Table 2). A possible explanation of this finding may be sought in the strong interaction of Au with the phenyl groups already found by Miyamura et al.<sup>[6]</sup> However, alloy nanoparticles turned out to be fully stable under the same conditions. This finding is corroborated by an analysis of the composite particles before and after catalysis by cryogenic transmission electron microscopy (see Fig. S4, Supporting Information). This method allows us to directly visualize the particles in situ, that is, in aqueous suspensions.<sup>[22,28]</sup> No change or leaching of the nanoparticles is seen. Moreover, repeated use of the composite particles as catalysts did not lead to a noticeable decrease of catalytic activity (see Supporting Information).

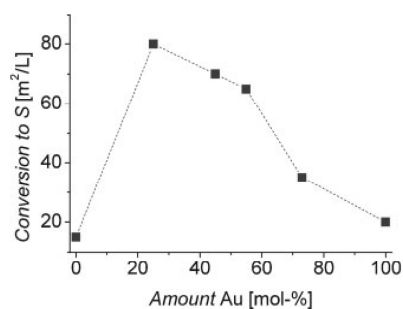


ADVANCED  
MATERIALS

**Table 2.** Selective oxidation of alcohols to aldehydes or ketones in presence of Au–Pt NPs at ambient conditions in water[a]. The first lines gives the yields while the second lines give the turnover numbers.

Product	Au <sub>100</sub> Pt <sub>0</sub> [h]	Au <sub>48</sub> Pt <sub>52</sub> [c]	Au <sub>46</sub> Pt <sub>54</sub> [d]	Au <sub>10</sub> Pt <sub>100</sub> [e]
	>99% <sup>[f]</sup> 2976	>99% 2976	>99% 2976	80% 2381
	81% 2411	70% 2083	63% 1875	40% 1190
	>99% <sup>[f]</sup> 2976	>99% 2976	>99% 2976	59% 1756
	>99% <sup>[f]</sup> 2976	>99% 2976	>99% 2976	>99% 2976
	73% 2173	73% 2173	78% 2321	46% 1369
	60% <sup>[f]</sup> 1786	68% 2024	71% 2113	65% 1935
	>99% 2976	>99% 2976	>99% 2976	45% 1339
	>99% 2976	>99% 2976	>99% 2976	58% 1726
	>99% <sup>[f]</sup> 2976	>99% 2976	>99% 2976	89% 2649
	>99% <sup>[f]</sup> 2976	>99% 2976	>99% 2976	77% 2292
	11% 327	10% 298	8% 238	9% 268
	45% 1339	40% 1190	47% 1399	41% 1220
	44% 1309	39% 1161	34% 1012	30% 893
	33% 982	26% 774	19% 565	21% 625

Oxygen from air is used as oxidizing agent. 0.31 mL Au<sub>100</sub>Pt<sub>0</sub> solution in water with a solid content of 0.342 wt % and a metal content of ca. 6.5 wt % Au corresponds to a catalyst loading of 0.0336 mol % Au. 0.28 mL Au<sub>48</sub>Pt<sub>52</sub> solution in water with a solid content of 0.339 wt % and a metal content of ca. 8 wt % Au–Pt corresponds to a catalyst loading of 0.0336 mol % metal. 1 mL Au<sub>46</sub>Pt<sub>54</sub> solution in water with a solid content of 0.094 wt % and a metal content of ca. 8 wt % Au–Pt corresponds to a catalyst loading of 0.0336 mol % metal. 1.16 mL Pt<sub>100</sub> solution in water with a solid content of 0.520 wt % and a metal content of ca. 1.1 wt % Pt corresponds to a catalyst loading of 0.0336 mol % Pt. [f]Coagulation of the composite particles.



**Figure 6.** Dependence of conversion (normalized to the surface area) on the amount of gold in bimetallic nanoparticle.

Figure 6 demonstrates that there is a synergistic effect of both metals in the nanoparticles related to their catalytic activity. Benzylalcohol was used as a substrate and the conversion was monitored under comparable conditions. Because the reaction proceeds on the surface of the nanoparticles, the reactivity has been normalized to the total surface provided by all nanoparticles present in the system.<sup>[22–24]</sup> Figure 6 shows that the conversion per unit area of metal surface goes through a maximum.

In conclusion, we presented the facile synthesis of Au–Pt nanoparticles immobilized on spherical polyelectrolyte brushes. The resulting particles are shown to be homogeneous solid solutions despite the fact that the bulk metals exhibit a miscibility gap. The catalytic activity for the oxidation of alcohols to the respective aldehydes goes through a maximum as the function of the Au/Pt composition. It should be noted that no surface stabilization was needed to keep these particles from coagulation. The stabilization is solely achieved by the spherical polyelectrolyte brushes on which the alloy nanoparticles are immobilized and the catalysis shows a very high selectivity towards aldehydes owing to the mild reaction conditions.<sup>[6,11]</sup> Hence, spherical polyelectrolyte brushes present a system that allows us to generate and to utilize alloy nanoparticles that exhibit properties widely differing from the properties of the respective bulk alloys.

## Experimental

**Materials:** Cationic spherical polyelectrolyte brushes carrying chains of poly(2-aminoethylmethacrylate hydrochloride) (PAEMH) were synthesized as described recently [25]. The radius  $R$  of the core particles was 45 nm, the average contour length  $L_c$  of the grafted chains was 165 nm and the grafting density (number of chains per unit area)  $\sigma = 0.14 \text{ nm}^{-2}$ . The entire number of charged groups in the polyelectrolyte layer was determined precisely by conductometric titration [25].

The gold and platinum nanoparticles were synthesized as described previously in Refs. [23–25]. In a typical experiment the bimetallic Au–Pt NPs were generated as follows: In the first step 120 mL of latex



(1.14 wt %) in pure water was placed in an ultrafiltration cell (NC 10 membrane filters, cellulosenitrate, Schleicher & Schuell, Germany) and 1 L of  $3.3 \times 10^{-4}$  M  $\text{HAuCl}_4$  (purchased from Aldrich:  $\text{HAuCl}_4 \cdot 3\text{H}_2\text{O}$ ) solution were passed through the cell. Subsequently, 500 mL of deionized water (Millipore, Milli-Q, A-10) were passed through the cell to remove free  $\text{AuCl}_4^-$  ions. The suspension attained a yellowish color indicating an exchange of counterions in the brush layer from  $\text{Cl}^-$  to  $\text{AuCl}_4^-$  ions. In the third step, 1 L of  $8 \times 10^{-5}$  M  $\text{H}_2\text{PtCl}_6$  (purchased from Aldrich:  $\text{H}_2\text{PtCl}_6 \cdot 6\text{H}_2\text{O}$ ) solution were passed through the cell. The color of the obtained dispersion changed to bluish/purple depending on the amount of gold respective platinum ions in the serum. For generation of bimetallic nanoparticles the dispersion was mixed slowly with 5 mL of a  $4 \times 10^{-4}$  M solution of  $\text{NaBH}_4$  through stirring under an atmosphere of nitrogen. The reduction of the  $\text{AuCl}_4^-$  and  $\text{PtCl}_6^{2-}$  ions could be followed easily by a change of color, dependent on the composition. After completion of the reaction the suspension was again placed in an ultrafiltration cell and a five-fold excess of deionized water was passed through the cell. The purification was monitored by measuring the conductivity of the serum. The content of gold and platinum in the composite system was determined by C, H, and N elemental analysis after burning off the organic material at  $950^\circ\text{C}$ , followed by a TEM-EDX analysis.

**Methods:** Cryogenic transmission electron microscopy (cryo-TEM) and transmission electron microscopy (TEM) were carried out using a LEO 9220 (200 kV) as described previously [28]. High-resolution TEM (HR-TEM) and EDX analysis were done using a Zeiss Libra 200 FE (200 kV) and a CM20 FEG with Noran Vantage system (Ge-detector) at 200 kV. The samples were prepared as follows: A drop of liquid was placed on a grid (Plano S 166-3). After drying on air for three minutes the rest of liquid was taken off by a filter paper. WAXS measurements were performed using a Bruker-AXS D8 Advance. Dynamic light scattering (DLS) was done using a Peters ALV 4000 light scattering goniometer and elemental analysis measurements were done using a Vario elemental EL III – CHN as described previously [25].

The catalytic activity was investigated as follows (for more details see Supporting Information): In a typical experiment 1 mmol of the alcohol (e.g., 172 mg  $\alpha$ -methyl-2-naphthalenemethanol) was added to a mixture of 8 mL of water and 3 mmol (414 mg) of  $\text{K}_2\text{CO}_3$ . At the end 1 mL of the catalyst solution was added to reach a loading of 0.0336 mol % of metal. The mixture was stirred for 24 h in an atmosphere of air at room temperature. After 24 h 0.4 mmol (68 mg, 91  $\mu\text{L}$ ) dodecane as internal standard was added. The products were extracted twice using 4 mL of diethylether. The combined organic layers were dried over  $\text{Na}_2\text{SO}_4$  and the conversion was checked by gas chromatography (GC). GC analyses were performed on an Agilent 6890N Gas Chromatograph equipped with a flame ionization detector (FID) and an Agilent 19091J-413 FS capillary column using dodecane as internal standard. Catalytic reactions were performed in glass tubes sealed with a PE cover. A small cannula through to cover allowed a continuous flow of air into the reaction vessel.

Received: September 25, 2007

Revised: November 22, 2007

Published online: April 21, 2008

- [1] A. Henglein, *Chem. Rev.* **1989**, 89, 1861.
- [2] A. P. Alivisatos, *Science* **1996**, 271, 933.
- [3] M. Haruta, M. Date, *Appl. Catal. A* **2001**, 222, 427.
- [4] M.-C. Daniel, D. Astruc, *Chem. Rev.* **2004**, 104, 293.
- [5] D. Astruc, F. Lu, R. Aranzaes, *Angew. Chem. Int. Ed.* **2005**, 44, 7852.
- [6] H. Miyamura, R. Matsubara, Y. Miyazaki, S. Kobayashi, *Angew. Chem. Int. Ed.* **2007**, 46, 4151.
- [7] C. L. Hill, *Advances in Oxygenated Processes*, Vol. 1, JAI Press, London **1988**.
- [8] M. Hundlucky, *Oxidations in Organic Chemistry*, ACS, Washington, DC, **1990**.
- [9] T. Mallat, A. Baiker, *Chem. Rev.* **2004**, 104, 3037.
- [10] R. A. Anderson, K. Griffin, P. Johnson, P. L. Alsteres, *Adv. Synth. Catal.* **2003**, 345, 517.
- [11] D. I. Enache, J. Edwards, P. Landon, B. Solsona-Espriu, A. F. Carley, A. A. Herzing, M. Watanabe, C. J. Kiely, D. W. Knight, G. J. Hutchings, *Science* **2006**, 311, 362.
- [12] Y. Lou, M. M. Maye, L. Han, J. Luo, C.-J. Zhong, *Chem. Commun.* **2001**, 473.
- [13] V. R. Stamenkovic, B. S. Mun, M. Arenz, K. J. J. Mayrhofer, C. A. Lucas, G. Wang, P. N. Ross, N. M. Markovic, *Nat. Mater.* **2007**, 6, 241.
- [14] J. Lou, M. M. Maye, V. Petkov, N. N. Kariuki, L. Wang, P. Njoki, D. Mott, Y. Lin, C.-J. Zhong, *Chem. Mater.* **2005**, 17, 3086.
- [15] Z. Hu, Y. Fan, Y. Chen, *Appl. Phys. A* **1999**, 68, 225.
- [16] G. De, C. N. R. Rao, *J. Mater. Chem.* **2005**, 15, 891.
- [17] P. N. Njoki, J. Luo, L. Wang, M. M. Maye, H. Quazar, C.-J. Zhong, *Langmuir* **2005**, 21, 1623.
- [18] D. Mott, J. Luo, A. Smith, P. N. Njoki, L. Wang, C.-J. Zhong, *Nanoscale Res. Lett.* **2007**, 2, 12.
- [19] G. C. Bond, *Platinum Met. Rev.* **2007**, 51(2), 63.
- [20] M. Brust, M. Walker, D. Bethell, D. J. Schiffrin, R. Wyman, *J. Chem. Soc. Chem. Commun.* **1994**, 801.
- [21] M. J. Hostetler, C.-J. Zhong, B. K. H. Yen, J. Anderegg, S. M. Gross, N. D. Evans, M. Porter, R. W. Murray, *J. Am. Chem. Soc.* **1998**, 120, 9396.
- [22] M. Ballauff, *Progr. Polym. Sci.* **2007**, 32, 1135.
- [23] Y. Mei, G. Sharma, Y. Lu, M. Drechsler, T. Irrgang, R. Kempe, M. Ballauff, *Langmuir* **2005**, 21, 12229.
- [24] G. Sharma, Y. Mei, Y. Lu, M. Ballauff, T. Irrgang, S. Proch, R. Kempe, *J. Catal.* **2007**, 246, 10.
- [25] M. Schrinner, F. Polzer, Y. Mei, Y. Lu, B. Haupt, M. Ballauff, A. Gödel, M. Drechsler, *Macromol. Chem. Phys.* **2007**, 208, 1542.
- [26] P. Pincus, *Macromolecules* **1991**, 24, 1912.
- [27] Y. M. A. Yamada, T. Arakawa, H. Hocke, Y. Uozumi, *Angew. Chem. Int. Ed.* **2007**, 46, 704.
- [28] A. Wittemann, M. Drechsler, Y. Talmon, M. Ballauff, *J. Am. Chem. Soc.* **2005**, 127, 9688.

Supplementary Material:

Stable bimetallic Gold-Platinum Nanoparticles  
Immobilized on Spherical Polyelectrolyte  
Brushes: Synthesis, Characterization and  
Application for the Oxidation of Alcohols

*Marc Schrinner, Yu Mei, Matthias Ballauff\**

Physikalische Chemie I, University of Bayreuth, 95440 Bayreuth, Germany

*Sebastian Proch, Rhett Kempe*

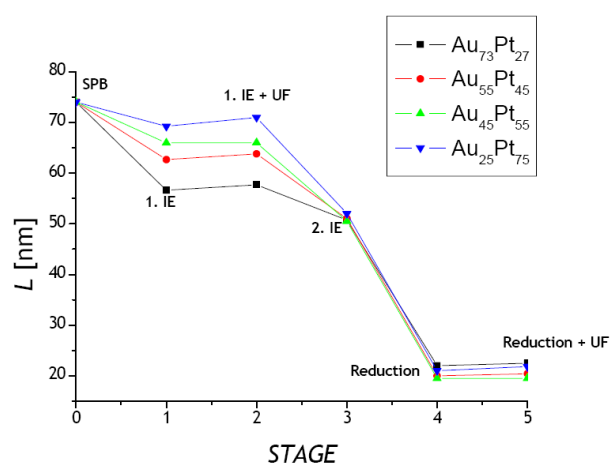
Anorganische Chemie II, University of Bayreuth, 95440 Bayreuth, Germany

*Nobuyoshi Miyajima*

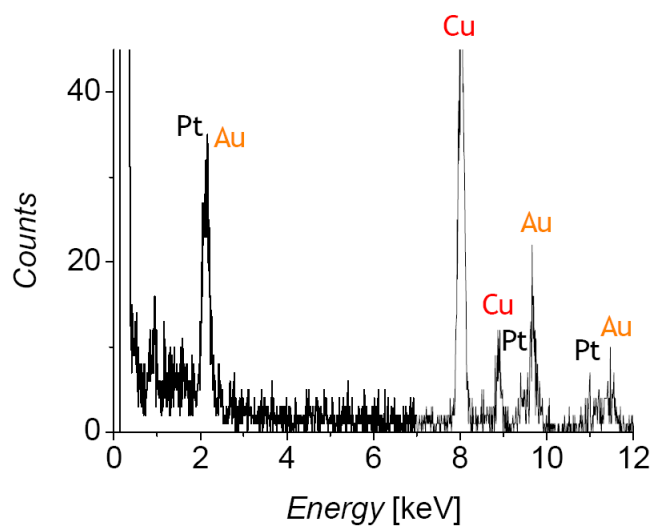
Bayerisches Geoinstitut, University of Bayreuth, 95440 Bayreuth, Germany

AUTHOR EMAIL ADDRESS ([Matthias.Ballauff@uni-bayreuth.de](mailto:Matthias.Ballauff@uni-bayreuth.de))

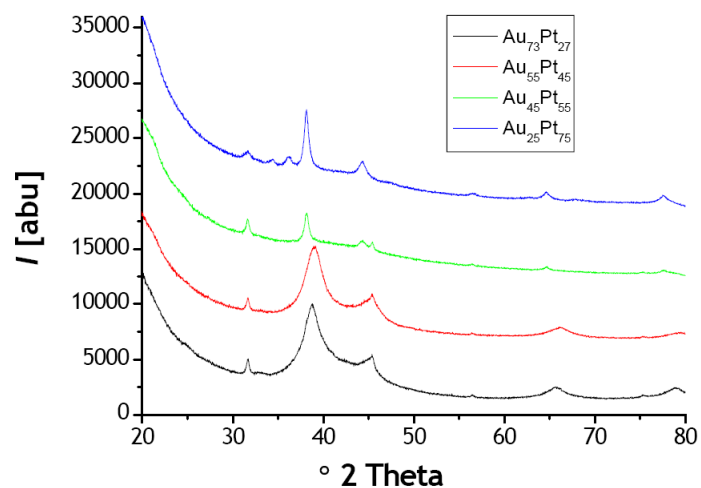
Figure S1	Ion exchange
Figure S2	EDX-spectra of a entire SPB/Au-Pt-NP composite particle
Figure S3	WAXS
Figure S4	Cryo-TEM of composite particles
Table SI	Catalyst solutions
Table SII	Recycling experiments



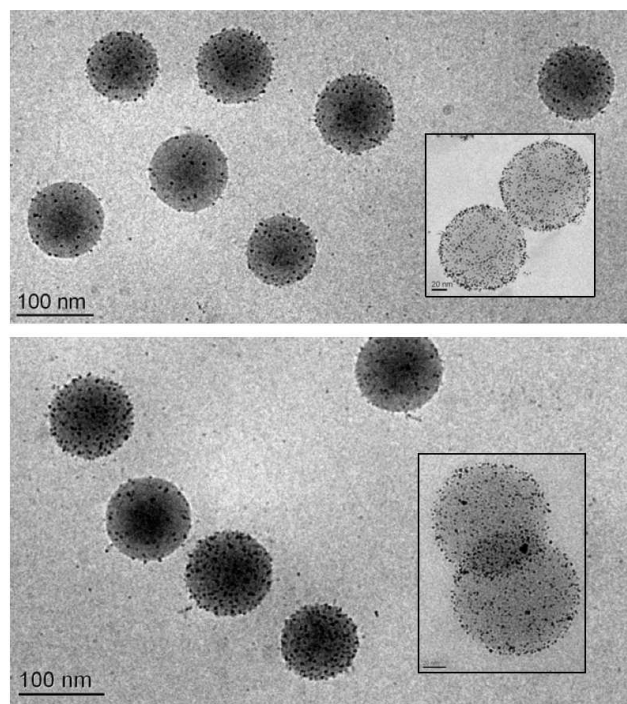
**Figure S1.** Decrease of the shell thickness  $L$  during ion exchange. Starting with the carrier particle SPB (Stage 0) the value of  $L$  is decreased by an increasing amount of  $[\text{AuCl}_4]^-$ -ions (Stage 1). The following ultrafiltration step (Stage 2) is followed by a slightly increasing  $L$ , indicating the change of ion strength. The introduction of  $[\text{PtCl}_6]^-$ -ions is followed again by an decreasing  $L$  (Stage 3). After reduction (Stage 4) and ultrafiltration (Stage 5)  $L$  becomes comparable for all composite systems.



**Figure S2.** EDX-spectra of an entire SPB/Au-Pt-NP composite ( $\text{Au}_{73}\text{Pt}_{27}$ ) particle. This spectra coincides with the spectra shown in Fig. 3 of the text. Hence, all alloy nanoparticles immobilized on a given carrier particle exhibit the same composition.



**Figure S3.** Wide-angle X-ray scattering intensities of the composite systems  $\text{Au}_{73}\text{Pt}_{27}$ ,  $\text{Au}_{55}\text{Pt}_{45}$ ,  $\text{Au}_{45}\text{Pt}_{55}$ ,  $\text{Au}_{25}\text{Pt}_{75}$  (from bottom to top).



**Figure S4.** Cryo-TEM image of a catalyst solution ( $\text{Au}_5\text{Pt}_{45}$ ) before (top) and after (bottom) use in a catalytic reaction. There is no change of the morphology of the composite particles. This underscores the stability of the composite system (see also Fig.S5).

**Table SI.** Solutions used for the determination of the catalytic activity

catalyst solution	solid content	metal content in solid content	Au content in metal content	Pt content in metal content
$\text{Au}_{73}\text{Pt}_{27}$	0.682 wt%	8.210 wt%	73 mol%	27 mol%
$\text{Au}_{55}\text{Pt}_{45}$	0.704 wt%	9.029 wt%	55 mol%	45 mol%
$\text{Au}_{45}\text{Pt}_{55}$	0.529 wt%	7.935 wt%	45 mol%	55 mol%
$\text{Au}_{25}\text{Pt}_{75}$	0.511 wt%	6.798 wt%	25 mol%	75 mol%

#### Oxygen consumption of benzyl alcohol oxidation (Au-NP)

A 600 ml steel autoclave was charged with 100 ml of water, 37.5 mmol (5.2 g)  $K_2CO_3$ , 12.5 mmol (1.3 ml) benzyl alcohol and 3.9 ml Au-NP.<sup>a</sup> A pressure of 1.1 bar pure  $O_2$  (pressure above atmospheric pressure) was used as oxidizing agent. The available gas volume amounts to 496 ml which corresponds to 42 mmol oxygen at the beginning of the reaction. At the stage of a complete conversion 35.75 mmol oxygen should be left, which corresponds to a pressure change of 0.3 bar (found: 0.35 bar after 16 h; conversion > 99 %).

#### Comparison o catalysts with different Pt content

In a typical experiment, 1 mmol benzyl alcohol (108 mg, 103  $\mu$ l) is added to a mixture of 8 ml of water and 3 mmol (414 mg) of  $K_2CO_3$ . At the end a catalyst solution in water is added to yield 0.0336 mol% metal ( a) 0.31 ml Au-NP; b) 0.12 ml  $Au_{73}Pt_{27}$ ; c) 0.1 ml  $Au_{55}Pt_{45}$ -NP; d) 0.16 ml  $Au_{45}Pt_{55}$ -NP; e) 0.19 ml  $Au_{25}Pt_{75}$ -NP; f) 1.16 ml Pt-NP; see table 1). The emulsion is stirred vigorously for 5 h in air at room temperature. After 5 h 0.4 mmol (68 mg, 91  $\mu$ l) dodecane as internal standard are added. The benzaldehyde is extracted twice using 4 ml of diethylether, the combined organic layers are dried over sodiumsulfate and the conversion is checked via GC.

#### Recycling experiments

In order to test the stability of the catalytic nanoparticles, several runs have been performed in which the catalysts have been re-used repeatedly. This has been done using the pure Pt-sample and the  $Au_{55}Pt_{45}$ -NP using 1 mmol of benzyl alcohol. After the reaction time of 24 h the products were removed by ether and new educts were added. This was repeated four times. Results are listed in the table. Stirring at 50°C leads to the precipitation of the gold containing samples within one hour.

**Table SII.** Recycling experiments.

sample	run 1	run 2	run 3	run 4
Pt-NP <sup>a</sup>	>99%	>99%	>99%	>99%
Au <sub>55</sub> Pt <sub>45</sub> -NP <sup>b</sup>	>99%	>99%	>99%	>99%

<sup>a</sup> 1.16 ml Pt-NP solution in water with a solid content of 0.520 wt% and a metal content of ca. 1.1 wt% Pt correspond to a catalyst loading of 0.0336 mol% Pt.

<sup>b</sup> 0.28 ml Au<sub>55</sub>Pt<sub>45</sub>-NP solution in water with a solid content of 0.339 wt% and a metal content of ca. 7 wt% Au/Pt (60 mol% Au and 40 mol% Pt) correspond to a catalyst loading of 0.0136 mol% Pt and 0.020 mol % Au (total 0.0336 mol %).





### 3.5 Single-Nanocrystals of Platinum Prepared by Partial Dissolution of Au-Pt-Nanoalloys

*Marc Schrinner<sup>a</sup>, Matthias Ballauff<sup>\*a</sup>, Yesahahu Talmon<sup>b</sup>, Yaron Kauffmann<sup>c</sup>,  
Jürgen Thun<sup>d</sup>, Michael Möller<sup>d</sup>, Josef Breu<sup>d</sup>*

<sup>a</sup> Physikalische Chemie I, <sup>d</sup> Anorganische Chemie I, University of Bayreuth, 95440 Bayreuth, Germany

<sup>b</sup> Department of Chemical Engineering, <sup>c</sup> Department of Materials Engineering, Israel-Institut of Technology, Technion, Haifa 32000, Israel

Published in *Science* 2009, 323, 617 – 620.

# Single-Nanocrystals of Platinum Prepared by Partial Dissolution of Au-Pt-Nanoalloys

*Marc Schrinner, Matthias Ballauff\**

Physikalische Chemie I, University of Bayreuth, 95440 Bayreuth, Germany

*Yeshayahu Talmon*

Department of Chemical Engineering, Technion-Israel Institute of Technology, Haifa 32000, Israel

*Yaron Kauffmann*

Department of Materials Engineering, Technion-Israel Institute of Technology, Haifa 3200, Israel

*Jürgen Thun, Michael Möller, Josef Breu*

Anorganische Chemie I, University of Bayreuth, 95440 Bayreuth, Germany

AUTHOR EMAIL ADDRESS (Matthias.Ballauff@uni-bayreuth.de)

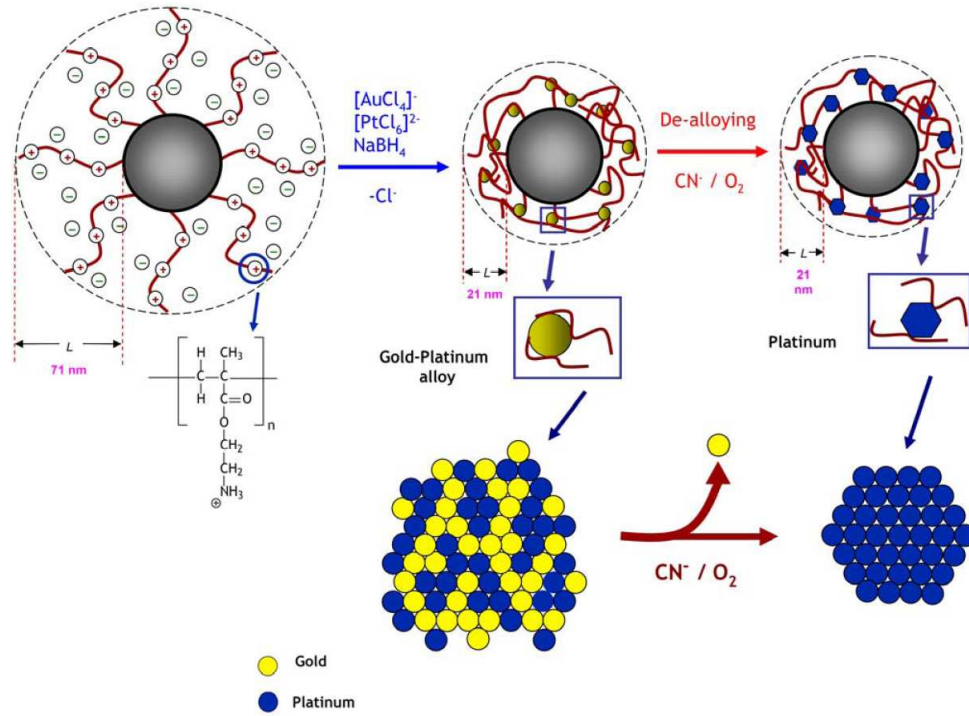
**October 1, 2008**

**ABSTRACT** We describe the preparation of perfect single nanocrystals of platinum with a size of 2 – 3 nm. These particles are generated and immobilized on spherical polyelectrolyte brushes consisting of a polystyrene core (diameter ca. 100 nm) onto which long chains of a cationic polyelectrolyte are affixed. In a first step a nanoalloy of gold and platinum is generated within the layer of cationic polyelectrolyte chains. Previous work demonstrated that the Au-Pt-nanoalloy generated in this way presents a true solid solution of gold and platinum atoms. In a second step the gold is slowly and selectively dissolved by cyanide ions in presence of oxygen. Cryo-transmission electron microscopy, wide-angle X-ray scattering and high-resolution transmission electron microscopy show that the resulting platinum nanoparticles are single-crystals with size of 2 to 3 nm only. The platinum nanoparticles are firmly embedded in the layer of polyelectrolyte chains bound to the surface of the core particles. Thus, the composite systems of the core particles and the platinum single nanocrystals exhibit an excellent colloidal stability. Moreover, they show high catalytic activity in hydrogenation reactions in the aqueous phase.

**KEYWORDS** nanocrystal, nanoalloy, spherical polyelectrolyte brushes, high-resolution TEM

Metallic nanoparticles of controlled size and shape have been of great interest recently for a number of possible applications in electronic or optical materials as well as in catalysis (1, 2, 3, 4, 5, 6, 7). In this way they have become one of the major basic building blocks of nanotechnology. By now the intense research devoted to metallic nanoparticles in the last years has clearly demonstrated that particle morphology plays a central role in catalysis. For instance, faceted platinum crystals have been found to exhibit higher catalytic activity than spherical particles (8, 9); the activity of the exposed facets may vary considerably (10, 11). The reactivity and selectivity of nanoparticles can therefore be tuned by controlling their morphology. In opposite to this, amorphous platinum nanoparticles have been found to exhibit a much reduced catalytic activity (12).

The prospect for a number of possible applications has led to a strong activity in this field in the last years. However, faceted nanocrystals with a well-developed shape and a narrow size distribution exhibit in general sizes typically in the range of 100 nm and more. Thus, Sun *et al.* could obtain well-defined gold and silver crystals with sizes on the order of 100 nm (4). Nanoprisms of silver with dimensions around 100 nm were prepared by Jin *et al.* by a photochemical conversion of silver spheres (3). Anisotropic silver nanoparticles of similar size have been synthesized by Liz-Marzan and coworkers through careful choice of a suitable surfactant (13). Platinum nanocrystals with high-index facets have been obtained recently by Tian and coworkers (6). Here again the typical sizes are ranging between 50 and 200 nm. Up to now, the only rather tedious route to faceted single crystals in the size range of a few nanometers is the synthesis of well defined clusters, e.g., Au<sub>55</sub>-cluster and a following heat treatment (14).



**Fig. 1.** Synthesis scheme of platinum nanocrystals by de-alloying of a Au-Pt-nanoalloy. The carrier particles are spherical polyelectrolyte brushes (SPB) that consist of a solid polystyrene (PS) core ( $R_H = 50$  nm) onto which cationic polyelectrolyte chains of 2-aminoethylmethacrylate (2-AEMH) are attached. In a first step the chloride counterions are exchanged against  $\text{AuCl}_4^-$ -ions; in a second step the rest of  $\text{Cl}^-$ -ions are exchanged against  $\text{PtCl}_6^{2-}$ -ions. The strong electrostatic interaction of the polyelectrolyte chains with their metal counterions leads to a virtually complete confinement of the ions (see the discussion of this point in ref. (22)). Bimetallic  $\text{Au}_{45}\text{Pt}_{55}$  nanoalloy particles are generated by reduction of the mixture of these ions by  $\text{NaBH}_4$  (21). The composition of the resulting nanoalloy can be adjusted very well by the ratio of the metal ions in the brush layer. In the final step cyanide-ions and oxygen are used to leach out the gold-atoms from the nanoalloy under very mild conditions. This procedure leads to faceted platinum nanocrystals with a size of few nanometers only. The platinum nanocrystals are firmly embedded in the surface layer of polyelectrolyte chains and the entire composite particles exhibit an excellent colloidal stability.

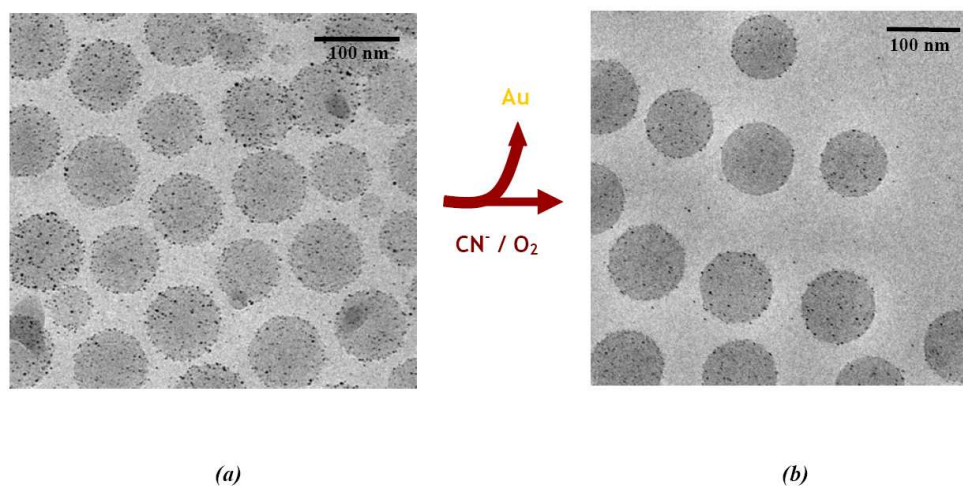
Platinum nanoparticles play a central role in recent research, because the growth of specific surfaces can be controlled by amphiphilic polymers or suitable surfactants (8, 15, 16, 17, 18). However, downsizing the platinum nanoparticles to a few nanometers is often accompanied by a broadening of the distribution, and partial loss of the control of the particle shape (5). The reduction of the metal ions and the generation of the nanoparticles seem to proceed very rapidly, leading to disordered structures and distorted crystal shapes. Thus, even amorphous platinum nanoparticles have been found recently (12). Summing up, it is fair to state that a direct synthesis of well-defined single nanocrystals of metals in the range of a few nanometers at room temperature has not been achieved yet.

In this communication we present a new and simple way for the synthesis of faceted, well-defined platinum single nanocrystals with a typical size of 2 - 3 nm only. As shown in Figure 1 the platinum nanocrystals are obtained by partial dissolution of nanoalloys of platinum and gold. In case of larger nanoalloy particles this procedure leads to sponge-like or hollow structures (19, 20). Here we find that the dissolution of the gold component of the nanoalloy leads to re-organization of the platinum atoms and the formation of well-defined, faceted nanocrystals. Fig. 1 displays the details in a schematic fashion. We start from a nanoalloy of gold and platinum generated on the surface of a spherical polyelectrolyte brush (SPB) as described recently (21). These particles consist of a solid core with colloidal dimensions (diameter: ca. 100 nm) onto which long charged polymer chains are grafted. These spherical polyelectrolyte brushes have been shown to be uniquely suited for the generation and immobilization of metallic nanoparticles in the aqueous phase (22, 23) for the following reasons: anionic complex ions of metals, like gold, silver, palladium or platinum, can be immobilized in the surface layer of cationic SPB. This confinement of these ions was attributed to the strong electrostatic interaction of the counterion with the highly charged macroion. The complex metal ions like  $\text{PtCl}_6^{2-}$  are thus localized solely in the layer of polyelectrolyte chains of the SPB, virtually no metal salt is dissolved into the aqueous phase. Subsequent reduction with  $\text{NaBH}_4$  under mild conditions leads to metallic nanoparticles, firmly embedded in a dense layer of polyelectrolyte chains. In the same way, particles of nano-alloys (24) can be synthesized and immobilized on the surface layer of spherical

polyelectrolyte brush particles. We demonstrated this by reduction of a mixture of the  $\text{AuCl}_4^-$  and  $\text{PtCl}_6^{2-}$  ions in the surface layer of a cationic SPB (21). High-resolution transmission electron microscopy (HR-TEM) has shown that the nanoalloy particles do not exhibit a core-shell structure (cf. the discussion of this point in (24)), but present homogeneous, true solid solutions (21). The composition of the metals can be varied continuously without disturbing the structure of the particles that consist of a random mixture of gold and platinum (21). Moreover, the final composition is within narrow limits determined by the ratio of the metal ions introduced into the brush layer before (21). A point that is important for all possible applications as e.g. catalysis in the aqueous phase is the excellent colloidal stability of the composite particles that consist of the carriers and the metallic nanoparticles. This is due the strong interaction of the alloy nanoparticles with the polyelectrolyte chains affixed to the surface of the carrier particle. As depicted in Fig. 1, the cationic polymer chains are interwoven with the nanoparticles and form a dense mesh on the surface of the core particles. This could be shown by careful measurements of the hydrodynamic radius  $R_H$  by dynamic light scattering (see supporting information) (25). The thickness  $L$  of the surface layer is given by  $L = R_H - R$  where  $R$  denotes the radius of the cores. As will be shown further below, the colloidal stability of the composites allows us to transform the nanoparticles while keeping them on the surface of the core particles.

We prepared composite particles containing Au-Pt-nanoalloys with the composition  $\text{Au}_{45}\text{Pt}_{55}$  as shown by elemental analysis. Partial dissolution of these nanoalloy particles then leads to pure platinum single nanocrystals. As shown in Fig. 1 the gold atoms are slowly dissolved by a treatment of the particles with cyanide-ions in presence of oxygen. In a typical experiment the crystalline platinum particles were generated as follows: The gold atoms of the bimetallic gold-platinum  $\text{Au}_{45}\text{Pt}_{55}$  nanoparticles were dissolved by drop-wise addition of 4 mL of a  $1.9 \times 10^{-5}$  M NaCN solution to 13 mL of a gold-platinum-SPB suspension (0.04 wt.-%) at room temperature under air by vigorous stirring. The high dilution of the cyanide ions turned out to be crucial to avoid coagulation or complete dissolution of the nanoparticles. Air was bubbled slowly through the solution in order to achieve complete removal of

the gold atoms. After 3 hours the dispersion turned blue, indicating the formation of pure platinum nanoparticles (25).

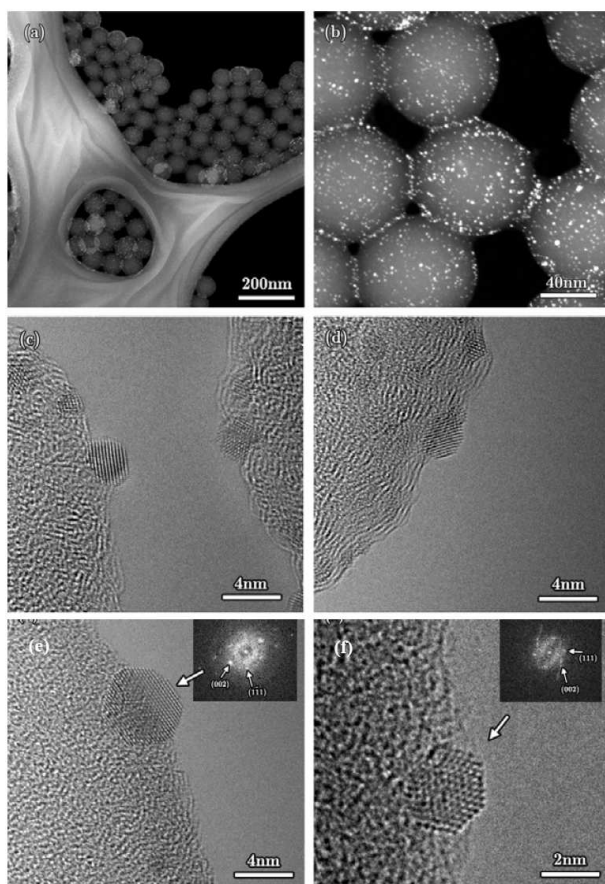


**Fig. 2.** (a) Cryo-TEM micrographs of the Au-Pt-nanoalloy particles (composition: Au<sub>45</sub>Pt<sub>55</sub>) generated on the surface of the spherical polyelectrolyte brushes. (b) Composite particles after complete removal of the gold atoms from the Au-Pt-nanoalloy by a mixture of CN<sup>-</sup>-ions and O<sub>2</sub>.

We find that the de-alloying of the Au-Pt-nanoalloy proceeds surprisingly smoothly. Fig. 2 shows micrographs of the composite particles before and after the leaching process. These micrographs were obtained by cryogenic transmission electron microscopy (cryo-TEM) that allows us to analyze the particles in their native state (26). Thus, a small drop of the suspension of the composite particles is shock-frozen and analyzed by transmission electron microscopy. The platinum nanocrystals can be seen in Fig. 2b as black dots distributed over the SPB. Both the nanoalloy particles as well as the platinum



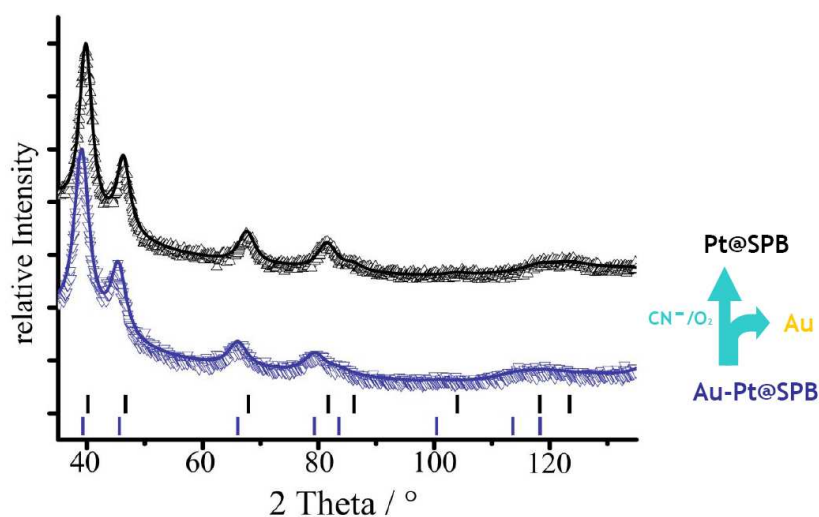
nanoparticles are distributed more or less uniformly over the carrier particles. The metal nanoparticles have a rather narrow size distribution which is preserved during the leaching process.



**Fig. 3.** (a)-(b) High angle annular dark field scanning transmission electron microscopy (HAADF-STEM) micrographs of the platinum nanoparticles (bright spots) embedded and uniformly dispersed on a surface layer of the spherical polyelectrolyte; (c) HR-TEM micrograph of nano-particles on the surface of two adjacent carrier particles; (d) HR-TEM micrograph of several crystalline nanoparticles; (e)-(f) HR-TEM micrographs of two different single crystalline platinum nanoparticles of sizes 4.6 nm and 2.8 nm, respectively, showing well defined facets. All micrographs were acquired at 300 keV.

The formation of the cyanide complex of gold atoms is very selective (27). Hence, only gold atoms of bimetallic Au-Pt-nanoalloy are leached out. Energy-dispersive X-ray spectroscopy (EDX) (see Fig. S1 and S2 of the supplementary material) demonstrates indeed that the metal nanoparticles resulting from de-alloying of nanoparticles consist only of platinum. No traces of gold could be detected. Thus, the selective dissolution of Au from the Au-Pt-nanoalloy leads to platinum nanoparticles still embedded on the surface of the SPB-carrier particles. It is important to note, that the colloidal stability of the composite particles is not lost during the reaction with the cyanide ions, nor is any coagulation of the nanoparticles on the surface of the carrier particles observed during this process. Thus, the composite particles consisting of the SPB and the metalnanoparticles present a very stable system that can be used as catalyst, as further discussed below (21, 22, 28). However, the entire process depends crucially on the conditions under which the de-alloying takes place. Rapid addition or high concentrations of the cyanide ions lead to coagulation and coarsening of the metal nanoparticles on the surface.

The structure of the resulting platinum nanoparticles was analyzed by combining high angle annular dark field scanning transmission electron microscopy (HAADF-STEM) and high resolution TEM (HR-TEM) with electron diffraction and wide-angle X-ray scattering (WAXS). Fig. 3a shows a low-magnification HAADF-STEM micrograph of the polystyrene spheres on the supporting holey carbon film. Fig. 3b is a higher magnification, of the same area which shows the uniform distribution of the platinum nanoparticles on the polystyrene spheres. In order to avoid any disturbance of this analysis by the core particles, only nanoparticles sitting on the periphery of the carrier spheres were analyzed by HR-TEM (see Figure 3c – 3f). HR-TEM demonstrates that the platinum nanoparticles are single crystals indeed. All platinum particles observed were crystalline and no grain boundaries were observed inside the particles. In several cases the facets can be indexed because the nanocrystals are aligned by chance. For instance, in Fig. 3e and 3f the electron diffraction shows directly the hexagonal symmetry of the cubic crystal.

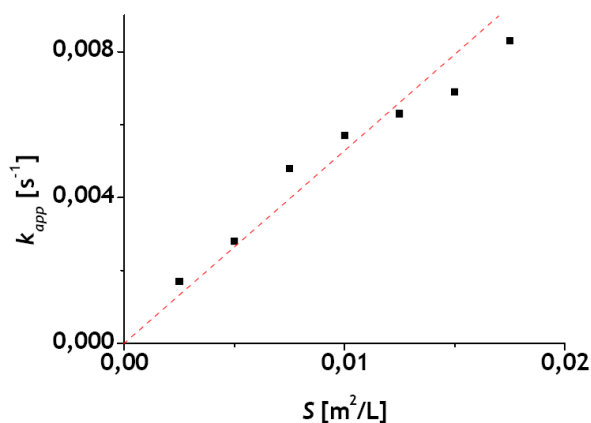


**Fig. 4.** Wide-angle X-ray scattering (WAXS)-diagrams of the Au<sub>45</sub>Pt<sub>55</sub>-nanoalloy (blue) and the platinum single crystals (black). Shown are the observed patterns (diamonds) and the best Rietveld-fit profiles (solid lines). Average real crystallite sizes were extracted from the line broadening of the peaks applying Rietveld analysis. The tick marks indicate the positions of the Bragg reflections of the Au<sub>45</sub>Pt<sub>55</sub>-nanoalloy (blue) and the platinum single crystals (black), respectively. Please note the slight shift of the diffraction peaks to higher angles which reflects the expected decrease of the unit cell parameter when going from the Au<sub>45</sub>Pt<sub>55</sub>-nanoalloy to pure platinum single crystals by selective extraction of gold atoms.

The lattice spacing derived from the (200) reflection as seen in the electron diffraction ( $d_{200} = 0.20$  nm) is in good agreement with the bulk value ( $d_{200} = 0.196$  nm; spacing: 0.392 nm; Ref. (29) (30)). The overall size of the platinum nanocrystals lies within the range estimated from the volume contraction due to the leaching of the Au-ions. All results hence demonstrate that the crystals of the Au-Pt nanoalloy are converted to the platinum single crystals individually; no coagulation or exchange between different nanoalloy particles takes place. Some of the particles moved under the intense electron beam and rolled on the surface of the polystyrene spheres, but their shape remained stable (no

melting was observed). Doubts may be raised whether the high crystallinity observed by HR-TEM could have been induced by the electron beam through local heating and subsequent crystallization. This problem can be solved by wide-angle X-ray scattering applied to powders of the dried composite particles. Fig. 4 displays the X-ray diffractograms (XRD) of the entire composite particles before and after partial dissolution of the Au-Pt-nanoalloy. The only preparatory step involved in this analysis is the drying of the composite particles at room temperature. All XRD-peaks observed can be indexed with a fcc unit cell demonstrating that both, the starting Au-Pt-nanoalloy and the resulting platinum single crystals represent single phases. The height and the breadth of these peaks can be analyzed to yield information on the average particle size (Rietveld analysis). While the conventional Scherrer analysis extracts only the crystal size from line broadening of a peak, the Rietveld analysis uses the full diffraction pattern. Moreover, it takes into account the lattice strain effects on line-broadening which yields more realistic values of the crystal size. Hence, the size of the crystallites derived from this analysis can be directly compared to the ones obtained by direct observation in the HR-TEM. Details of the Rietveld analysis are given in the supplementary material. First of all, a lattice parameter of  $0.40102 (\pm 0.0000014)$  nm is obtained for the starting material ( $\text{Au}_{45}\text{Pt}_{55}$ ). This lattice spacing agrees very well with the value expected from Vegard's law, that is, the lattice parameter of the nano-alloy can be obtained by linear interpolation of the lattice parameters of Au and Pt (see the discussion of this point in Ref. (21)). This shows that both Au and Pt are homogeneously mixed in the alloy at the level of the unit cell. The nanoalloy thus represents a true solid solution. After complete removal of the gold atoms, the lattice parameter shrinks to  $0.39146 (\pm 0.00009)$  nm as expected. This value is in excellent agreement with the known lattice parameter of pure platinum ( $0.392$  nm; (29)). The average crystallite sizes as extracted from the Rietveld analysis were  $7.01(3)$  nm for the  $\text{Au}_{45}\text{Pt}_{55}$ -nanoalloy and  $3.80(4)$  nm for the resulting platinum single crystals, respectively. These values agree very well with crystal sizes as observed by HR-TEM which confirms that particles shown in Fig. 3 are representative for the whole sample. From these results we conclude that a possible dissolution followed by re-crystallization of the platinum nanoparticles can be safely dismissed. Thus, all methods applied

here lead unambiguously to the conclusion that Au-Pt-nanoalloys can be converted into single crystals of Pt by selective leaching of the Au-atoms. Considering that the nanoalloy particles contain only 750 - 900 atoms in total, the present process represents a novel type of a well-defined chemical manipulation of nanocrystals.



**Fig. 5.** Catalytic activity of the Pt-nanocrystals. The normalized rate constant  $k_1$  (see equ.(1)) obtained for the catalytic reduction of p-nitrophenol to p-amino-phenol is plotted against the specific surface  $S$  of the platinum single nanocrystals in the solution.  $S$  is the total surface of all particles per unit volume.

As a final point we discuss the catalytic activity of the platinum nanocrystals affixed to the surface of the spherical polyelectrolyte brushes. Previous work (22, 31) demonstrated that the catalytic reduction of p-nitrophenol to p-aminophenol can be used for the analysis of the catalytic activity of nanoparticles. We assumed that reduction rates were independent of the concentration of sodium borohydride since it was in excess compared to p-nitrophenol. Moreover, the apparent rate constant  $k_{app}$  was found to be proportional to the surface  $S$  of the metal nanoparticles present in the system (28):

$$-\frac{dc_t}{dt} = k_{app}c_t = k_1Sc_t \quad (1)$$

where  $c_t$  is concentration of *p*-nitrophenol at time  $t$ ,  $k_1$  is the rate constant normalized to  $S$ , the surface area of platinum nanoparticles normalized to the unit volume of the system. Therefore the rate constant  $k_1$  has been plotted against the specific surface  $S$  of the metal nanoparticles in the systems (see Figure 5; (31)). Fig. 5 shows that the platinum single nanocrystals exhibit a high catalytic activity leading to turnover numbers of 1580. This value is among the highest turnover number measured so far (22). Hence, the composite particles consisting of the spherical polyelectrolyte brushes and the platinum nanoparticles present a system with high colloidal stability that may be used for catalysis in an aqueous environment. It should be noted that the polyelectrolyte layer can be dissolved to yield free nanocrystals of Pt. Thus, the method communicated here presents a general access to the smallest faceted single crystals of platinum known so far. Further tests of the catalytic properties of these crystals are under way.

ACKNOWLEDGMENT Financial support by the Deutsche Forschungsgemeinschaft, SFB 481, Bayreuth, by the BASF SE, and by the Fonds der Chemischen Industrie is gratefully acknowledged. Marc Schrinner thanks the Minerva Foundation, the German Academic Exchange Service (DAAD), and the Technion Russell Berrie Nanotechnology Institute (RBNI) for the support during his stay at the Technion in Haifa. Cryo-TEM was performed at the Hannah and Georeg Krumholz Laboratory for Electron Microscopy of Soft Matter, part of the Technion Project on Complex Liquids, Microstructure and Macromolecules.

#### REFERENCES

- 
- <sup>1</sup> C. Burda, X. Chen, R. Narayanan, M. A. El-Sayed, *Chem. Rev.* **105**, 1025 (2005).

- 
- <sup>2</sup> S. K. Gosh, T. Pal, *Chem. Rev.* **107**, 4797 (2007).
- <sup>3</sup> R. Jin, Y. W. Cao, C. A. Mirkin, K. L. Kelly, G. C. Schatz, J. G. Zheng, *Science* **294**, 1901 (2001).
- <sup>4</sup> Y. Sun, Y. Xia, *Science* **298**, 2176 (2002).
- <sup>5</sup> R. Narayanan, M. A. El-Sayed, *J. Am. Chem. Soc.* **126**, 7194 (2004).
- <sup>6</sup> N. Tian, Z.-Y. Zhou, S.-G. Sun, Y. Ding, Z. L. Wang, *Science* **316**, 732 (2007).
- <sup>7</sup> S. C. Warren, L. C. Messina, L. S. Slaughter, M. Kamperman, Q. Zhou, S. M. Gruner, F. J. DiSalvo, U. Wiesner, *Science* **320**, 1748 (2008).
- <sup>8</sup> T. S. Ahmadi, Z. L. Wang, T. C. Green, A. Henglein, M. A. El-Sayed, *Science* **272**, 1924 (1996).
- <sup>9</sup> R. Narayanan, M. A. El-Sayed, *J. Am. Chem. Soc.* **126**, 7194 (2004).
- <sup>10</sup> R. Naryanan, M. A. El-Sayed, *J. Phys. Chem. B* **107**, 12416 (2003).
- <sup>11</sup> R. Narayanan, M. A. El-Sayed, *Nano Lett.* **4**, 1343 (2004).
- <sup>12</sup> Y. Sun, L. Zhuang, J. Lu, X. Hong, P. Liu, *J. Am. Chem. Soc.* **129**, 15465 (2007).
- <sup>13</sup> I. Pastoriza-Santos, L. Liz-Marzan, *Nano Lett.* **2**, 903 (2002).
- <sup>14</sup> M. Turner, V. B. Golovko, O. P. H. Vaughan, P. Abdulkin, A. Berenguer-Murcia, M. S. Tikhov, B. F. G. Johnson, R. Lambert, *Nature* **454**, 981 (2008).
- <sup>15</sup> H. Lee, S. E. Habas, S. Kweskin, D. Butcher, G. A. Somoraj, P. Yang, *Angew. Chem. Intl. Ed.* **45**, 7824 (2006).
- <sup>16</sup> S. Kinge, H. Bönemann, *Appl. Organomett. Chem.* **20**, 784 (2006).
- <sup>17</sup> R. D. Tilley, J. Ren, *Small* **9**, 1508 (2007).

- 
- <sup>18</sup> E. Ramirez, L. Eradés, K. Philippot, P. Lecante, B. Chaudret, *Adv. Funct. Mat.* **17**, 2219 (2007).
- <sup>19</sup> S. Guo, Y. Fang, S. Dong, E. Wang, *J. Phys. Chem. C* **111**, 17104 (2007).
- <sup>20</sup> J. Snyder, P. Asanithi, A. B. Dalton, J. Erlebacher, *Adv. Mater.* published online, (2008).
- <sup>21</sup> M. Schrunner, S. Proch, Y. Mei, R. Kempe, N. Miyajima, M. Ballauff, *Adv. Mater.* **20**, 1928 (2008).
- <sup>22</sup> M. Ballauff, *Progr. Polym. Sci.* **32**, 1135 (2007).
- <sup>23</sup> Y. Lu, Y. Mei, M. Schrunner, M. Ballauff, M. W. Möller, J. Breu, *J. Phys. Chem. C* **111**, 7676 (2007).
- <sup>24</sup> R. Ferrando, J. Jellinek, R. L. Johnston, *Chem. Rev.* **108**, 845 (2008).
- <sup>25</sup> M. Schrunner, F. Polzer, Y. Mei, Y. Lu, B. Haupt, M. Ballauff, A. Gödel, M. Drechsler, *Macromol. Chem. Phys.* **208**, 1542 (2007).
- <sup>26</sup> Li, Z., Kesselman, E., Talmon, Y., Hillmyer, M.A., and Lodge, T.P. *Science* **306**, 98 (2004).
- <sup>27</sup> J. E. Huheey, *Inorganic Chemistry: principles of structure and reactivity*, 5.ed., Pearson/Addison-Wesley, Boston (2004).
- <sup>28</sup> Y. Mei, G. Sharma, Y. Lu, M. Drechsler, T. Irrgang, R. Kempe, M. Ballauff, *Langmuir* **21**, 12229 (2005).
- <sup>29</sup> D. Brooksbank, K. W. Andrews, *J. Iron Steel Ins.* **206**, 595 (1968).
- <sup>30</sup> T. Swanson, *Natl. Bur. Stand. (U.S.), Circ.* **31**, 539 (1953).
- <sup>31</sup> Y. Mei, Y. Lu, F. Polzer, M. Ballauff, F. Polzer, *Chem. Mater.* **19**, 1062 (2007).



# Single-Nanocrystals of Platinum Prepared by Partial Dissolution of Au-Pt-Nanoalloys

*Marc Schrinner, Matthias Ballauff\**

Physikalische Chemie I, University of Bayreuth, 95440 Bayreuth, Germany

*Yeshayahu Talmon*

Department of Chemical Engineering, Technion,-Israel Institute of Technology, Haifa 32000,  
Israel

*Yaron Kauffmann*

Department of Materials Engineering, Technion,-Israel Institute of Technology, Haifa 3200,  
Israel

*Jürgen Thun, Michael Möller, Josef Breu*

Anorganische Chemie I, University of Bayreuth, 95440 Bayreuth, Germany

*Supplementary Material*

*Materials:* Cationic spherical polyelectrolyte brushes carrying chains of poly(2-aminoethylmethacrylate hydrochloride) (PAEMH) were synthesized as described recently [give ref.?]. The radius,  $R$ , of the core particles was 45 nm, the average contour length,  $L_c$ , of the grafted chains was 165 nm, and the grafting density (number of chains per unit area)  $\sigma = 0.14 \text{ nm}^{-2}$ . The entire number of charged groups in the polyelectrolyte layer was determined precisely by conductometric titration (1).

The bimetallic gold-platinum nano-particles on spherical polyelectrolyte brushes were synthesized as described previously in ref (2). In a typical experiment the crystalline platinum particles were generated as follows: The gold atoms of the bimetallic gold-platinum nano-particles were dissolved by drop-wise addition of 4 mL of a  $1.9 \times 10^{-5} \text{ M}$  NaCN solution to 13 mL of a gold-platinum-SPB suspension (0.04 wt.-%) at room temperature under air by vigorous stirring. The solution was flushed slowly with air to achieve full oxidation of the gold atoms. After 3 h the dispersion had a steel blue colour like the latex (Pt/SPB composite system) with pure Pt nano-particles. The complexation of gold atoms by  $\text{CN}^-$ -ions is selective for gold and no platinum atoms dissolved by this method (3).

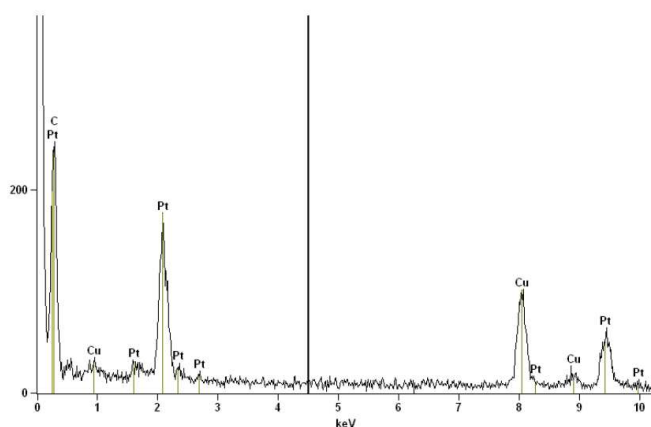
After completion of the reaction the suspension was placed in an ultrafiltration cell again, and a two-fold excess of de-ionized water was passed through the cell. The purification was monitored by measuring the conductivity of the serum. The content of platinum in the composite system was determined by C, H, and N elemental analysis after burning off the organic material at  $950^\circ\text{C}$ , followed by a TEM-EDX analysis.

*Methods:* Cryogenic transmission electron microscopy (cryo-TEM) was carried out by an FEI T12 (120 kV) and lacey carbon on copper grids (Science Services LC305-Cu [we used the Pelco ones]), as described previously (4). High-resolution TEM (HR-TEM) imaging and chemical analysis were done using a  $\text{C}_s$  corrected FEI Titan 80-300 S/TEM operated at 300 kV with a point-to-point resolution below  $1\text{\AA}$ , equipped with an EDX detector (EDAX Inc.). All samples examined in the HR-TEM were placed on lacey carbon copper grids (Science

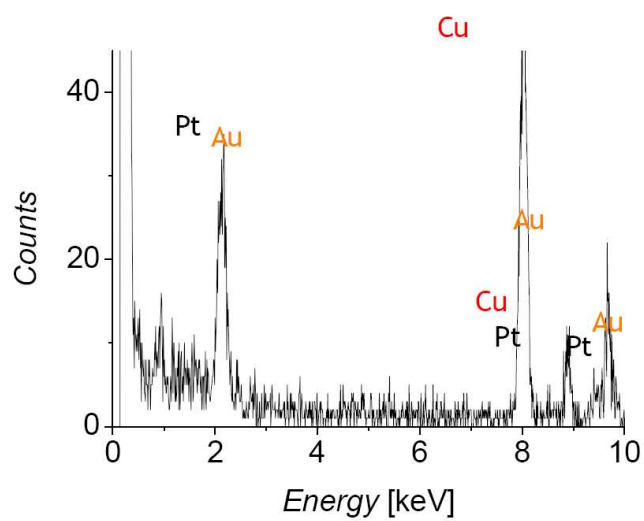
S2

Services LC305-Cu). After drying in air for three minutes the rest of liquid was blotted by a filter paper. After these procedures the grid was dried in vacuum for 24 h, and the samples were plasma cleaned (Model 1020 plasma cleaner, Fischione Instruments, Inc.) for 30 seconds to remove residuals from the solution and to avoid any contamination under the beam during imaging and EDX analysis. PXR-diffractograms of the finely ground, dry samples on zero-background sample holders were collected in Bragg-Brentano-geometry on a Panalytical XPERT-PRO diffractometer with a X'Celerator Scientific detector using Cu -  $K_{\alpha 1}$  radiation (40 kV, 40 mA). Dynamic light scattering (DLS) experiments and elemental analysis were done as described previously in ref. (5).

*Catalytic Activity:* As a model reaction we chose the reduction of *p*-nitrophenol by  $\text{NaBH}_4$  to *p*-aminophenol, as described previously (6). In a typical experiment a given amount of SPB/Pt-composite nanoparticles were added to a *p*-nitrophenol (0.1 mmol/L) solution. After mixing these solutions, a given amount of sodium borohydride (10 mmol/L) was added to start the reduction. The kinetic process of the reduction was monitored by measuring the extinction of the solution at 400 nm as a function of time. To study the effect of oxygen dissolved in water on catalytic kinetics, nitrogen was used to purge water for 30 minutes. At the end,  $\text{NaBH}_4$  was added directly in the cuvette to start the reaction.



**Figure S1.** EDX-spectra of an entire SPB/Pt-NP composite particle. The Cu peaks are from the grid.



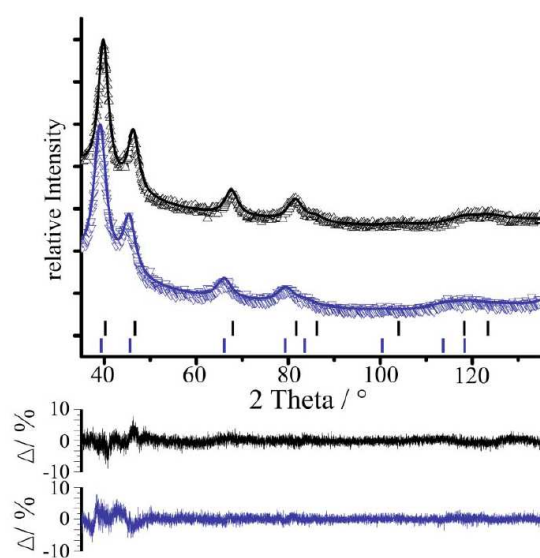
**Figure S2.** EDX-spectra of an entire SPB/Au-Pt-NP composite ( $\text{Au}_{45}\text{Pt}_{55}$ ) particle. The Cu-peak is from the grid.

Rietveld refinements were performed applying the program TOPAS (7) for both, the starting material and the resulting Platinum nanoparticles. A good fit of the experimental diffraction traces was obtained as indicated by the small difference curves (see Fig. S3) and low R-values (see Tab. S1).

Size-strain-line broadening analysis can be performed with different procedures (8). The results of a recently conducted round-robin showed that all techniques used give similar results. We choose to extract the crystal sizes from Rietveld refinements. As suggested by the round robin, the instrument parameters were determined using LaB<sub>6</sub> and both, Lorentzian and Gaussian contributions to the size-broadening-term were refined. More details and results of the Rietveld refinement are given in Table S1.

**Table S1.** Crystallographic details of the platinum nanoparticle and the Gold-Platinum alloy.

Parameter	Platinum	Gold-Platinum alloy
$a$ [Å]	3.9146(9)	4.0102(14)
$V$ [Å <sup>3</sup> ]	59.98(4)	64.49(7)
space group	$Fm\bar{3}m$	$Fm\bar{3}m$
$R_{\text{Bragg}}$ [%]	1.44	0.65
$R_{\text{wp}}$ [%]	5.23	5.53
zero point	-0.0603	0.2226
strain [%]	1.80(8)	1.74(16)
crystal size [nm]	3.80(4)	7.01(3)



**Figure S3.** Scattered X-ray intensities as a function of diffraction angle showing the good fit between the observed and calculated data based upon a Rietveld refinement. In the top, the observed pattern (diamonds) and the best Rietveld-fit profile (solid line) for Au<sub>45</sub>Pt<sub>55</sub>-nano-alloy (blue) and the Pt-single crystals (black) are shown. The upper and the lower tick marks indicate the positions of the Bragg reflections as obtained in the Rietveld refinement. In the bottom the resulting difference curves are shown indicating the good quality of the fit.

1 M. Schrunner, F. Polzer, Y. Mei, Y. Lu, B. Haupt, M. Ballauff, A. Gödel, M. Drechsler, *Macromol. Chem. Phys.* **208**, 1542 (2007).

2 M. Schrunner, S. Proch, Y. Mei, R. Kempe, N. Miyajima, M. Ballauff, *Adv. Mater.* **20**, 1928 (2008).

3 J. E. Huheey, *Inorganic Chemistry: principles of structure and reactivity*, 5.ed., Pearson/Addison-Wesley, Boston (2004).

4 H. Cui, T.K. Hodgdon, E. W. Kaler, L. Abezgauz, D. Danino, M. Lubovsky, Y. Talmon, D. J. Pochan, *Soft Matter* **3**, 945 (2007).

---

5 M. Schrunner, S. Proch, Y. Mei, R. Kempe, N. Miyajima, M. Ballauff, *Adv. Mater.* **20**, 1928 (2008).

6 Y. Mei, Y. Lu, F. Polzer, M. Ballauff, F. Polzer, *Chem. Mater.* **19**, 1062 (2007).

7 A. A. Coelho, TOPAS Users's Manual, Version 3.1 (Bruker AXS GmbH, Karlsruhe, Germany, 2003).

8 D. Balzar et al., *J. Appl. Cryst.* **37**, 911-924 (2004).





### 3.6 Nanoalloys as Efficient “Green” Catalysts for the Epoxidation of Alkenes by Molecular Oxygen

*Marc Schrunner<sup>a</sup>, Matthias Ballauff<sup>\*a</sup>, Salem Deeb<sup>b</sup>, Sebastian Proch<sup>b</sup>, Rhett Kempe<sup>b</sup>, Yaron Kauffmann<sup>c</sup>, Jürgen Thun<sup>d</sup>, Josef Breu<sup>d</sup>*

<sup>a</sup> Physikalische Chemie I, <sup>b</sup> Anorganische Chemie II, <sup>d</sup> Anorganische Chemie I, University of Bayreuth, 95440 Bayreuth, Germany

<sup>c</sup> Department of Chemical Engineering, <sup>c</sup> Department of Materials Engineering, Israel-Institut of Tecnology, Technion, Haifa 32000, Israel

***To be submitted 2008.***

## Nanoalloys as efficient “green” catalysts for the epoxidation of alkenes by molecular oxygen

*Marc Schrinner<sup>a</sup>, Matthias Ballauff<sup>e</sup>*

*Salem Deeb<sup>b</sup>, Sebastian Proch<sup>b</sup>, Rhett Kempe<sup>b</sup>*

*Yaron Kauffmann<sup>c</sup>*

*Jürgen Thun<sup>d</sup>, Josef Breu<sup>d</sup>*

a) Lehrstuhl für Physikalische Chemie I, Universität Bayreuth, Universitätsstraße 30,  
D-95440 Bayreuth (Germany)

b) Lehrstuhl für Anorganische Chemie II, Universität Bayreuth, Universitätsstraße 30,  
D-95440 Bayreuth (Germany)

c) Department of Materials Engineering, Israel Institute of Technology, Technion,  
Haifa 32000 (Israel)

d) Lehrstuhl für Anorganische Chemie I, Universität Bayreuth, Universitätsstraße 30,  
D-95440 Bayreuth (Germany)

*Date: October 8<sup>th</sup> 2008*

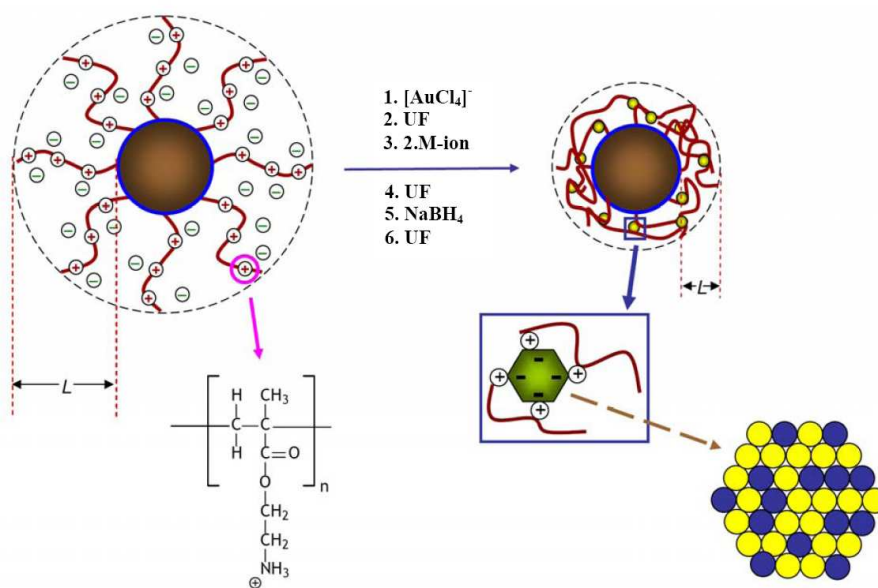
Since antiquity, alloys of various metals have been employed, because these materials may display properties that are superior to the ones of the pure components.<sup>1</sup> This synergistic effect is not only seen for mechanical properties, but also in catalysis. Recent work has demonstrated that nano-alloys, that is, nanoparticles consisting of two metals present highly active catalysts.<sup>2</sup> Thus, homogeneous nano-alloys from gold and platinum have been shown to be stable catalysts for oxidation reactions in an aqueous environment by oxygen.<sup>3</sup> Here we show that homogeneous nano-alloys from gold with iridium, rhodium, and ruthenium are highly selective catalysts for the epoxidation of alkenes by molecular oxygen. The particles of the nano-alloy are shown to present homogeneous mixtures of the respective metals that have miscibility gaps in bulk. We find that the nano-alloys exhibit the maximum catalytic activity at compositions around 50 mol-%. Our observations suggest that nano-alloys present a viable route to catalysts for “green” epoxidation reactions under very mild conditions.

Oxidation reactions are among the most important chemical reactions. Thus, life is merely possible via controlled reactions involving dioxygen from the air that lead to well-defined products. Industrial oxidation processes are often much less selective and require expensive intermediates. The use of molecular oxygen in an aqueous environment, which resembles the reaction pathway of enzymes, would lead to a “green” and sustainable chemistry. Oxidation products of alkenes as e.g. epoxides, ketones, aldehydes and alcohols are highly important starting materials for many materials of our everyday life like plastics, detergents, dyes, cosmetics and food additives. Epoxides are especially important in that they can be transformed into a multitude of different compounds via regio- and stereoselective ring-opening reactions.<sup>4,5</sup> Since Haruta’s discovery of unexpectedly high activity of gold clusters in the oxidation of CO in 1989<sup>6</sup> the application of gold catalysts in organic transformation reactions is increasing rapidly.<sup>7</sup> As an example, propene can be oxidized directly in the gas phase applying goldparticles immobilized on titania by a hydrogen/oxygen mixture yielding propylene oxide.<sup>8,9,10,11</sup> The epoxides of other cyclic and acyclic alkenes can also be synthesized by means of heterogeneous gold catalysis employing molecular oxygen and *tert*-butyl hydroperoxide (TBHP) as an initiator.<sup>12</sup> Dioxygen as a direct oxidizing agent significantly lowers costs of industrial processes and dramatically enhances the atom efficiency of the overall reaction compared to other “green” oxidants like hydrogenperoxide. Gold catalysts derived from Au<sub>55</sub> clusters below 2 nm work with pure oxygen, but show little selectivity.<sup>13</sup> Also many examples of alkene epoxidations requiring stoichiometric amounts of hydrogenperoxide can be found in the literature applying heterogeneous transition-metal containing<sup>14,15,16</sup> as well as transition-metal-free systems.<sup>17,18</sup>

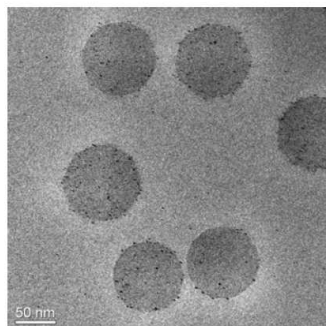
Recent work on core-shell nanoparticles consisting of a gold core and a palladium shell demonstrates that electronic interactions may enhance the catalytic activity for oxidation reactions.<sup>19</sup> In a similar manner, our recent work has shown that homogeneous Au-Pt-nano-alloys exhibit a high activity for the selective oxidation of alcohols to aldehydes or ketones.<sup>3</sup> The nano-alloys have been generated on the surface of spherical polyelectrolyte brushes. The method is shown in Figure 1: Nano-alloy of gold and platinum generated on the surface of a spherical polyelectrolyte brush (SPB) as described recently.<sup>3</sup> Spherical polyelectrolyte brushes have been shown to be uniquely suited for the generation and immobilization of metallic nanoparticles.<sup>20,21</sup> Ions of metals, like gold, silver, palladium or platinum, can be immobilized on the surface layer of cationic SPB. Subsequent reduction with NaBH<sub>4</sub> under mild conditions then leads to metallic nanoparticles, firmly embedded in a dense layer of polyelectrolyte chains. In the same way particles of nano-alloys can be synthesized and immobilized on the surface layer of spherical polyelectrolyte brush particles by reduction of a mixture of the respective metalate ions.

Figure 2 displays the composite particles Au-Ir@SPB thus obtained. This micrograph has been obtained by cryogenic transmission electron microscopy (cryo-TEM) that allows us to analyze the particles in-situ, that is, directly in the aqueous dispersion. The image shows the morphology of the composite system. The Au-Ir nanoalloy particles are in the range of 1.8 nm

and monodisperse. It is also visible, that all nanoparticles are well located near the PS-core. For the other composite systems (Au-Rh@SPB and Au-Ru@SPB) we obtained similar results (see supplementary information).



**Figure 1.** Synthesis of nano-alloy particles on the surface of spherical polyelectrolyte brushes: The carrier particles are spherical polyelectrolyte brushes (SPB) that consist of a solid polystyrene (PS) core ( $R_H = 50$  nm) onto which cationic polyelectrolyte chains of 2-aminoethylmethacrylate (2-AEMH) are attached. In a first step the chloride counter-ions are exchanged against  $\text{AuCl}_4^-$ -ions, in a second step the rest of chloride-ions are exchanged against  $\text{PtCl}_4^{2-}$ -ions. During these steps the brush thickness  $L$  is decreasing from around 71 nm to 21 nm. Bimetallic  $\text{Au}_{45}\text{Pt}_{55}$  nano-alloy particles are generated by reduction of the mixture of these ions by  $\text{NaBH}_4$ . The same steps are used for the synthesis of Au-Rh and Au-Ru nanoalloys. This procedure leads to faceted Au-Rh- and Au-Ru-nanocrystals with a size of a few nanometers only. The alloy-nanocrystals are firmly embedded in the surface layer of polyelectrolyte chains and the entire composite particles exhibit an excellent colloidal stability.



**Figure 2.** Cryo-TEM image of Au-Ir@SPB nanocomposite particles. The nanoalloys are located near the PS-core.

**Table 1.** Compositions of Au-Pt, Au-Ir, Au-Rh, Au-Ru, pure Au and Pt nanocomposites.

System <sup>a</sup>	Metalate Ion Ratios <sup>b</sup>	Au/Me Theor. <sup>c</sup>	Au/Me Exp. <sup>d</sup>	Exp. Metal content <sup>e</sup>	$d_{MeNP}$ [nm] <sup>f</sup>
Au <sub>19</sub> Pt <sub>81</sub>		20:80	19:81	7.50	1.3 ± 0.5
Au <sub>39</sub> Pt <sub>61</sub>		40:60	39:61	7.35	2.0 ± 0.5
Au <sub>60</sub> Pt <sub>40</sub>		60:40	60:40	7.47	3.0 ± 0.5
Au <sub>80</sub> Pt <sub>20</sub>		80:20	80:20	7.50	4.0 ± 0.5
Au <sub>80</sub> Ir <sub>20</sub>		80:20	80:20	7.99	1.8 ± 0.1
Au <sub>11</sub> Rh <sub>89</sub>		11:89	11:89	7.94	2.0 ± 0.2
Au <sub>25</sub> Rh <sub>75</sub>		25:75	25:75	7.94	2.3 ± 0.3
Au <sub>43</sub> Rh <sub>57</sub>		43:57	43:57	8.06	2.8 ± 0.4
Au <sub>69</sub> Rh <sub>31</sub>		69:31	69:31	7.94	3.5 ± 0.5
Au <sub>12</sub> Ru <sub>88</sub>		12:88	12:88	8.09	1.2 ± 0.2
Au <sub>25</sub> Ru <sub>75</sub>		25:75	25:75	8.07	1.7 ± 0.3
Au <sub>46</sub> Ru <sub>54</sub>		46:54	46:54	8.21	2.9 ± 0.4
Au <sub>68</sub> Ru <sub>32</sub>		68:32	68:32	8.00	3.8 ± 0.3
Au <sub>1.7</sub>		Pure Au	Pure Au	7.51	1.7 ± 0.3
Au <sub>1.8</sub>		Pure Au	Pure Au	7.59	1.8 ± 0.3
Au <sub>2.5</sub>		Pure Au	Pure Au	7.29	2.5 ± 0.5
Au <sub>6.0</sub>		Pure Au	Pure Au	6.88	6.0 ± 0.75
Pt <sub>1.75</sub>		Pure Pt	Pure Pt	7.80	1.75 ± 0.25

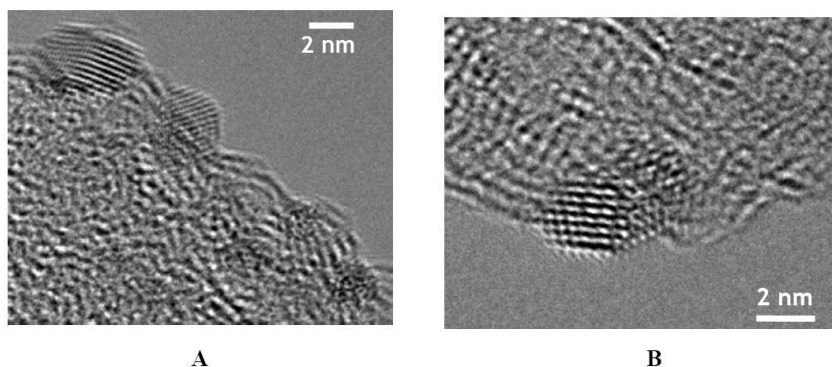
<sup>a</sup> sample name; <sup>b</sup> amount of  $[AuCl_4]^-$  and  $[PtCl_6]^{2-}/[IrCl_6]^{2-}/[RhCl_6]^{3-}/[RuCl_6]^{3-}$  introduced during ultrafiltration; <sup>c</sup> theoretical ratio of Au and Pt/Ir/Rh/Ru@SPB; <sup>d</sup> Measured ratio of Au/M in Au-M alloy NPs; <sup>e</sup> Total content of metal; <sup>f</sup> diameter of generated nano-alloy or M-NP on the carrier particles.

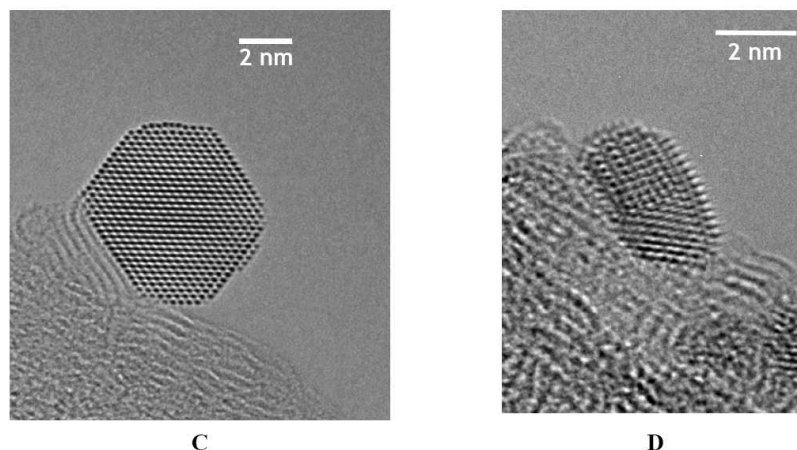
Here we synthesized three different new nano-alloys, namely Au-Ir, Au-Rh and Au-Ru immobilized on SPB (Table 1). In a typical experiment the synthesis was performed as described in Figure 1. Starting from the SPB the  $Cl^-$ -ions were exchanged against  $AuCl_4^-$ -ions. In the following step the suspension was purified by ultrafiltration (UF) from not complexed  $AuCl_4^-$ -ions in the system. Now the second metalate ion was introduced ( $PtCl_6^{2-}/IrCl_6^{2-}/RhCl_6^{3-}/RuCl_6^{3-}$ ) and the excess of  $Cl^-$ -ions was exchanged. Before reducing by  $NaBH_4$ , the system was purified again by UF.

In case of the Au-Ir alloys only the composition Au<sub>80</sub>Ir<sub>20</sub> proved to be stable. To the authors best knowledge we are the first, who synthesized an Au-Ir nano-alloy. The particle size is in

the range of 1.8 nm. The Au-Rh- and the Au-Ru-nano-alloys, however, could be obtained throughout the entire range of compositions, like the discussed Au-Pt nano-alloy in our previous paper.<sup>3</sup> For each alloy type four nano-alloys with different ratios of the metals were synthesized. Table 1 summarizes the resulting compositions. As shown by elemental analysis, the measured compositions are rather close to the ratios adjusted via ion exchange. The total content of metal ranges from 6.9 – 8.2 wt.-%. This result demonstrates that almost all metalate ions introduced previously have been reduced to metallic nanoparticles. It is also evident from Table 1 that the synthesis of the Au-Rh und Au-Ru alloys are highly reproducible. An evaluation of TEM micrographs shows, that the alloy size and morphology of the Au-Rh and Au-Ru particles depends on the composition of the alloy particle. For both types of alloy the average size of the nanoparticles (Table 1) decreases with increasing content of Rh and Ru respectively.

For more detailed studies about the structure and the composition we need a powerful instrument: High-resolution transmission electron microscopy (HR-TEM) in combination with electron dispersive X-ray spectroscopy (EDX) (supplementary information) is the method of choice for studying the resulting nanoparticles. Figure 3 shows the Au-Ir (**A** and **B**), Au-Rh (**C**) and Au-Ru (**D**) nanoalloys embedded into the polymerbrush. All three nanoalloys show crystallinity and a faceted morphology. The EDX analysis of the nanoalloys shows, that the theoretical values (Table 1) are in good agreement with the experimental results.

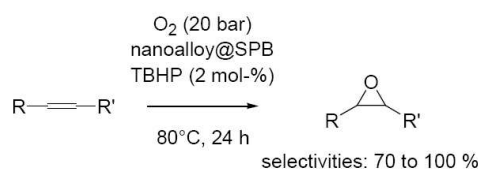




**Figure 3.** HR-TEM micrographs of the three different types of nanoalloys: (A) and (B) Au-Ir@SPB, (C) Au-Rh@SPB and (D) Au-Ru@SPB. All particles are faceted and the crystalline structure is by lattices recognizable. The diameter of the nanoparticles are Au-Ir (1.8 nm), Au-Rh (3.8 nm) and Au-Ru (2.8 nm).

**Figure 4.** WAXS- and Rietveld-analysis. (Vegard Gesetz?)

All synthesized nanoalloys@SPB are efficient catalysts for the solvent-free epoxidation of alkenes using molecular oxygen as an oxidant and catalytic activation via TBHP (Scheme 1).

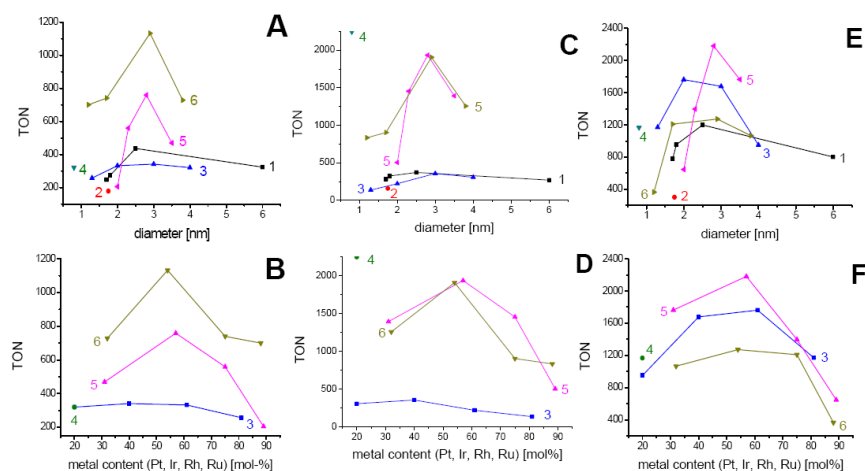


**Scheme 1.** Heterogeneous epoxidation of alkenes using nanoalloys@SPB as efficient catalysts and  $\text{O}_2$  as oxidant, activated by TBHP.

A reaction without addition of TBHP as activator does not take place, as well as an oxidation without catalyst. Below 2 mol-% of TBHP conversions decrease drastically. Catalytic activities depend on the particle size and show like demonstrated by Hayashi et al. the best results between 2 and 4 nm (Figure 5: A, C, E). Also a profound influence of the alloy on the TON can be observed, Au/Rh@SPB and Au/Ru@SPB are in all cases much better catalysts than pure gold particles (Figure 5: A [1, 5, 6], C [1, 5, 6], E [1, 5, 6]). This positive effect of alloying on the catalytic performance of nanoparticles has been shown by Enache et al.<sup>19</sup> in the case of alcohol oxidation, there the catalytic activity is enhanced by factor 25, if Pd/Au-particles are employed compared to pure gold particles. In the present investigation similar effects are observed: The activity in the epoxidation of cyclooctene using Au/Ru@SPB

compared to pure gold particles is elevated by factor 4 (Figure 5 A), this effect is even more evident in the case of *trans*-stilbene, here Au/Rh@SPB and Au/Ru@SPB show a five-fold activity (Figure 5 C), the alloy of Au<sub>80</sub>Ir<sub>20</sub> (Table 1) exhibits already an enhancement of the TON by factor seven compared to pure gold particles, unfortunately Au/Ir-alloys@SPB are only stable at this composition. Less pronounced this effect can be observed for the allylic oxidation of cyclohexene (Figure 5 E). Very insightful is the plot of the TON vs. content of the extrinsic metal in the alloy, all three cases exhibit a „magic composition“, at which the highest activity is obtained (Figure 5 B, D, F). This „magic composition“ everytime is around 50 mol-% extrinsic metal. A possible explanation lies in the nature of the particles, they are all solid solutions, i.e. mixed nanoparticles.<sup>2</sup> The highest degree of mixing between the two metals and possibly also the greatest effect of alloying is obtained at a 50:50 mixture of the two platinum metals. The achieved TONs in case of the nanoalloys lie noticeably above the ones obtained by Hughes et al. employing pure gold particles (*cycloocten*: Au@C→781; Au<sub>46</sub>Ru<sub>54</sub>→1132). Also the TOF (turnover frequency) of the conversion is close to obtained results, e.g. styrene conversion using Au<sub>55</sub>@SiO<sub>2</sub> is at 0.03 s<sup>-1</sup> (toluene, 100°C, 0.5 bar O<sub>2</sub>) same as the *trans*-stilbene epoxidation employing Au<sub>80</sub>Ir<sub>20</sub> (thf, 80°C, 20 bar O<sub>2</sub>). If cyclohexene is employed an epoxidation of the double bond is not achieved, instead a selective allylic oxidation (90 % selectivity towards 2-cyclohexene-1-one) like in the case of Liu et al.<sup>22</sup> is observed. The epoxidation of *trans*-stilbene yields benzaldehyde as a byproduct, which stems from the decay of 1,2-diphenylethane-1,2-dione (double oxidation of the double bond). The reaction is 80% *trans*-stilbenoxide-selective. A crucial problem using the SPB support is its instability under the applied reaction conditions, the polystyrene cores with the grafted carrier brushes are completely dissolved at the elevated temperatures and release the metal particles. This can be deduced from e.g. dark red coloured solutions after catalysis, if pure gold particles are employed (dark grey for pure platinum particles). The solubility of the carrier system is likely to be the reason for the relatively low TONs, despite the high temperatures. In search for a flawless and inert support two different approaches are carried out in our labs currently. One is the cross-linking of the polystyrene cores to minimize their solubility and the other is the transfer of the tailor-made particles to inert carrier systems (MOFs, SBAs, MCMs, PILCs, ...).





**Figure 5.** The TONs (*turn over numbers*) of the epoxidation reaction of A, B: cyclooctene yielding cycloocteneoxide and C, D: *trans*-stilbene yielding *trans*-stilbenesoxide as well as the allylic oxidation of E, F: cyclohexene yielding 2-cyclohexene-1-one employing Au/M@SPB as catalyst are shown in dependence of the particle size of the gold/metal-nanoalloys and the size of the pure gold- and platinumnanoparticles respectively as soon as the composition of the nanoalloy (1 = black: pure Au-nanoparticles; 2 = red: pure Pt-nanoparticles; 3 = blue: Au/Pt-nanoalloys; 4 = olive: Au/Ir-nanoalloys; 5 = magenta: Au/Rh-nanoalloy; 6 = dark yellow: Au/Ru-nanoalloys). Reaction conditions: 0.5 ml or 0.5 g (+ 2 ml THF) alkene, 1 mg catalyst, TBHP (2 mol%), O<sub>2</sub> (20 bar), 80°C, 24 h.

**Acknowledgements:** Financial support by the Deutsche Forschungsgemeinschaft, SFB 481, Bayreuth, by the BASF SE, and by the Fonds der Chemischen Industrie is gratefully acknowledged. Marc Schrinner thanks the Minerva Foundation, the German Academic Exchange Service (DAAD), and the Russell Berrie Nanotechnology Institute (RBNI) for the support during his stay at the Technion in Haifa.

## METHODS

**Materials and Synthesis:** Cationic spherical polyelectrolyte brushes carrying chains of poly(2-aminoethylmethacrylate hydrochloride) (PAEMH) were synthesized as described recently. The radius  $R$  of the core particles was 45 nm, the average contour length  $L_c$  of the grafted chains was 165 nm and the grafting density (number of chains per unit area) is 0.14 nm<sup>2</sup>. The entire number of charged groups in the polyelectrolyte layer was determined precisely by conductometric titration.<sup>23</sup> The gold and platinum nanoparticles were synthesized as described previously in Refs.<sup>24</sup>. In a typical experiment the bimetallic Au/M-NPs were generated as follows: In the first step 120 mL of latex (1.14 wt.-%) in pure water was placed in an ultrafiltration cell (NC 10 membrane filters, cellulosenitrate, Schleicher & Schuell, Germany) and 1 L of 3.3 · 10<sup>-4</sup> M HAuCl<sub>4</sub> (purchased from Aldrich: HAuCl<sub>4</sub>·3H<sub>2</sub>O) solution was passed through the cell. Subsequently, 500 mL of deionized water

(Millipore, Milli-Q, A-10) were passed through the cell to remove free  $\text{AuCl}_4^-$ -ions. The suspension attained a yellowish colour indicating an exchange of counterions in the brush layer from  $\text{Cl}^-$  to  $\text{AuCl}_4^-$ -ions. In the third step, 1 L of  $8 \cdot 10^{-5}$  M  $\text{H}_2\text{PtCl}_6$ /1 L of  $8 \cdot 10^{-5}$  M  $\text{Na}_2\text{IrCl}_6$ /1 L of  $8 \cdot 10^{-5}$  M  $\text{K}_3\text{RhCl}_6$ /1 L or  $8 \cdot 10^{-5}$  M  $\text{K}_3\text{RuCl}_6$  (purchased from Aldrich:  $\text{H}_2\text{PtCl}_6 \cdot 6\text{H}_2\text{O}$ / $\text{Na}_2\text{IrCl}_6 \cdot 6\text{H}_2\text{O}$ / $\text{K}_3\text{RhCl}_6$ / $\text{K}_3\text{RuCl}_6$ ) solutions were passed through the cell. The colour of the obtained dispersion changed to steel blue/purple/red/red depending on the amount of gold and platinum-/iridium-/rhodium- or ruthenium-ions in the serum. For generation of bimetallic nanoparticles the dispersion was mixed slowly with 5 mL of a  $4 \cdot 10^{-4}$  M solution of  $\text{NaBH}_4$  through stirring under an atmosphere of nitrogen. The reduction of the  $\text{AuCl}_4^-$ - and  $\text{PtCl}_6^{2-}$ -/ $\text{IrCl}_6^{2-}$ -/ $\text{RhCl}_6^{3-}$ -/ $\text{RuCl}_6^{3-}$ -ions could be followed easily by a change of colour, dependent on the composition. After completion of the reaction the suspension was placed in an ultrafiltration cell and a five-fold excess of deionized water was passed through the cell. The purification was monitored by measuring the conductivity of the serum.

**Freeze-Drying of Catalyst Solutions:** In a typical experiment the composite dispersion was freeze-dried for two days. For this purpose the sample was frozen in liquid nitrogen for 10 minutes. Then it was dried with a freeze-dryer (ALPHA 1-2, CHRIST). The obtained powder was used as a catalyst.

**Characterization Methods:** Cryogenic transmission electron microscopy (cryo-TEM) and transmission electron microscopy (TEM) were carried out using a LEO9220 (200 kV) as described previously. High-resolution TEM (HR-TEM) and EDX analysis were done using a FEI Titan (300 kV). The samples were prepared as follows: A drop of liquid was placed on a grid (Plano S 166-3). After drying in air for three minutes the rest of the liquid was taken off by a filter paper. Dynamic light scattering (DLS) was done using a Peters ALV 4000 light scattering goniometer and elemental analysis measurements were done using a Vario elemental EL III – CHN as described previously.

**General Epoxidation / Allylic Oxidation Protocol:** The reactions were carried out under a 20 bar dioxygen atmosphere in a steel autoclave (Parr Instrument). The reaction mixture always contained 0.5 mL liquid alkene (*cis*-cyclooctene or cyclohexene) or 0.5 g solid alkene (*trans*-stilbene) dissolved in 2 mL of thf, 1 mg of solid catalyst and 2 mol% TBHP (6 M solution in decane). The autoclave was sealed, 20 bar of oxygen atmosphere were applied and the reaction mixture was stirred for 24 h at  $80^\circ\text{C}$ . At the end of the reaction 2 mL of thf were added in case of the liquid alkenes and 0.5 mmol of dodecane (113  $\mu\text{L}$ ) in all cases. The conversion was checked via GC or GC-MS, if new products had to be identified (GC analyses were performed on an Agilent 6890N gas chromatograph equipped with a flame ionisation detector (FID) and an Agilent 19091J-413 FS capillary column; GC-MS analyses were performed on a Thermo Focus DSQ apparatus equipped with the same column using dodecane as internal standard.). Results are shown in Table 2 (supplementary information).

<sup>1</sup> Alloy treatise

<sup>2</sup> Ferrando, R., Jellinek, J., Johnston, R. L. Nanoalloys: From Theory to Applications of Alloy Clusters and Nanoparticles. *Chem. Rev.* **108**, 845-910 (2008).

<sup>3</sup> Schrinner, M., Proch, S., Mei, Y., Kempe, R., Miyajima, N., Ballauff, M. Stable bimetallic gold-platinum nanoparticles immobilized on spherical polyelectrolyte brushes: synthesis, characterization, and application for the oxidation of alcohols. *Adv. Mater.* **20**, 1928-1933 (2008).

<sup>4</sup> Dalton, C. D., Ryan, K. M., Wall, V. M., Bousquet, C., Gilheany, D. G. Recent progress towards the understanding of metal-salen catalyzed asymmetric alkene epoxidation. *Top. Catal.* **5**, 75-91 (1998).

- 
- <sup>5</sup> Sielaff G., Rieth, R., Rowbottom K. T. *Ullmann's Encyclopedia of Organic Chemicals Vol. 4*, Wiley-VCH, Weinheim (1999).
- <sup>6</sup> Haruta, M., Yamada, N., Kobayashi, T., Iijima, S. Gold catalysts prepared by coprecipitation for low-temperature oxidation of hydrogen and of carbon monoxide. *J. Catal.* **115**, 301-309 (1989).
- <sup>7</sup> Hashmi, A., Stephen, K. Gold-catalyzed organic reactions. *Chem. Rev.* **107**, 3180-3211 (2007).
- <sup>8</sup> Hayashi, T., Tanaka, K., Haruta, M. Selective vapor-phase epoxidation of propylene over Au/TiO<sub>2</sub> catalysts in the presence of oxygen and hydrogen. *J. Catal.* **178**, 566-575 (1998).
- <sup>9</sup> Haruta, M., Masakazu, D. Advances in the catalysis of Au nanoparticles. *Appl. Catal. A* **222**, 427-437 (2001).
- <sup>10</sup> Sinha, A. K., Seelan, S., Tsubota, S., Haruta, M. A three-dimensional mesoporous titanosilicate support for gold nanoparticles: Vapor-phase epoxidation of propene with high conversion. *Angew. Chem.* **116**, 1572-1574 (2004); A three-dimensional mesoporous titanosilicate support for gold nanoparticles: Vapor-phase epoxidation of propene with high conversion. *Angew. Chem. Int. Ed.* **43**, 1546-1548 (2004).
- <sup>11</sup> Chowdhury, B., Bravo-Suárez, J. J., Daté, M., Tsubota, S., Haruta, M. Trimethylamine as a gas-phase promoter: Highly efficient epoxidation of propylene over supported gold catalysts. *Angew. Chem.* **118**, 426-429 (2006); Trimethylamine as a gas-phase promoter: Highly efficient epoxidation of propylene over supported gold catalysts. *Angew. Chem. Int. Ed.* **43**, 412-415 (2006).
- <sup>12</sup> Hughes, M. D., Xu, Y.-J., Jenkins, P., McMorn, P., Landon, P., Enache, D. I., Carley, A. F., Attard, G. A., Hutchings, G. J., King, F., Stitt, E. H., Johnston, P., Griffin, K., Kiely, C. J. Tunable gold catalysts for selective hydrocarbon oxidation under mild conditions. *Nature* **437**, 1132-1135 (2005).
- <sup>13</sup> Tümer, M., Golovko, V. B., Vaughan, O. P. H., Abdulkın, P., Berenguer-Murcia, A., Tikhov, M. S., Johnson, B. F. G., Lambert, R. M. Selective oxidation with dioxygen by gold nanoparticle catalysts derived from 55-atom clusters. *Nature* **454**, 981-984 (2008).
- <sup>14</sup> Nakagawa, Y., Kamata, K., Kotani, M., Yamaguchi, K., Mizuno, N. Polyoxovanadometalate-catalyzed selective epoxidation of alkenes with hydrogen peroxide. *Angew. Chem.* **117**, 5266-5271 (2005); Polyoxovanadometalate-catalyzed selective epoxidation of alkenes with hydrogen peroxide. *Angew. Chem. Int. Ed.* **44**, 5136-5141 (2005).
- <sup>15</sup> Serafimidou, A., Stamatis, A., Louloudi, M. Manganese(II) complexes of imidazole based-acetamide as homogeneous and heterogenized catalysts for alkene epoxidation with H<sub>2</sub>O<sub>2</sub>. *Catal. Commun.* **9**, 35-39 (2007).

- <sup>16</sup> Wang, Y. M., Magustin, P. C. M. M., Van Santen, R. A., Abbenhuis, H. C. L. Organo-bridged silsesquioxane titanates for heterogeneous catalytic epoxidation with aqueous hydrogen peroxide. *J. Catal.* **251**, 453-458 (2007).
- <sup>17</sup> Pescarmona, P. P., Janssen, K. P. F., Jacobs, P. A. Novel transition-metal-free heterogeneous epoxidation catalysts discovered by means of high-throughput experimentation. *Chem. Eur. J.* **13**, 6562-6572 (2007).
- <sup>18</sup> Pescarmona, P. P., Van Noyen, J., Jacobs, P. A. Transition-metal-free microporous and mesoporous catalysts for the epoxidation of cyclooctene with hydrogen peroxide. *J. Catal.* **251**, 307-314 (2007).
- <sup>19</sup> Enache, D. I., Edwards, J. K., Landon, P., Solsona-Espriu, B., Carley, A. F., Herzing, A. A., Watanabe, M., Kiely, C. J., Knight, D. W., Hutchings, Solvent-Free Oxidation of Primary Alcohols to Aldehydes Using Au-Pd/TiO<sub>2</sub> Catalysts. *Science* **311**, 362-365 (2006).
- <sup>20</sup> Ballauff, M. Spherical polyelectrolyte brushes. *Progr. Polym. Sci.* **32**, 1135-1151 (2007).
- <sup>21</sup> Lu, Y., Mei, Y., Schrinner, M., Ballauff, M., Möller, M. W., Breu, J., In Situ Formation of Ag Nanoparticles in Spherical Polyacrylic Acid Brushes by UV Irradiation. *J. Phys. Chem. C* **111**, 7676-7681 (2007).
- <sup>22</sup> J. Liu, J., F. Wang, F., X. Xu, X. Creation of a monomeric Ag species on the surface of  $\gamma$ -ZrP as an efficient heterogeneous catalyst for the selective oxidation of cycloolefins. *Catalysis Lett.* **120**, 106-110 (2008).
- <sup>23</sup> Schrinner, M., Polzer, F., Mei, Y., Lu, Y., Haupt, B., Ballauff, M., Goldel, A., Drechsler, M., Preussner, J., Glatzel, U. Mechanism of the formation of amorphous gold nanoparticles within spherical polyelectrolyte brushes. *Macromol. Chem. Phys.* **208**, 1542-1547 (2007).
- <sup>24</sup> Y. Mei, G. Sharma, Y. Lu, M. Drechsler, T. Irrgang, R. Kempe, M. Ballauff, High Catalytic Activity of Platinum Nanoparticles Immobilized on Spherical Polyelectrolyte Brushes. *Langmuir* **21**, 12229-12234 (2005).

## Supplementary Information

### Nanoalloys as efficient “green” catalysts for the epoxidation of alkenes by molecular oxygen

*Marc Schrimmer<sup>a</sup>, Matthias Ballauff<sup>a</sup>  
Salem Deeb<sup>b</sup>, Sebastian Proch<sup>b</sup>, Rhet Kempe<sup>b</sup>  
Yaron Kauffmann<sup>c</sup>  
Jürgen Thun<sup>d</sup>, Josef Breu<sup>d</sup>*

- a) Lehrstuhl für Physikalische Chemie I, Universität Bayreuth, Universitätsstraße 30,  
D-95440 Bayreuth (Germany)
- b) Lehrstuhl für Anorganische Chemie II, Universität Bayreuth, Universitätsstraße 30,  
D-95440 Bayreuth (Germany)
- c) Department of Materials Engineering, Israel Institute of Technology, Technion,  
Haifa 32000 (Israel)
- d) Lehrstuhl für Anorganische Chemie I, Universität Bayreuth, Universitätsstraße 30,  
D-95440 Bayreuth (Germany)





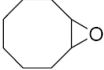

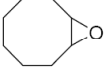

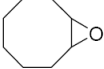
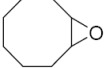
***Date: October 8<sup>th</sup> 2008***


Table 1. Overview of all synthesized metallic nanoalloys supported on SPB.

<b>Name (pure gold)</b>	<b>wt.% Au</b>		<b>wt.% metal</b>	<b>mol% Au</b>		<b>M<sub>average</sub></b>	<b>Diameter [nm]</b>
Au <sub>1.7</sub>	7.51	-	7.51	100	-	197	1.7 ± 0.3
Au <sub>1.8</sub>	7.59	-	7.59	100	-	197	1.8 ± 0.3
Au <sub>2.5</sub>	7.29	-	7.29	100	-	197	2.5 ± 0.5
Au <sub>6.0</sub>	6.88	-	6.88	100	-	197	6.0 ± 0.75
<b>Name (pure platinum)</b>		<b>wt.% Pt</b>	<b>wt.% metal</b>		<b>mol% Pt</b>	<b>M<sub>average</sub></b>	<b>Diameter [nm]</b>
Pt <sub>1.75</sub>	-	7.80	7.80	-	100	195	1.75 ± 0.25
<b>Name (gold/platinum alloys)</b>	<b>wt.% Au</b>	<b>wt.% Pt</b>	<b>wt.% metal</b>	<b>mol% Au</b>	<b>mol% Pt</b>	<b>M<sub>average</sub></b>	<b>Diameter [nm]</b>
Au <sub>19</sub> Pt <sub>81</sub>	1.45	6.05	7.50	19.18	80.81	195.36	1.3 ± 0.5
Au <sub>39</sub> Pt <sub>61</sub>	2.90	4.45	7.35	39.15	60.85	195.78	2.0 ± 0.5
Au <sub>60</sub> Pt <sub>40</sub>	4.48	2.99	7.47	59.75	40.25	196.20	3.0 ± 0.5
Au <sub>20</sub> Pt <sub>80</sub>	5.98	1.52	7.50	79.54	20.46	196.59	4.0 ± 0.5
<b>Name (gold/iridium alloys)</b>	<b>wt.% Au</b>	<b>wt.% Ir</b>	<b>wt.% metal</b>	<b>mol% Au</b>	<b>mol% Ir</b>	<b>M<sub>average</sub></b>	<b>Diameter [nm]</b>
Au <sub>80</sub> Ir <sub>20</sub>	6.43	1.56	7.99	80.09	19.91	196.02	1.8 ± 0.1
<b>Name (gold/rhodium alloys)</b>	<b>wt.% Au</b>	<b>wt.% Rh</b>	<b>wt.% metal</b>	<b>mol% Au</b>	<b>mol% Rh</b>	<b>M<sub>average</sub></b>	<b>Diameter [nm]</b>
Au <sub>11</sub> Rh <sub>89</sub>	1.56	6.38	7.94	10.65	89.35	112.93	2.0 ± 0.2
Au <sub>25</sub> Rh <sub>75</sub>	3.13	4.82	7.94	25.31	74.69	126.72	2.3 ± 0.3
Au <sub>43</sub> Rh <sub>57</sub>	4.78	3.28	8.06	43.18	56.82	143.53	2.8 ± 0.4
Au <sub>69</sub> Rh <sub>31</sub>	6.41	1.53	7.94	68.60	31.40	167.45	3.5 ± 0.5
<b>Name (gold/ruthenium alloys)</b>	<b>wt.% Au</b>	<b>wt.% Ru</b>	<b>wt.% metal</b>	<b>mol% Au</b>	<b>mol% Ru</b>	<b>M<sub>average</sub></b>	<b>Diameter [nm]</b>
Au <sub>12</sub> Ru <sub>88</sub>	1.72	6.37	8.09	12.17	87.83	112.77	1.2 ± 0.2
Au <sub>25</sub> Ru <sub>75</sub>	3.17	4.90	8.07	24.93	75.07	125.00	1.7 ± 0.3

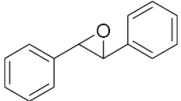
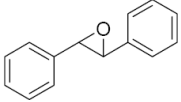
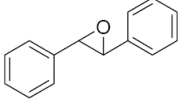
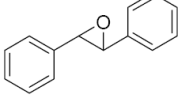
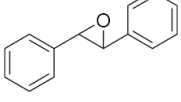
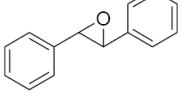
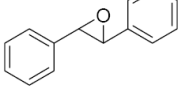
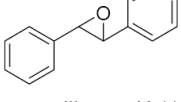
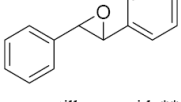
Au <sub>46</sub> Ru <sub>54</sub>	5.13	3.08	8.21	46.09	53.91	145.29	2.9 ± 0.4
Au <sub>68</sub> Ru <sub>32</sub>	6.46	1.54	8.00	68.29	31.71	166.56	3.8 ± 0.3

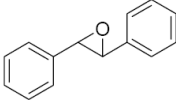
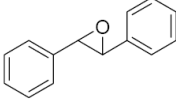
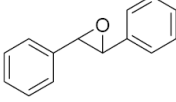
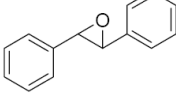
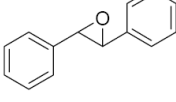
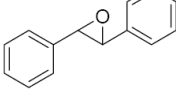
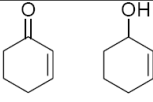
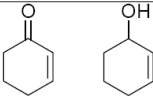
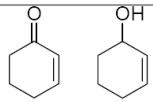
Table 2. Catalytic activities of nanoalloys@SPB.

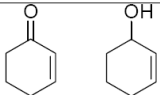
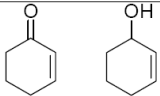
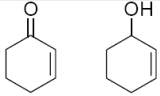
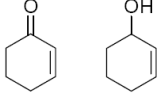
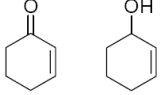
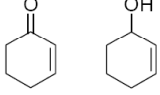
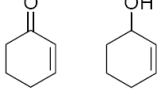
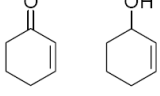
Product	Catalyst	GC-Conversion	TON*
 cyclooctene oxide	Au <sub>1.7</sub>	2.5	247
 cyclooctene oxide	Au <sub>1.8</sub>	2.7	273
 cyclooctene oxide	Au <sub>2.5</sub>	4.2	436
 cyclooctene oxide	Au <sub>6.0</sub>	3.0	323
 cyclooctene oxide	Pt <sub>1.75</sub>	1.9	178
 cyclooctene oxide	Au <sub>19</sub> Pt <sub>81</sub>	2.6	257
 cyclooctene oxide	Au <sub>39</sub> Pt <sub>61</sub>	3.3	332
 cyclooctene oxide	Au <sub>60</sub> Pt <sub>40</sub>	3.4	341
 cyclooctene oxide	Au <sub>80</sub> Pt <sub>20</sub>	3.2	320
 cyclooctene oxide	Au <sub>80</sub> Ir <sub>20</sub>	3.4	320

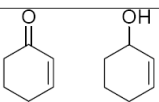
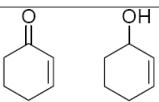
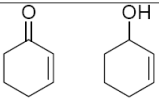
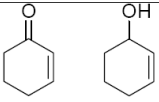
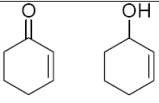
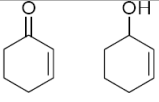
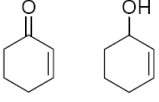
 cyclooctene oxide	<b>Au<sub>11</sub>Rh<sub>89</sub></b>	3.8	205
 cyclooctene oxide	<b>Au<sub>25</sub>Rh<sub>75</sub></b>	9.2	559
 cyclooctene oxide	<b>Au<sub>43</sub>Rh<sub>57</sub></b>	11.2	759
 cyclooctene oxide	<b>Au<sub>69</sub>Rh<sub>31</sub></b>	5.8	469
 cyclooctene oxide	<b>Au<sub>12</sub>Ru<sub>88</sub></b>	13.2	700
 cyclooctene oxide	<b>Au<sub>25</sub>Ru<sub>75</sub></b>	12.6	740
 cyclooctene oxide	<b>Au<sub>46</sub>Ru<sub>54</sub></b>	16.8	1132
 cyclooctene oxide	<b>Au<sub>68</sub>Ru<sub>32</sub></b>	9.2	728
 <i>trans</i> -stilbene oxide**	<b>Au<sub>1,7</sub></b>	3.8 (1.2, 76% epoxide selectivity)	281
 <i>trans</i> -stilbene oxide**	<b>Au<sub>1,8</sub></b>	4.5 (1.7, 72% epoxide selectivity)	324
 <i>trans</i> -stilbene oxide**	<b>Au<sub>2,5</sub></b>	4.9 (0.6, 89% epoxide selectivity)	372



 trans-stilbene oxide**	<b>Au<sub>6,0</sub></b>	3.3 (0.9, 79% epoxide selectivity)	268
 trans-stilbene oxide**	<b>Pt<sub>1.75</sub></b>	2.2 (0.7, 76% epoxide selectivity)	157
 trans-stilbene oxide**	<b>Au<sub>19</sub>Pt<sub>81</sub></b>	1.9 (0.4, 83% epoxide selectivity)	136
 trans-stilbene oxide**	<b>Au<sub>39</sub>Pt<sub>61</sub></b>	3.0 (1.0, 75% epoxide selectivity)	221
 trans-stilbene oxide**	<b>Au<sub>60</sub>Pt<sub>40</sub></b>	4.9 (1.5, 76% epoxide selectivity)	357
 trans-stilbene oxide**	<b>Au<sub>80</sub>Pt<sub>20</sub></b>	4.2 (1.3, 77% epoxide selectivity)	307
 trans-stilbene oxide**	<b>Au<sub>80</sub>Ir<sub>20</sub></b>	32.6 (7.8, 81% epoxide selectivity)	2242
 trans-stilbene oxide**	<b>Au<sub>11</sub>Rh<sub>89</sub></b>	12.6 (3.1, 80% epoxide selectivity)	503
 trans-stilbene oxide**	<b>Au<sub>25</sub>Rh<sub>75</sub></b>	32.5 (10.7, 75% epoxide selectivity)	1453

 <i>trans</i> -stilbene oxide**	<b>Au<sub>43</sub>Rh<sub>57</sub></b>	38.8 (12.5, 76% epoxide selectivity)	1933
 <i>trans</i> -stilbene oxide**	<b>Au<sub>69</sub>Rh<sub>31</sub></b>	23.6 (10.2, 70% epoxide selectivity)	1391
 <i>trans</i> -stilbene oxide**	<b>Au<sub>12</sub>Ru<sub>88</sub></b>	21.3 (4.9, 81% epoxide selectivity)	833
 <i>trans</i> -stilbene oxide**	<b>Au<sub>25</sub>Ru<sub>75</sub></b>	20.8 (4.7, 82% epoxide selectivity)	903
 <i>trans</i> -stilbene oxide**	<b>Au<sub>46</sub>Ru<sub>54</sub></b>	38.4 (9.6, 80% epoxide selectivity)	1905
 <i>trans</i> -stilbene oxide**	<b>Au<sub>68</sub>Ru<sub>32</sub></b>	21.5 (5.4, 80% epoxide selectivity)	1255
 2-cyclohexene-1-one 2-cyclohexene-1-ol***	<b>Au<sub>1.7</sub></b>	6.0 (0.8, 91% ketone selectivity)	780
 2-cyclohexene-1-one 2-cyclohexene-1-ol***	<b>Au<sub>1.8</sub></b>	4.7 (0.6, 89% ketone selectivity)	954
 2-cyclohexene-1-one	<b>Au<sub>2.5</sub></b>	9.1 (1.5, 86% ketone selectivity)	1200

2-cyclohexene-1-ol***			
 2-cyclohexene-1-one 2-cyclohexene-1-ol***	<b>Au<sub>6.0</sub></b>	5.7 (0.7, 89% ketone selectivity)	802
 2-cyclohexene-1-one 2-cyclohexene-1-ol***	<b>Pt<sub>1.75</sub></b>	2.5 (0.4, 87% ketone selectivity)	301
 2-cyclohexene-1-one 2-cyclohexene-1-ol***	<b>Au<sub>19</sub>Pt<sub>81</sub></b>	9.2 (1.0, 90% ketone selectivity)	1171
 2-cyclohexene-1-one 2-cyclohexene-1-ol***	<b>Au<sub>39</sub>Pt<sub>61</sub></b>	13.5 (2.0, 87% ketone selectivity)	1764
 2-cyclohexene-1-one 2-cyclohexene-1-ol***	<b>Au<sub>60</sub>Pt<sub>40</sub></b>	13.0 (1.16, 92% ketone selectivity)	1680
 2-cyclohexene-1-one 2-cyclohexene-1-ol***	<b>Au<sub>80</sub>Pt<sub>20</sub></b>	7.4 (0.92, 89% ketone selectivity)	951
 2-cyclohexene-1-one 2-cyclohexene-1-ol***	<b>Au<sub>80</sub>Ir<sub>20</sub></b>	9.7 (1.2, 89% ketone selectivity)	1168
 2-cyclohexene-1-one 2-cyclohexene-1-ol***	<b>Au<sub>11</sub>Rh<sub>89</sub></b>	9.3 (1.5, 86% ketone selectivity)	646

2-cyclohexene-1-one 2-cyclohexene-1-ol***			
 2-cyclohexene-1-one 2-cyclohexene-1-ol***	<b>Au<sub>25</sub>Rh<sub>75</sub></b>	17.9 (2.2, 89% ketone selectivity)	1398
 2-cyclohexene-1-one 2-cyclohexene-1-ol***	<b>Au<sub>43</sub>Rh<sub>57</sub></b>	25.0 (3.4, 88% ketone selectivity)	2182
 2-cyclohexene-1-one 2-cyclohexene-1-ol***	<b>Au<sub>69</sub>Rh<sub>31</sub></b>	17.1 (2.3, 88% ketone selectivity)	1765
 2-cyclohexene-1-one 2-cyclohexene-1-ol***	<b>Au<sub>12</sub>Ru<sub>88</sub></b>	5.3 (0.9, 86% ketone selectivity)	364
 2-cyclohexene-1-one 2-cyclohexene-1-ol***	<b>Au<sub>25</sub>Ru<sub>75</sub></b>	15.9 (2.0, 89% ketone selectivity)	1210
 2-cyclohexene-1-one 2-cyclohexene-1-ol***	<b>Au<sub>46</sub>Ru<sub>54</sub></b>	14.7 (3.4, 81% ketone selectivity)	1273
 2-cyclohexene-1-one 2-cyclohexene-1-ol***	<b>Au<sub>68</sub>Ru<sub>32</sub></b>	10.5 (1.6, 87% ketone selectivity)	1067

\* TONs shown in

Table 2 are based on the total number of metal atoms contained in the composite material.

\*\* trans-stilbene gave benzaldehyde as a byproduct, the numbers in brackets give the conversion of diketone (1,2-diphenyl-ethane-1,2-dione) from which the benzaldehyde emerges and epoxide selectivity.

\*\*\* 2-cyclohexene-1-one selectivity compared to 2-cyclohexene-1-ol is given in brackets. TON corresponds to production of 2-cyclohexene-1-one (main product).



## 4 Summary / Zusammenfassung

- *Summary:*

First of all the up scaled synthesis for cationic and anionic spherical polyelectrolyte brushes (SPB) was introduced and a reproducible method for the synthesis was established (Chapter 3.1). For a better understanding of anionic SPB the complexation of the anionic polyelectrolyte chains with the cationic surfactant cetyl trimethyl ammonium bromide was studied in detail. The models were proved by cryogenic transmission electron microscopy (cryo-TEM) and dynamic light scattering (DLS), if it's in good agreement with the resulting systems (Chapter 3.2).

It was possible to show, that cationic SPB could be used for the generation of gold nanoparticles (Chapter 3.3). The synthesized carrier systems were characterized in detail by transmission electron microscopy (TEM), cryo-TEM and disc centrifuge (DCP). The more detail examination of the Au/SPB system by DLS, TEM/cryo-TEM, showed that a reversible immobilization system for gold nanoparticles was synthesized. The immobilized gold nanoparticles@SPB could be complexed by cyanid ions and oxygen. After the complexation of the gold nanoparticles we get the previous carrier system back. Detailed studies by wide angle X-ray scattering (WAXS) and high resolution transmission electron microscopy (HR-TEM) show an amorphous morphology of the gold nanoparticles in the range of 1 nm. This kind of generation allow us to generate gold nanoparticles in the range of 1.0 and 2.5 nm on the surface of the carrier particle.

In the following part of the thesis the concepts described above were used for the synthesis of binary gold nanoalloys (Chapter 3.4 and 3.6). The binary systems Au-Pt, Au-Ru, Au-Rh and Au-Ir were sucessfully generated. In the next step the nanoparticular structure of these binary systems were completely clarified by different HR-TEM methods and WAXS. It was shown, that there is a different behaviour between macroscopic and nanoscopic world. Bulk Au-Pt alloys show miscibility gaps, whereas Au-Pt nanoalloys have no such miscibility gap. This alloy obeys the Vegard's law. For the generation of facettet Pt nanocrystals (Chapter 3.5), the complexation of gold atoms by cyanid ions and oxygen is used.

By this way it's possible to synthesize well-ordered PtNP structures starting from the Au-Pt nanoalloy.

In the second part of the thesis the immobilized gold nanoparticles and the binary gold nanoalloys applied as catalysts for industrial interesting oxidation reactions of alcohols and epoxidation reactions (Chapter 3.4 and 3.6) were studied. All reactions could be conducted at room temperature and in water as reaction media. The catalytic activities have a strong dependency on the composition in the nanoalloy. Cryo-TEM characterization showed us no change of the morphology of the catalyst before and after a catalyst cyclus.

Concluding this thesis showed successfully a new route for the synthesis of monodispers and well defined gold nanoparticles, gold nanoalloys and faceted platinum nanocrystals. The particle sizes ranges between 1.0 and 7.0 nm. All systems can be used as green catalysts. This is an important point in the discussion of sustainability. All dispersions are not light and air sensitive, so they can be handled without any problems.

- **Zusammenfassung:**

Im Rahmen dieser Arbeit wurde in einem ersten Teil eine großtechnische Synthese für kationische und anionische sphärische Polyelektrolyt (SPB)-Dispersionssysteme eingeführt (Kapitel 3.1). Zum tiefergehenden Verständnis der anionischen sphärischen Polyelektrolyte wurde die Komplexbildung zwischen Tensid CTAB und den Polyelektrolytketten eingehend untersucht. Die Modellvorstellungen wurden mittels kryogener Transmissionselektronenmikroskopie (*cryo*-TEM) und dynamischer Lichtstreuung (DLS) untermauert (Kapitel 3.2).

Es konnte gezeigt werden, dass sich kationische SPB als Trägersysteme für Goldnanopartikel eignen (Kapitel 3.3). Das synthetisierte Trägersystem wurde mittels dynamischer Lichtstreuung (DLS), Transmissionselektronenmikroskopie (TEM) / Tieftemperaturtransmissionselektronenmikroskopie (*cryo*-TEM) und Scheibenzentrifuge (DCP) charakterisiert. Die eingehendere Untersuchung des Gold-Kern/Schale-Trägersystems mittels DLS und TEM/*cryo*-TEM zeigte, dass ein reversibles Immobilisierungssystem für AuNP gezielt synthetisiert worden und reproduzierbar herstellbar ist. Die auf der Oberfläche des PS-Kerns durch die



Wechselwirkung mit den funktionellen Gruppen der Polyelektrolytketten immobilisierten Au-Partikel ließen sich zerstörungsfrei durch Cyanidionen/Sauerstoff unter Komplexbildung herauslösen. Anschließend war das zu Beginn eingesetzte SPB Trägersystem zerstörungsfrei erhalten. Des Weiteren war es durch systematische Studien möglich, sehr einheitliche AuNP auf der PS-Kernoberfläche zu generieren, die je nach Bedarf im Bereich von 1 – 2,5 nm gezielt hergestellt werden können. Die Untersuchung der 1 nm großen Nanopartikel zeigte eine amorphe Struktur.

In einem weiteren Teil der Arbeit wurden die für Goldnanopartikel gewonnen Konzepte nun zur Generierung von Goldnanolegierungen (Kapitel 3.4 und 3.6) angewendet. So konnten die binären Systeme Au-Pt, Au-Ir, Au-Ru, Au-Rh mit Erfolg synthetisiert werden, sowie deren Struktur mit Hilfe verschiedener HR-TEM Methoden und WAXS vollkommen aufgeklärt werden. Diese Untersuchungen zeigten die vollkommen unterschiedlichen Strukturen zwischen makroskopischen und nanoskopischen Legierungen. So weisen Au-Pt Nanolegierungen keine Mischungslücke auf und gehorchen dem Vegard'schen Gesetz, wohingegen *bulk* Au-Pt Legierungen dieser Regel nicht gehorchen. Für die Generierung facettierter Pt-Nanokristalle (Kapitel 3.5) konnte die bereits angesprochene Komplexierung der Goldatome herangezogen werden. Aus den binären Au-Pt Nanolegierungen konnten mittels Cyanidionen/Sauerstoff geometrisch hochgeordnete Platin Nanokristalle gewonnen werden.

Der zweite Teil der Arbeit beschäftigt sich mit der Anwendung der immobilisierten Goldpartikel, sowie der binären Goldnanolegierungen als Katalysatoren in industriell bedeutsamen Alkoholorxidations- und Epoxidierungsreaktionen (Kapitel 3.4 und 3.6). Alle Reaktionen konnten bei Raumtemperatur mit den wässrigen Dispersionsmedien als Katalysatoren durchgeführt werden. Dabei zeigte sich für die katalytische Aktivität eine Abhängigkeit von der Legierungszusammensetzung. Cryo-TEM Untersuchungen zeigten, dass sich die Morphologie der Kompositpartikel nach dem Einsatz in der Katalyse nicht verändert.

Abschließend ist festzuhalten, dass die vorliegende Arbeit einen neuen Weg zur Generierung wohldefinierter und einheitlicher Goldnanopartikel, binärer Goldnanolegierungen, sowie facettierter Platinnanokristalle aufzeigt. Die

Nanopartikelgrößen können gezielt zwischen 1 und 7 nm eingestellt werden, sowie nahezu monodispers generiert werden. Es handelt sich bei allen Systemen um wässrige Dispersionen, die eine mehrjährige Licht- und Luftstabilität aufweisen. Im Hinblick auf den Einsatz als umweltfreundliche Katalysatoren wurde ein wesentlicher Beitrag geleistet.

## 5 Publications

### 5.1 Publications of this Thesis

- Samokhina, L.; Schrunner, M.; Ballauff, M.; Drechsler, M.: Binding of oppositely charged surfactants to spherical polyelectrolyte brushes: A study by cryogenic transmission electron microscopy, *Langmuir* **2007**, *23*, 3615.
- Schrunner, M.; Polzer, F.; Mei, Y.; Lu, Y.; Haupt, B.; Ballauff, M.; Gödel, A.; Drechsler, M.; Preussner, J.; Glatzel, U.: Mechanism of the Formation of Amorphous Gold Nanoparticles within Spherical Polyelectrolyte Brushes, *Macromol. Chem. Phys.* **2007**, *208*, 1542 (Coverarticle).
- Schrunner, M.; Proch, S.; Mei, Y.; Kempe, R.; Miyajima, N.; Ballauff, M.: Stable bimetallic Gold-Platinum Nanoparticles Immobilized on Spherical Polyelectrolyte Brushes: Synthesis, Characterization and Application for the Oxidation of Alcohols, *Adv. Mater.* **2008**, *20*, 1928.
- Schrunner, M.; Haupt, B.; Wittemann, A.: A novel photoreactor for the production of electrosterically stabilised colloidal particles at larger scales, *Chemical Engineering Journal* **2008**, *144*, 138.
- Schrunner, M.; Ballauff, M.; Talmon, Y.; Kauffmann, Y.; Thun, J.; Möller, M.; Breu, J.: Single Nanocrystals of Platinum Prepared by Partial Dissolution of Au-Pt-Nanoalloys, *Science* **2009**, *323*, 617.
- Schrunner, M.; Ballauff, M.; Deeb, S.; Proch, S.; Kempe, R.; Kauffmann, Y.; Thun, J.; Breu, J.: Nanoalloys as efficient „green“ catalysts for the epoxidation of alkenes by molecular oxygen, *to be submitted* **2008**.

### 5.2 Publications as Co-author

- Lu, Y.; Mei, Y.; Schrunner, M.; Ballauff, M.: In-situ formation of Ag nanoparticles in polystyrene (PS) core-polyacrylic acid (PAA) brush particles by UV irradiation, *PMSE Preprints* (Am. Chem. Soc., Div. Polym. Chem) **2007**, *96*, 795.

- Lu, Y.; Mei, Y.; Schrunner, M.; Ballauff, M.; Möller, M.; Breu, J.: In situ formation of Ag-nanoparticles in spherical polyelectrolyte brushes by UV-radiation, *J. Phys. Chem. C.* **2007**, *111*, 7676.
- Yu, M.; Lu, Y.; Schrunner, M.; Polzer, F.; Ballauff, M.: Spherical Polyelectrolyte Brushes as Carriers for Catalytically Active Metal Nanoparticles, *Macromol. Symp.* **2007**, *254*, 42.
- Schrunner, M.; Schmelz, J.; Proch, S.; Kempe, R.; Miyajima, N.; Ballauff, M.: Bimetallic Metal Nanoparticles Immobilized on Spherical Polyelectrolyte Brushes, *PMSE Preprints (Am. Chem. Soc., Div. Polym. Chem.)* **2008**, *98*, 106.
- Hain, J.; Schrunner, M.; Lu, Y.; Pich, A.: Design of Multicomponent Microgels by Selective Deposition of Nanomaterials, *Small* **2008**, *4*, 2016.
- Lu, Y.; Proch, S.; Schrunner, M.; Kempe, R.; Ballauff, M.: Thermosensitive Core-shell Microgel Particles as Carrier System for Catalytic Active Metal Nanoparticles **2008**, *accepted PMSE*.
- Crassous, J.J.; Wittemann, A.; Siebenbürger, M.; Schrunner, M.; Drechsler, M.; Ballauff, M.: Direct imaging of temperature-sensitive core-shell latexes by cryogenic transmission electron microscopy, *Colloid. Polym. Sci.* **2008**, *286*, 805.
- Hoffmann, M.; Lu, Y.; Schrunner, M.; Harnau, L.; Ballauff, M.: Dumbbell-Shaped Polyelectrolyte Brushes Studied by Depolarized Dynamic Light Scattering, *Journal of Physical Chemistry B* **2008**, *112*, 14843.
- Crassous, J. J.; Rochette, C. N.; Wittemann, A.; Schrunner, M.; Balluff, M.; Drechsler, M.: Analysis of Polymer Colloids by Combining Cryo-Transmission Electron Microscopy with Small Angles X-Ray Scattering, *accepted Langmuir* **2009**.
- Lu, Y.; Hoffmann, M.; Yelamanchili, R. S.; Terrenoire, A.; Schrunner, M.; Drechsler, M.; Möller, M. W.; Breu, J.; Ballauff, M.: Well-defined crystalline TiO<sub>2</sub> nanoparticles generated by a templated synthesis at room temperature, *accepted Macromol. Chem. Phys.* **2009**.
- Häntzschel, N.; Hund, R.-D.; Hund, H.; Schrunner, M.; Pich, A.; Herrmann, K.; Lück, C.: Hybrid Microgels with Antibacterial Properties, *accepted Macromolecular Bioscience* **2009**.

## 6 Appendix

### 6.1 Presentations at International Meetings

- Polyamphi, Chadova Plana, Czech, September 2005, *poster presentation*:  
‘Preparation of MeNP (Au, Ag, Pd, Pt) on polyelectrolyte brushes nanocomposites and their catalytic reduction of 4-nitrophenol’
- Bayreuther Polymer Symposium (BPS), Bayreuth, Germany, September 2005, *poster presentation*:  
‘Preparation of polyelectrolyte brush-metal (Au, Ag, Pd, Pt) nanocomposites and their catalytic reduction of 4-nitrophenol’
- Trends in Nanoscience, Kloster Irsee, Allgäu, Germany, Februar 2007, *poster presentation*:  
‘Metal nanoparticles immobilized on spherical polyelectrolyte brushes and their catalytic application’
- Bayreuther Polymer Symposium (BPS), Bayreuth, Germany, September 2007, *poster presentation*:  
‘Synthesis and Characterization of Metal Nanoparticles immobilized on Spherical Polyelectrolyte Brushes and their Application in Catalysis’
- React, Dresden, Germany, September 2007, *poster presentation*:  
‘Synthesis and characterization of gold- and bimetallic-nanoparticles on spherical polyelectrolyte brushes and their application as catalysts’
- Russel Berrie Nanotechnology (RBNI) Winter School, Dead Sea, Israel, February 2008, *poster presentation*:  
‘Synthesis and Characterization of Gold- and Bimetallic Gold-Platinum-Nanoparticles on Spherical Polyelectrolyte Brushes and their Application as Catalysts’

## 6.2 Abbreviations and Symbols

<i>[X]</i>	<i>reference list</i>
<i>1, 2</i>	<i>serial number of substances</i>
<i>A-co-B</i>	<i>block-co-polymer</i>
<i>2-AEMH</i>	<i>2-amino ethyl methacrylate-hydrochloride</i>
<i>AgNP</i>	<i>silver nanoparticle</i>
<i>AuNP</i>	<i>gold nanoparticle</i>
<i>Cryo-TEM</i>	<i>cryogenic transmission electron microscopy</i>
<i>CTAB</i>	<i>cetyl trimethyl ammonium bromide</i>
<i>DCP</i>	<i>disc centrifuge</i>
<i>DLS</i>	<i>dynamic light scattering</i>
<i>DMAEMA</i>	<i>N,N dimethyl amino ethyl methacrylate</i>
<i>Fig.</i>	<i>Figure</i>
<i>HMEM</i>	<i>2-[p-(2-hydroxy-2-methylpropiophenone)]- ethylene glycol-methacrylate</i>
<i>h</i>	<i>hour</i>
<i>HR-TEM</i>	<i>high resolution transmission electron microscopy</i>
<i>HAADF-STEM</i>	<i>high angle annular dark field scanning transmission electron microscopy</i>
<i>Cat.</i>	<i>catalysator</i>
<i>conc.</i>	<i>concentrated</i>
<i>L<sub>c</sub></i>	<i>contour length</i>
<i>Solv.</i>	<i>solvent</i>
<i>m</i>	<i>meter</i>
<i>Me</i>	<i>metal</i>
<i>NP</i>	<i>nanoparticle</i>
<i>4-Nip</i>	<i>4-Nitrophenol</i>
<i>p</i>	<i>para-</i>
<i>PAA</i>	<i>poly(acrylic acid)</i>
<i>PMMA</i>	<i>poly(methyl methacrylate)</i>
<i>PS</i>	<i>poly styrene</i>
<i>PSS</i>	<i>poly(styrene sulfonate)</i>

<i>PtNP</i>	<i>platinum nanoparticle</i>
<i>R<sub>H</sub></i>	<i>hydrodynamic radius</i>
<i>RT</i>	<i>room temperature</i>
<i>SPB</i>	<i>spherical polyelectrolyte brush</i>
<i>TEM</i>	<i>transmission electron microscopy</i>
<i>t</i>	<i>time</i>
<i>T</i>	<i>temperature</i>
<i>Tab.</i>	<i>table</i>
<i>THF</i>	<i>tetrahydrofuran</i>
<i>V-50</i>	<i>α, α'-Azo-di-isobutyramidine-di-hydrochloride</i>
<i>WAXS</i>	<i>Wide angle X-ray scattering</i>
<i>[wt.-%]</i>	<i>solid content [wt.-%]</i>

### 6.3 Danksagung

Ich möchte mich bei allen bedanken, die auf vielfältige Weise zum Gelingen dieser Arbeit beigetragen haben, insbesondere bei:

- Meinem verehrten akademischen Lehrer Herrn Prof. Dr. M. Ballauff für die außergewöhnliche Aufgabenstellung und sein fortwährendes Interesse an meiner Arbeit, die vielen Anregungen und seine stetige Diskussionsbereitschaft.
- Herrn Dr. A. Wittemann für unzählige Ratschläge und viele Diskussionen, vor allem bei Problemstellungen bezüglich der SPB.
- Herrn Prof. Dr. Y. Talmon, sowie seiner Gruppe für die ausgezeichnete Betreuung am TECHNION in Haifa vor Ort und der exzellenten Unterstützung bei der Bearbeitung elektronenmikroskopischer Fragestellungen.
- Herrn Dr. Y. Kauffmann für die gute Zusammenarbeit bei Fragestellungen und Arbeiten zu HR-TEM.
- Herrn Prof. Dr. U. Glatzel, J. Preussner, C. Liebscher und Dr. M. Nobuyoshi für Diskussionen zu elektronenmikroskopischen Fragestellungen und Geräten.
- Herrn Dr. M. Drechsler und C. Kuhnert für die Einweisung und Betreuung der elektronenmikroskopischen Infrastruktur in Bayreuth.
- Herrn Dr. S. Proch für die gute Zusammenarbeit und stete Diskussionsbereitschaft bei katalytischen Untersuchungen.
- Herrn G. Glatz bei der Einführung in die elementaranalytischen Messungen.
- Herrn Prof. Dr. J. Breu, Herrn J. Thun und Herrn M. Möller für die gute Zusammenarbeit und stete Diskussionsbereitschaft bei Röntgenuntersuchungen.
- Frau C. Bächer, Frau C. Thunig und Herrn K.-H. Lauterbach für Ihre stete Hilfsbereitschaft und Unterstützung.
- Herrn F. Polzer für die angenehme Zusammenarbeit und stete Hilfsbereitschaft in unserem Labor.
- Allen Mitgliedern des Arbeitskreises PC I, auch den hier nicht namentlich erwähnten, für das gute Arbeitsklima kombiniert mit ständiger Hilfsbereitschaft.





## 6.4 Schlusserklärung

Hiermit erkläre ich, dass ich die vorliegende Arbeit selbständig verfasst und keine anderen als die angegebenen Quellen und Hilfsmittel benutzt habe.

Ferner erkläre ich, dass ich nicht anderweitig mit oder ohne Erfolg versucht habe, eine Dissertation einzureichen oder mich einer Doktorprüfung zu unterziehen.

*Bayreuth, den 08. Oktober 2008*

---

*Marc Schrinner*